Improved magnetic feedback system on the fast rotating kink mode

Qian Peng

Submitted in partial fulfillment of the
requirements for the degree
of Doctor of Philosophy
in the Graduate School of Arts and Sciences

Columbia University

2016

Improved magnetic feedback system on the fast rotating kink mode

Qian Peng

Abstract

This thesis presents an improved feedback system on HBT-EP and suppression of the fast rotating kink mode using this system. HBT-EP is an experimental tokamak at Columbia University designed to study the magnetohydrodynamic (MHD) instabilities in confined fusion. The most damaging instabilities are global long wavelength kink modes, which break the toroidal symmetry of the magnetic structure and lead to plasma disruption and termination. When a tokamak is surrounded by a close fitting conducting wall, then the single helicity linear dispersion relation of the kink instability has two dominating branches: one is the "slow mode", rotating at the time scale of wall time, known as resistive wall mode (RWM), the other is the fast mode, that becomes unstable near the ideal wall stability limit. Both instabilities are required to be controlled by the feedback system in HBT-EP. In this thesis, improvements have been made upon the previous GPU-based system to enhance the feedback performance and obtain clear evidence of the feedback suppression effect. Specifically, a new algorithm is implemented that maintains an accurate phase shift between the applied perturbation and the unstable mode. This prevents the excitation of the slow kink mode observed in previous studies and results in high gain suppression for fast mode control at all frequency for the first time. When the system is turned off, suppression is lost and the fast mode is observed to grow back. The feedback performance is tested with several wall configurations including the presence of ferritic material. This provides the first comparison of feedback control between the ferritic and stainless wall. The effect of plasma rotation on feedback control is tested by applying a static voltage on a bias probe. As the mode rotation being slowed by the radial current flow, a higher gain on the kink mode is required to achieve feedback suppression. The change in plasma rotation also modifies the plasma response to the external perturbation. The optimal phase shift for suppression changes with the modified response and these observations are consistent with the predictions of the

single helicity model.

CONTENTS

LIST OF FIGURES

ACKNOWLEDGMENTS

My experience at Columbia has been a period of great personal and professional growth. I enjoyed working with the professors, staff and students associated with HBT-EP through my graduate school. I thank Mike Mauel and Jerry Navratil for their leadership in running the group and their enthusiasm in discoveries in the experiment. I thank Allen Boozer and Andrew Cole for lecturing me about theories related to plasma modelling and answering all my questions. I thank Nick Rivera and Jim Andrello for keeping the tokamak operational. My thanks go to students Jeffrey Levesque, Daisuke Shiraki, Bryan DeBono, Nikolaus Rath and Patrick Byrne for teaching me all the details about the machine. My thanks go to students Christopher Stoafer, Paul Hughes, Sarah Angelini and Dov Rhodes for making the experience here colorful.

I thank my relatives for supporting my career here. I am grateful of my parents' support and belief in my endeavors here. I am most grateful to my wife, Yicong Ma, who chose to pursue her Ph.D. degree in U.S. so we can stay together. Her support and trust gave me the strength to finish this work.

I. INTRODUCTION

Energy has always been important in human history. Utilization of fire separated us from other animals. We collected energy from wood and grease, made light and heat, went through the dark age into the age of reason and science. Prosperous cities with large population were built around fertile lands, where the food, the energy for ourselves, were abundant. Today, massive deployment of machines relies heavily on the sustained supply of energy to maintain their daily activities. Topics about oil production, which directly relates to gasoline availability and power plant fuel, are always at the center of public attention. As the demand of energy grows and with traditional resources limited, we are constantly in searching for new ways to boost our energy production capacity. Nuclear energy, firstly demonstrating its power during world war II, is considered as a promising resource. Many fission power plants have already been built all over the world and is contributing 10% of the total electricity production. Fusion, another form of nuclear energy, was first demonstrated by United States in the 1952 "Ivy Mike" test of the hydrogen bomb[1]. Provided this awesome energy can be safely controlled, fusion will become a useful energy source for humanity. The potential of safe fusion energy has motivated decades of studies about how to safely and practically harness fusion energy for power plant[2].

This thesis investigates an important topic about controlling the instabilities of magnetically confined plasma needed to achieve the sustained burning fusion condition in a tokamak. Specifically, a feedback suppression method is demonstrated on the plasma instabilities which, if left uncontrolled, reduces the power and reliability of fusion energy production. The suppression is demonstrated under several experimental conditions, and our experimental results verify the predictions of a linear single helicity model for kink modes in HBT-EP.

A. Fusion and tokamak

Fusion is the process that heats the sun and stars, where atomic nuclei collide with each other, undergo nuclear fusion, and release energy. The released energy in nuclear reaction is proportional to the mass difference between the reactant nuclei and the reaction products. The variation is highest for the lightest elements: like hydrogen fusion than by the fission of uranium.

This abundant energy resource in nature, however, does not get released easily. To release the energy, fusion requires two nuclei to overcome the Coulomb repulsion and fuse into one. Nuclear attraction and fusion from quantum tunneling only become effective after most of the Coulomb barrier has been penetrated[3]. This barrier results in a relative small probability for fusion reaction events, a small cross section. The largest cross section occurs with deutrium-tritium (D-T) fusion. But even for D-T fusion, many thousands of Coulomb collisions will occur for each DT fussion collision.

The nuclear process that is proposed for fusion above is

$$\mathrm{D} + \mathrm{T} \rightarrow \mathrm{He}^4(3.5\mathrm{MeV}) + \mathrm{n}(14.1\mathrm{MeV})$$

where deutrium and tritium fuse into helium and an extra neutron. This process produces an energetic alpha particle that later sustains the fusion plant and a fast neutron that can be used to generate heat and electricity. In order for this process to happen, the nuclei of D and T must overcome the Coulomb repulsion force to get close enough for strong force to take over. The reaction cross section σ is a measurement of the probability f of the fusion reaction. The probability also depends on the density of the two species that collide: $f = n_1 n_2 \sigma$ where n_i is the density of the nuclei species. The cross section is a function of the relative velocity between two nuclei. σ is nearly zero at room temperature and peaks around $10 \sim 100$keV, where the particles have enough energy to overcome the barrier but still have relatively slow speed to allow enough time for nuclear attraction. Because this temperature is well above the ionization energy (13.6eV for hydrogen), the reactants exist as ionized gas, called plasma.

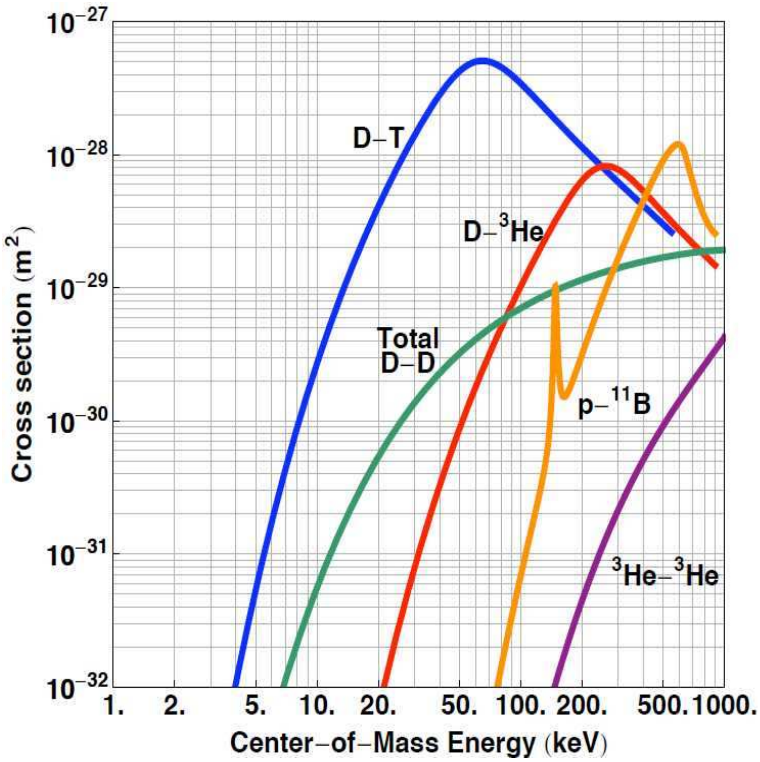

Figure 1. The cross section of fusion reaction v.s. nuclei energy.

Such high temperature of the reactants defies any material that could be served as the boundary of the container. Two methods have thus been proposed to confine the plasma. One is inertial confinement, which puts the reactants initially at rest in the center of a large vacuum chamber. Lasers are then fired at the reactants to quickly compress them and trigger fusion at the inner layers of the target. Everything happens so fast that the inertia of the reactants prevents them from disassembling before the fusion process begins. Inertial fusion requires multiple fusion explosions sustained in a pulse-like fashion[4].

Magnetic confinement, the other method, aims to confine the reactants for longer time, by taking advantage of the Lorentz force on the ionized reactants, $\vec{F} = q(\vec{E} + \vec{v} \times \vec{B})$. In a neural plasma where the electric force is small, the $\vec{v} \times \vec{B}$ force prevents charged particles from crossing the magnetic field line, yet allowing the free streaming along it. If such free streaming can be confined in a finite volume with no magnetic field going across the surface, then a confinement is achieved on the first order by the $\vec{v} \times \vec{B}$ force. Plasma can still escape due to higher order terms contributed by non-uniform field or collision transport, which is addressed in the latter part of this section.

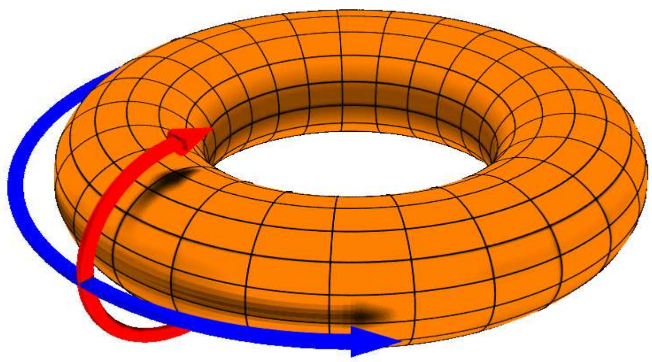

Figure 2. An example of the torus. The blue arrow shows the toroidal direction and the red arrow shows the poloidal direction.

Torus, shown in Fig. 2, is one topology shape in which a bundle of magnetic field lines can be confined within. Two directions are defined in the context of a torus. If the torus is viewed as a bent cylinder, the z direction is called the toroidal direction and the θ direction is called the poloidal direction. These two directions are shown in Fig. 2 as blue and red arrows respectively.

Particles drift away from magnetic surface with higher order force terms contributed by the non-uniformity of magnetic field. The confinement is made possible by creating a poloidal magnetic field that guilds the magnetic field line around the minor circle while travelling along the toroidal direction. A helical structure is created and when a particle streams along this helical path, it drifts inward or outward the

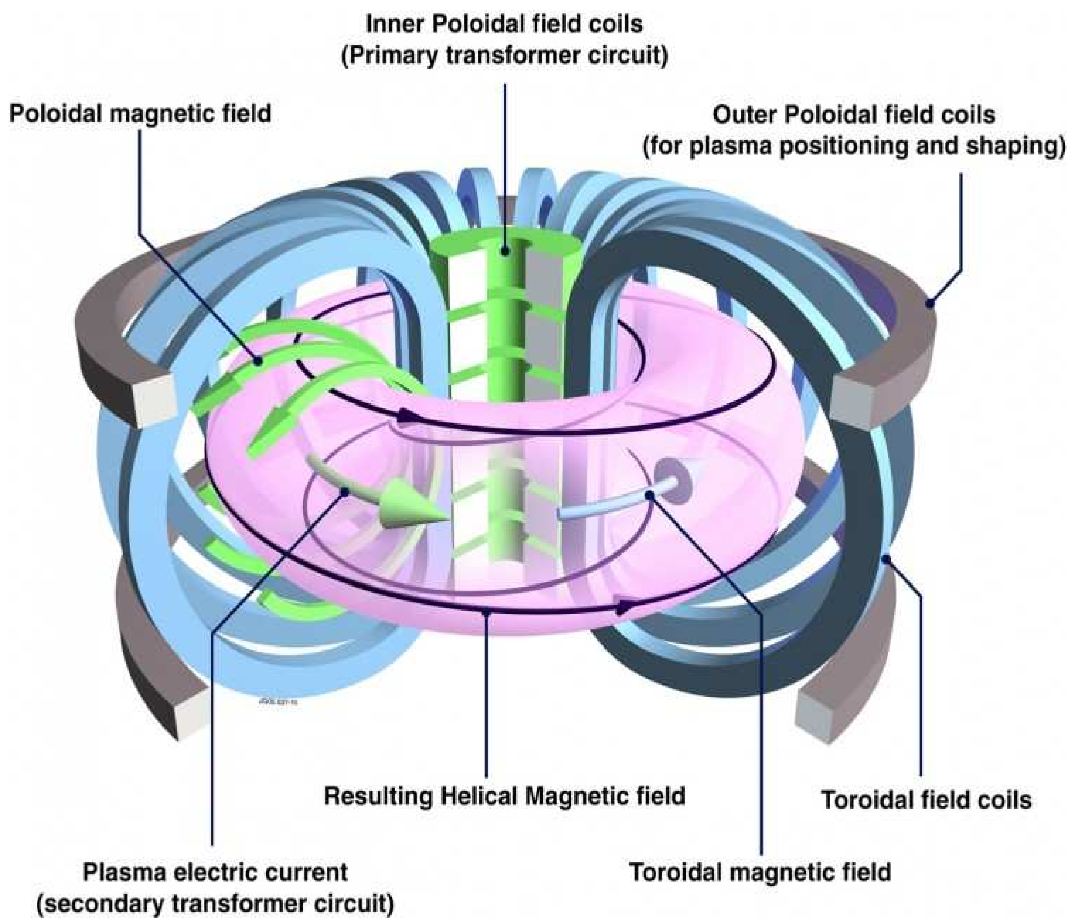

Figure 3. Generic Tokamak.

surface, depending on its location at the surface. The averaged effect is a cancellation of the drift and enhancement of confinement. The two components of this designed magnetic field is generated differently. The toroidal field (TF) is created by external coils running along the poloidal direction, known as TF coils. The major poloidal field is generated by a toroidal current, which runs through the plasma in tokamak.

A generic configuration of the tokamak device is shown in Fig. 3. In addition to the TF coils discussed, a tokamak also has outer poloidal field coils that create a vertical magnetic field. This field maintains the plasma (indicated as purple) in place horizontally by countering the self-expanding force generated by the plasma toroidal current. The inner poloidal field coils in the center, known as Ohmic Heating coils, are used to drive the plasma toroidal current. Change of the current in these coils creates an induced electric field toroidally outside the solenoid, which accelerates the initial free electrons provided by the electron gun. These accelerated electrons ionize the gas and generate plasma. After the plasma breakdown, the $\vec{E}$ field continues to drive and sustain the plasma toroidal current. Tokamak has been the most successful device at reaching fusion-grade plasma conditions so far. Another related type of large magnetic confinement device is stellarator.

For net fusion power generation, the plasma must be dense, hot and confined long enough so that the power harnessed from reactor exceeds the power required for operation. This is represented by the triple product criteria:[5]

$$nT\tau \gtrsim 5 \times 10^{21} keV \cdot s/m^3$$

For D-T fusion in tokamak, $n \sim 10^{20} m^{-3}$ is the typical plasma density achieved, $T \sim 10keV$ is the typical temperature and $\tau \sim 5secs$ is the confinement time. To reach fusion condition, confinement time must be at least several seconds.

A substantial cost for the tokamak is magnetic field generation and maintenance. With the same magnetic field strength generated, one wants to produce the largest plasma pressure, nT. A metric for the efficiency is the ratio of the volume averaged plasma pressure to the averaged magnetic pressure, called beta:

$$\beta = \frac{< p >}{< B^2 > /2\mu_0}$$

Achieving high beta value is important for the efficiency of fusion power plant. However, the plasma becomes more unstable with increased β [6, 7]. Plasma develops local or global instabilities that deform the magnetic field. These instabilities can grow quickly, degrading plasma confinement and causing a disruption. Certain empirical β limit criteria has been found experimentally[6–8], beyond which plasma disrupts quickly. Suppressing the instabilities is essential to extend the confinement time and increase the efficiency of the controlled fusion[9].

B. Tokamak instabilities and feedback control

Instabilities in tokamak are driven by gradient in plasma current density and pressure[9]. Such instabilities often cause the loss of thermal energy through radial transport, and reduce the rotational shear of magnetic field which are essential for confinement. These instabilities need to be carefully controlled for a burning plasma device.

The instability in plasma can be modelled at different levels. The energetic ions and electrons in plasma, like molecules in gas, move at very high speed and collide with each other frequently on the micro-structure level. This suggests a natural way of characterizing plasma with a distribution function $f(\vec{x}, \vec{v})$, the same method used to analyze gas and liquid, where the density of the particle population is provided with regard to velocity and spacial location. Macro physics quantities are then expressed as integration on this distribution function. While this method has the potential to provide ultimately first principle calculation in almost every aspect of the plasma property, significant demand in computation power rules out such implementation for a real 3D device in detail. Brute force calculation about the distribution function is either restricted to analytical derivation, where the geometry is much simplified, or applied numerically on a localized region in plasma. Empirically, a fusion power plant cares most about the instability at macro scale, at which the external perturbations are effective. Imagine a scale bar, with the finest distribution function at one end and the industrial pragmatic need at the other end. Detailed computation could reveal the connection bonded by physics law, but is difficult to carry out. A cascade of theories are thus developed along the bar to address the plasma characteristic at different levels of scrutiny, where uninteresting information is dropped and effects on the macro scale is focused.

On the micro structure level, the distribution function follows a dynamic governed by the Vlasov equation[10]:

$$\frac{\partial f_\alpha}{\partial t} + \vec{v}_\alpha \cdot \vec{\nabla} f_\alpha + q_\alpha(\vec{v}_\alpha \times \vec{B} + \vec{E}) \cdot \frac{\partial f_\alpha}{m_\alpha \partial \vec{v}_\alpha} = C[f] \tag{1}$$

where $C[f_\alpha]$ is the collision operator on the species. This operator includes collisions within the single species where energy and momentum are redistributed while also considers collision between different species where the momentum and energy are exchanged. The location dependency in non-uniform fields enters the equation through $\vec{B}(x)$ and $\vec{E}(x)$. These macro quantities, $\vec{E}$ and $\vec{B}$, not only include the externally applied field, but also contain the field induced by the plasma itself. Solution for the function $f(\vec{v}, \vec{x})$ provides a statistically equivalent estimation of the plasma state as tracking billions of particles simultaneously.

The gyro-kinetic theory reduces the complicity at micro scale level by utilizing the observation that a charged particle can only move freely along the magnetic field line. Under the magnetic field, a charged particle circles around the field line perpendicularly as a magnetic dipole. In the parallel direction along the $\vec{B}$ field, the center of the dipole follows the field line on the first order. The distribution on these two velocity dimensions perpendicular to the magnetic field line can thus be reduced to a dependency on the conserved quantity, $\mu = mv_\perp^2/2B$, the magnetic moment. The dependency of the distribution function on the kinetic energy is approximated , on the leading order, as an equilibrium in Maxwell distribution $f_0 \sim exp(-mv^2/2kT)$. The dynamics of f, under the gyro-kinetic theory, is solved with respect to the expansion around this equilibrium[11].

The Neoclassical Toroidal Viscosity (NTV) theory focuses on the connection between the toroidal rotation of plasma, which is critical in maintaining the plasma stability, and the particle distribution function which is influenced by the asymmetry of the torus structure. It solves the displacement δf with respect to the Vlasov equation under the perturbed torus geometry. Experimentally, a drag force on the plasma rotation is observed when the torus is not perfectly symmetric. The theory predicts that magnetic perturbation on the order of $\delta B/B \sim 10^{-3}$ is enough to slow down the plasma rotation and build up radial particle transport[12, 13].

MHD theory is a further step towards the macro scale analysis. While acknowledging that the plasma consists of ions and electrons, this theory does not treat them separately in the equations. The total mass density $\rho = \sum \rho_\alpha$ is mostly contributed by the heavy ions, so is the momentum of the mass velocity $\vec{u}$. The difference in ion and electron velocity enters the equation through current density $\vec{j} = q(n_i\vec{v}_i - n_e\vec{v}_e)$. MHD uses only macro physics quantities in the equations, which consist of the Maxwell's equations and the plasma fluid equations[14]:

$$
\begin{aligned}
\vec{E} + \vec{u} \times \vec{B} &= \eta\vec{j} \\
\rho\frac{d\vec{u}}{dt} &= \vec{j} \times \vec{B} - \vec{\nabla}p - R \\
\frac{\partial\rho}{\partial t} + \vec{\nabla} \cdot (\rho\vec{u}) &= 0 \\
\frac{d}{dt}(\frac{p}{\rho^\gamma}) &= 0
\end{aligned}
$$

These equations come from integrations on Eq. 1 with weights like $\vec{v}_\alpha$ or m_α, and combining the equations from ions and electrons. η is the resistivity and R is the viscosity force from the integration on the collision operator $C[f]$. MHD theory assumes that the plasma is charge neutral on the macro scale and the electron mass can be ignored compared with ion mass. In *ideal* MHD, η and R are zero[15].

Reduced MHD theory models the plasma in a cylindrical tube and establishes an intuitive picture of the instabilities in tokamak geometry[16, 17]. In the cylindrical shape, the magnetic field is assumed to be much stronger in the toroidal direction compared with the component in the poloidal direction. Physical quantities, including the perturbed magnetic field, the plasma current and velocity, are expanded in orders with respect to the ratio $\epsilon = a/R$, where a is the typical torus minor radius and R the major radius.

The structures obtained in this expansion become the basis for magnetic field decomposition. The coordinate system constructed on a torus shape, as is shown in

Fig. 2, is used to describe the physics quantities about plasma in a tokamak. In this coordinate system, ψ is used to distinguish the layers of torus and (θ, φ) is used to identify the points on each surface. The basis structure of the instability often has a form of $\exp[-i(m\theta - n\varphi)]$, which is called the (m, n) mode respectively. The m, n number must be integers, and the modes are analyzed discretely.

Instabilities observed experimentally at macro scale are explained by the eigen structures with positive growth rate. The positive growth rate is sometimes triggered by the non-axisymmetric field inheritant in the device's hardware, which provides the source of error field. The error field which resonates most strongly with the plasma is routinely cancelled by the compensation coils. The cancellation is not exact, however, and it is important to understand the impact of the remaining error field. One of the initial impact of an error field is magnetic braking. The magnetic braking reduces plasma rotation; the magnetic braking increases radial transport; the magnetic braking destabilizes the plasma and makes it sensitive to other tearing instabilities[6, 17–20].

Feedback control that responds directly to plasma instability provides capability beyond what is offered by static control of compensation coils[9]. The feedback control in a tokamak is primarily used to suppress the resistive wall mode (RWM)[21–23], which is a slowly growing kink mode that occurs in the presence of a resistive wall. The resistive time of the wall, τ_w, determines the time scale of the mode growth rate. Feedback control for error field compensation on stable plasma is another important application. This application is introduced when the plasma is marginally stable and the kink mode amplification of the external field is strong. Accurate compensation is required under such conditions to avoid braking and locking of the rotation. Fast time scale control of kink modes is equally an important role for the feedback system. The feedback control becomes necessary when kinetic effects are not enough to stabilize the plasma. Suppression of a fast rotating kink mode with typical frequency around 7kHz, through a GPU based feedback system in HBT-EP, is presented in this thesis.

Theories developed for feedback control involves many topics, including noise filtration, system modelling, prediction and optimization. It is important to identify a valid model such that the system's response to external perturbation can be predicted. Equally important is making sure that the desired perturbation is accurately delivered to the system. While most feedback systems in a tokamak currently detect and perturb the plasma through magnetic field, there have been concerns about the applicability of such methods with larger machines like ITER. In those machines, the walls are often so thick that the eddy currents severely reduce the performance of the magnetic sensors and the control coils behind the wall. Feedback schemes equipped with soft-Xray and fast camera as detection methods and electron cyclotron resonance as a perturbation method have been proposed and investigated[24, 25]. The physics model governing the plasma system, however, should be the same regardless of the perturbation and detection method. Knowledge developed with the magnetic feedback helps better design of non-magnetic feedback systems. The physics model and the parallel computation platform, investigated through the magnetic feedback control in this thesis, can be extended to include other detection and perturbation techniques.

A successful feedback control system for plasma instability suppression addresses the unique requirements of the device it is applied to. A range of techniques have been implemented on large machines such as DIII-D, NSTX, and RFX- mod, designed to address their unique MHD control requirements. Separation of direct perturbation coil pickup from sensor signals reduces the noise in the input signal. Real-time equilibrium reconstruction provides a better estimation of the pressure and density profile in tokamak. Mode control with state-space method and model-based RWM discrimination increases the efficiency of applying the perturbation.[26–29].

HBT-EP has been developing feedback control methods on toroidally confined plasmas for many years. Magnetic sensors located around the machine are used to measure the unstable mode, estimate its amplitude, phase and rotation frequency. The feedback system drives the control coils accordingly to cancel or suppress the mode. HBT-EP group has carried out extensive research on these techniques and has explored several designs[23, 30–33]. It has studied on the smart shell designs; it has studied the mode control with FPGA; It is now studying the GPU-based feedback system. In the smart shell design, control coils are used to cancel the flux through the wall, effectively creating an artificial ideal wall. The mode control with FPGA models the instability as a rotating mode and perturbs it with predictions from the model. The FPGA unit was then replaced by GPU for easier programming accessibility and larger capacity of handling more signals simultaneously. Many algorithms have since been implemented and tested under the GPU framework.

The difficulty of feedback suppression in HBT-EP lies in the fast rotating nature of the unstable mode. Each revolution takes only around $150\mu s$ and the mode's amplitude and rotation frequency changes on the same time scale. Quick response of the feedback system is required to handle the fast dynamics. The current feedback system in HBT-EP uses a GPU based parallel computing system to take in signals from 80 feedback sensors and calculate the driving signals for the 40 control coils. The latency from signal input to output is $22\mu s$. Aside from this latency, the delay in response also arises from the coil's reaction to the fast change of the driving signal for amplifier.

These difficulties in HBT-EP are addressed in this thesis. Efficiency in memory and computation for capturing the fast rotating mode signal is achieved by redesigning the logic. More control power directed for the handling of the abrupt changes in mode phase is achieved by mitigating the fluctuation in mode amplitude. Agility of the feedback system is enhanced by compensating the delay due to the inductive rise time of the control coils. Feedback suppression is demonstrated in all frequency under several tested scenarios. The suppression has a long duration window and can be clearly observed in each discharge.

Success of the feedback system in HBT-EP demonstrates the capability of responding to fast plasma dynamics in sub-millisecond time scale. Accurate synchronization between applied perturbation and fast rotating plasma instability is critical in achieving suppression without exciting other instabilities. The same technique presented in this work could be used in other platforms where such accuracy is needed.

C. Organization of this thesis

This thesis is organized into five sections and three appendices. Sec. II gives an overview of HBT-EP, the machine on which the work of this thesis is tested on. The hardware specifics will be covered in this section, together with the typical plasma behavior in HBT-EP. It shows why feedback control is needed on this device and what problems need to be considered for designing the system. The model for the MHD instability in HBT-EP is covered in Sec. III, based on which the feedback system is designed. It starts with the surface representation of the MHD instabilities. The mode's interaction with wall and external perturbation is then examined and a dispersion relation is obtained. This equation includes both the slow RWM root and the fast rotating kind mode. The derivation uses some knowledge about general coordinate system, which is covered in Appendix I. Details about the algorithms used in the feedback system are shown in Sec. IV, where the accurate phase shift between the applied perturbation and the detected mode is maintained. The experimental results with the feedback system are shown in Sec. V. The performance is compared with past results. With the improved system, we have also tested its performance under different wall configurations and under a slowed plasma rotation. The plasma becomes more unstable under these configurations, yet the feedback suppression is achieved nevertheless. The experimental results are consistent with the theoretical predictions. In Sec. VI, the key achievements of the thesis are summarized, including: the successful demonstration of the feedback suppression effect under several unfavourable experimental configurations, the consistency between the experimental results and theoretical models, the enhancements of the algorithms by mathematics techniques and the integration of different perturbation methods into one single platform. Some details about the feedback code are shown in Appendix III. In Appendix II, an extension of the fitting method used in the feedback algorithm is discussed.

II. PLASMA IN HBT-EP

The feedback system presented in this thesis is tested on The High Beta Tokamak Extended Pulse (HBT-EP) device, which is an intermediate scale tokamak designed to study the kink and tearing instabilities. The dominant kink instabilities observed in it are fast rotating at $\sim$ 7kHz, with fluctuations in both amplitude and frequency. The fast time scale of this dynamics is the main difficulty faced by the feedback system. More than two hundred magnetic sensors, forty control coils and twenty adjustable shells are equipped by HBT-EP, for detailed analysis of the instability and tests of the feedback algorithm.

Parameters of HBT-EP are shown in Tab. I. The toroidal field is 0.33T and an air-core transformer at the the center of the machine is used to generate plasma current and provide Ohmic heating. The lifetime of a discharge is typically around 5 to 10 ms long.

HBT-EP	Parameters
Major radius (R_0)	$=$ 88 $\sim$96 cm
Minor radius (a)	$=$ 11$\sim$15 cm
Plasma current (I_p)	$\lesssim$ 20 kA
Toroidal field on axis (B_T)	$=$ 0.33 T
Electron temperature (T_e)	$\lesssim$ 150 eV
Electron density (n_e)	$=$ 1$\sim$3e13 cm^{-3}
Pulse length	$=$ 5$\sim$10 ms

Table I. Typical HBT-EP discharge parameters.

A. Hardware in HBT-EP

The unique feature of HBT-EP is its adjustable in-vessel conducting walls. As is shown in Fig. 4, the 20 conducting shells cover the outboard region of the plasma. They are grouped in 10 uniformly distributed sections. Each section has a top shell and a bottom shell whose radial positions can be adjusted individually. The minor radius of the wall can move between 0.17cm to 0.21cm. The coupling between the plasma and the wall strongly depends on the distance between the two. This provides the capability to study the MHD instabilities with respect to the variation of the coupling parameter $c \sim (a/b)^{2m}$, where a and b are the radius of the plasma and the wall, and m is the mode number[17]. It is observed that the plasma is more unstable with reduced coupling, when all the walls are retracted away from the plasma.

Every other shells, along the toroidal direction, are covered with ferritic material, to study the ferritic wall effect. Stainless steels are highly susceptible to activation by fast neutrons generated in fusion. Using it as wall material in fusion reactors would result in nuclear wastes with long-lasting radioisotopes. An alternative is a class of material known as 'low-activation ferritic steels. They are more resistant to fast neutron damage, but are also ferromagnetic, with $\mu_r > 1$. This lowers the perturbed magnetic energy outside the plasma, the barrier of which restrains the kink mode instability. This raises concerns about whether such these materials will reduce stability margins in a tokamak[34]. Ferritic material was installed in HBTEP on the shells to investigate the impact on plasma stability[35]. Since each segment can be moved individually, the overall wall coverage can be configured to be primarily ferritic or primarily stainless-steel.

Numerous feedback sensors and control coils are mounted on those shells for detailed magnetic field measurement and perturbation in precise phase. As is shown in Fig. 4, on each shell, there are two control coils mounted on different poloidal positions. Shifted toroidally, two sensor boxes are mounted on the same poloidal positions with control coils. The shift is to avoid direct coupling between the sensors and the coils. The sensor boxes reside at the inner side of the shell. Each sensor box contains a poloidal field sensor and a radial field sensor. In summary, control coils, poloidal field sensors and radial field sensors all form in 4x10 matrices in space that cover the plasma uniformly along the toroidal direction at the torus' outboard side. The 10 units of each array along the toroidal direction provide a good resolution in point wise measurement. When viewing the signals globally with a $cos(\varphi + \triangle)$ structure, such measurement provides estimation of the amplitude and phase of the mode.

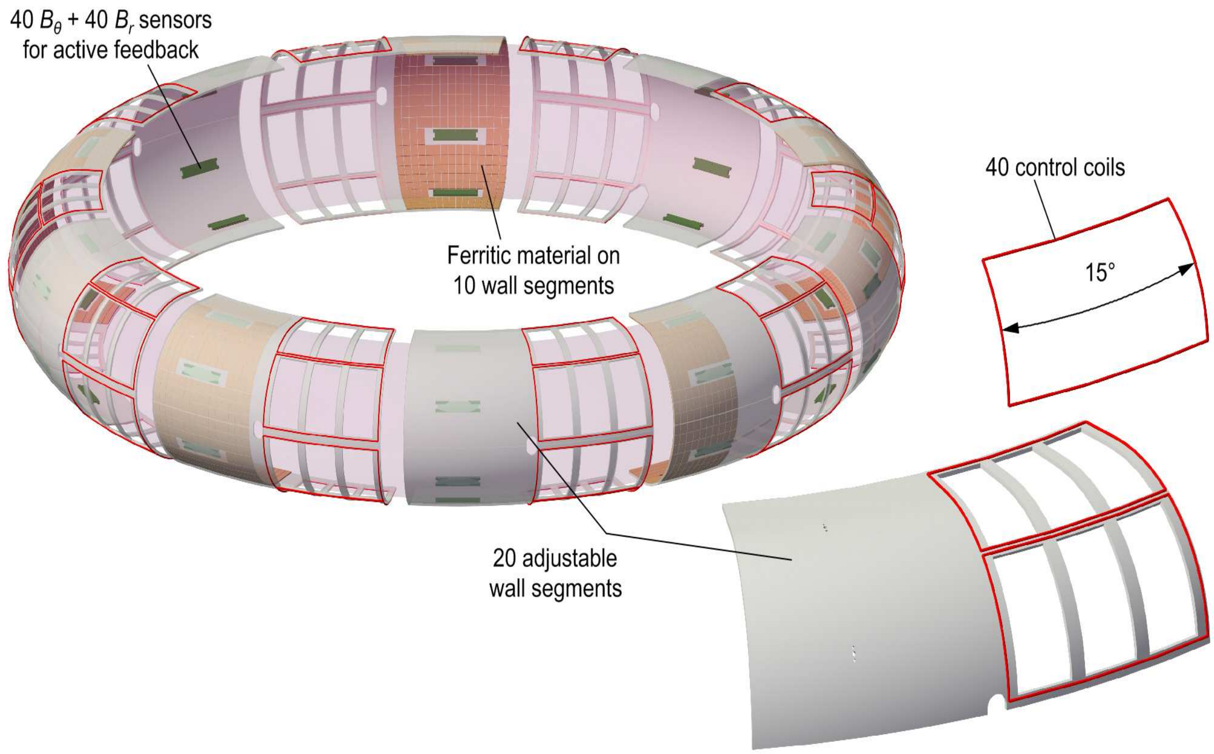

Figure 4. The layout of the shell segments in HBT-EP. There are 2x10 stainless shells, shown in grey. The 4x10 control coils are marked as red loops on the shells. The 4x10 sensor boxes are shown as green on the shell. They have the same poloidal locations as the center of the control coils. The ferritic tiles are shown in brown. They are placed on the inner surface of the shells. Only half of the shells have ferritic material.

In addition to these 80 magnetic sensors, two poloidal arrays of sensors and a toroidal array sensors are also equipped in HBT-EP. The poloidal sensors arrays are located on two opposite toroidal positions on the machine. The array wraps the plasma along the poloidal circle. Each of the array has 32 poloidal field senors and 16 radial field sensors. The toroidal sensor array is at the inner board position. It has 30 poloidal field sensors and 10 radial sensors. These densely placed sensors provide measurement of the global structure of the instability in plasma at higher resolution. They identifies how the structure of the dominant instability evolves over time. The feedback system tested in this thesis does not currently use those sensors in real time. They are used for post-discharge analysis.

Another important device in HBT-EP is the bias probe. It is an electrode probe

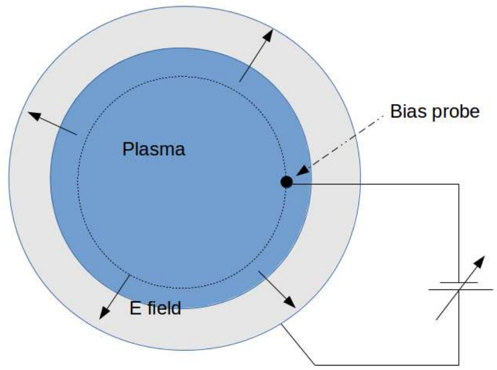

Figure 5. Bias probe illustration. The bias probe creates an radial $\vec{E}$ field that affects plasma rotation.

sticking into the plasma. The tip of the probe is maintained at a programmed voltage which could be different from the plasma floating potential at that location. The plasma streams freely along the magnetic field lines. Not considering the induced loop voltage, the $\vec{B} \cdot \vec{\nabla} V = 0$ property implies constant static electric potential on each layer. Changing the electric potential at one point will effectively modify the potential of the whole surface. This generates additional toroidal torque and changes its rotation speed. In HBT-EP, the bias probe is used to modify the plasma rotation. The rotation can be accelerated, decelerated or even reversed. The feedback system uses this to test its performance on slowed plasma. The bias probe is setup is illustrated in Fig. 5.

B. Fast rotating mode in HBT-EP

The instabilities observed in HBT-EP are typically rotating near 7kHz. The mode's shape, amplitude, phase and rotation speed are measured by the 216 magnetic sensors installed around the machine. In post-discharge analysis, the intrinsic pattern of the rotating mode can be determined by a bi-orthogonal decomposition technique[36]. In the real-time feedback system, however, the feedback system needs to interpret the mode amplitude and phase quickly in real time. The mode amplitude and rotation are inferred from the fluctuation signal measured by the magnetic sensors, which is best presented through a contour plot. An example of the contour plot is shown in the first row of Fig. 6. The x-axis of the plot is time, while y-axis is the measured fluctuation along one array of the sensors in the toroidal direction. Each column of the plot represents the measured mode structure on the sensor array and the mode shifts in phase, because of rotation, as time passes. The mode has a clear $n = 1$ structure along the toroidal direction, as is shown by the stripes. The mode's rotation frequency can be inferred from the slope of the stripe at any give x location. From the plot, we see that the rotation frequency is not constant. The magnitude of the mode is indicated by the contrast of the plot. While the contour plot is clear for human eyes, the feedback system requires a quantitative input for analysis. Two time series are used to represent the mode's rotation and amplitude, which are obtained by projecting the fluctuation signals from the sensor array onto a pair of sin/cos basis functions. The time series from the sine component is displayed on the second row of the figure; the cosine component is similar but shifted by 90 degrees. The mode's rotation frequency and amplitude can be obtained equivalently from these two time series. This signal demonstrates, more quantitatively, how the mode's amplitude and frequency evolve over time, even without external perturbation.

The mode naturally rotates around 7KHz. The mode's rotation can be increased up or slowed down by the feedback system through perturbations applied at a certain phase shift with respect to the measured mode. The rotation can also be influenced with a bias probe, which penetrates into the plasma and connects to the inner surface of it. When the probe is charged at a programmed voltage, it changes the entire electric potential of the magnetic surface, which generates the E field between magnetic surfaces and drives an $E \times B$ flow in the plasma. This technique is used in the experiment to modify the plasma rotation when testing the feedback system on a slowed plasma.

The fast variation in mode amplitude and frequency observed in Fig. 6 presents a

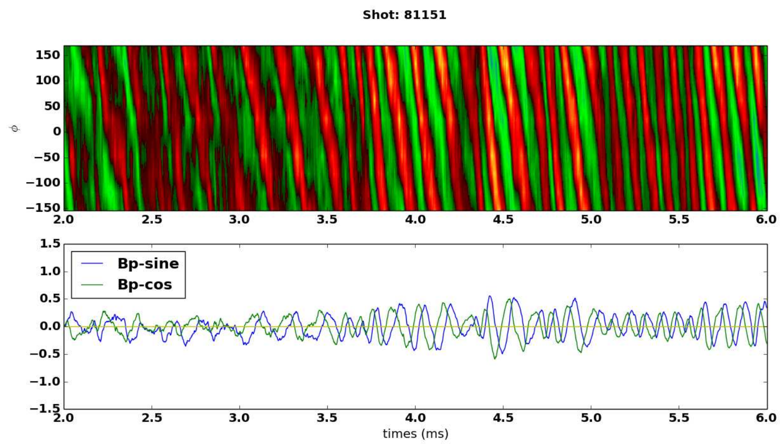

Figure 6. An example of the saturated rotating mode, measured by one feedback array sensors on discharge 81151. The first row shows the contour plot. It displays an $n = 1$ rotating mode structure. The second row plots the perturbation signal against measured signal. No perturbation is applied in this case, but the mode amplitude and rotation frequency evolve over time by itself.

serious problem for the feedback system. Those variations are consistently measured from the sensor arrays, cross verified, and cannot be dismissed as mere noise in the measurement. For each array, the two time series of the sin/cos mode component $A_c(t)$ and $A_s(t)$ can be calculated. The mode amplitude $A = \sqrt{A_c^2 + A_s^2}$ and phase $\triangle\varphi = \arctan(A_c/A_s)$ are then calculated individually for each sensor array. The signals from the four arrays, while seemingly unsteady when viewed alone, are very consistent with each other, as are shown in Fig. 7. Such coherent observation indicates the variation is real and must be handled with care in the feedback system. We will come back to this observation again in Sec. IV to discuss how the fast variation in mode amplitude and frequency is handled in the feedback system.

The unstable fast rotating mode is excited when the edge q goes near an integer number. The mode is unstable on the first order, but as its amplitude grows, the energy dissipates away through mode rotation and wall interaction. Experimentally, the mode is often observed to exponentially grow at first, then the amplitude stays saturated for a while before eventually heading to disruption. A criteria used to judge the effectiveness of the mode suppression by the feedback system is developed upon

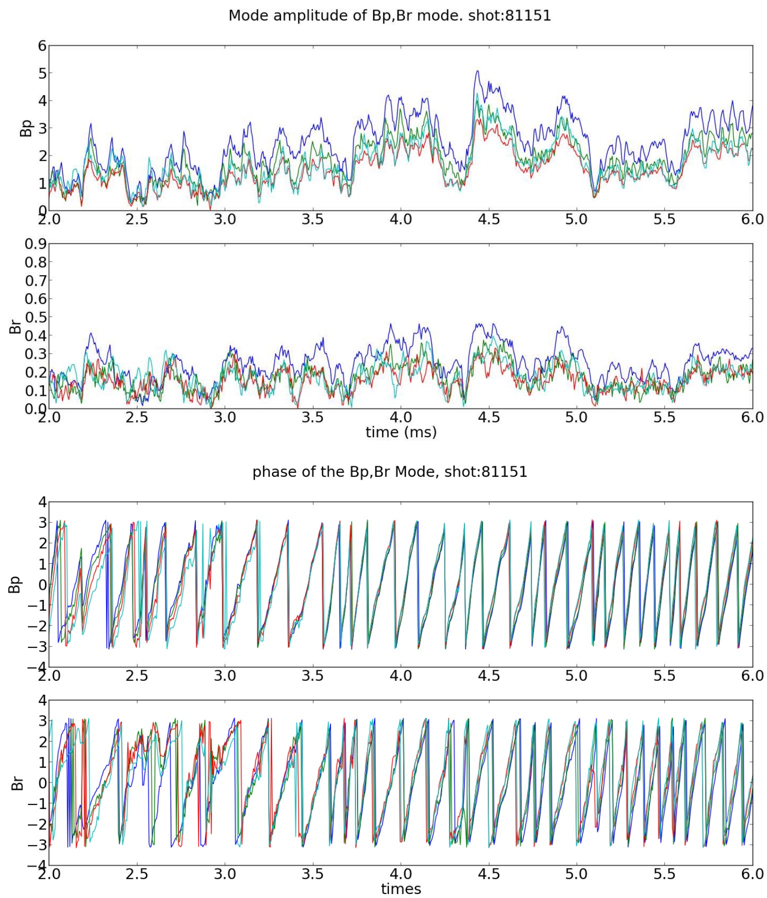

Figure 7. The mode amplitude and phase information obtained from the four sensor arrays. The mode amplitude signal rises and drops consistently across the four arrays. The phase measurement is shifted with respect to different arrays to make the value the same at $t = 3.5ms$, so the evolution of the phase difference between different arrays are made more clear. For the raw signal, there is a constant offset in phase measurements because of different poloidal locations of the arrays and the helical structure of the global mode.

this observation. The mode suppression is effective if the mode's saturated amplitude is reduced. This fast rotating mode is different from the resistive wall mode (RWM) typically observed in many large devices, which is further discussed in Sec. III, It stems from a different root in the dispersion relation, and rotates on a time scale faster than the resistive wall time scale in HBT-EP (~2ms^{-1}). The work in this thesis, developed upon the GPU-based feedback system[32], focuses on synchronizing the perturbation with the fast rotation and achieves mode suppression at all frequency.

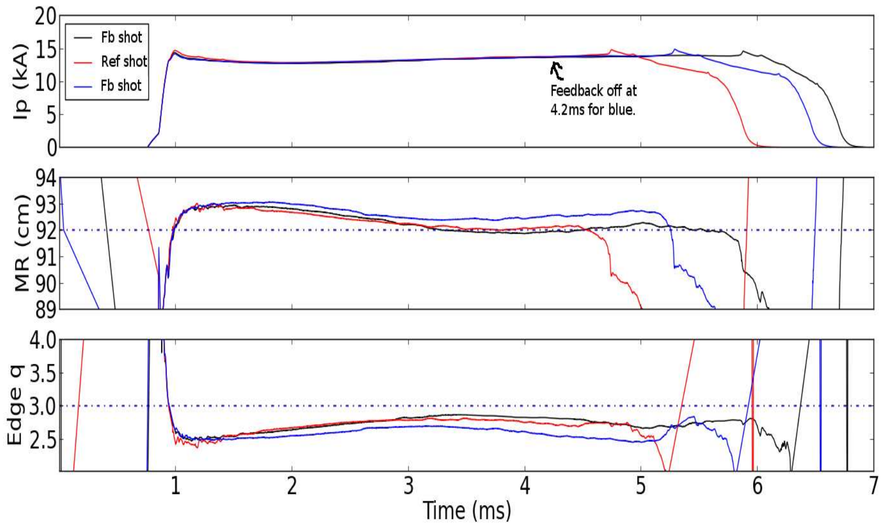

Figure 8. An example of the discharges with plasma total toroidal current (Ip), major radius(MR) and edge q.

Typical plasma toroidal current (Ip), major radius (MR) and edge q time series investigated in this thesis a are shown in Fig. 8. Relatively stable plasma current and major radius traces are maintained to focus on the feedback effect and rule out factors from other possible physics parameters. In the example, one is a reference shot where feedback is off. The other two have feedback on but one is turned off early. Details of the feedback effect regarding to the mode amplitude and rotation will be discussed in Sec. V.

III. MODEL OF THE INSTABILITY

The theory about the instabilities in the plasma is covered in this chapter. The instability in plasma is often modelled as a perturbation on top of a quasi-steady equilibrium. The equilibrium is a torus shaped plasma, possibly rotating and slowly evolving with respect to its major radius, center position and current distribution etc. Upon this equilibrium, the flux coordinate systems is usually constructed, details of which is shown in Appendix I. Deviation away from this equilibrium displayed by the plasma often follows a fast dynamic. The deviation can be stable, if the plasma tends to recover to the equilibrium without external interference, or unstable, if the deviation will grow on its own. Given a perturbation, the thermal and magnetic energy released by plasma, δW_p can be calculated. The perturbation will also increase the magnetic energy in the vacuum by δW_v If the energy δW_p released by plasma is greater than the energy barrier δW_v from the vacuum magnetic field, then it is unstable[5].

The global structure of the deviation is analyzed on the basis of eigen modes. Both the magnetic field and the plasma mass flow are perturbed by these modes. The binding relation between the two means the perturbation in magnetic field alone is sufficient to represent the deviation. Further more, the 3D structure crossing the plasma at different minor radius, ψ, is often reduced to the helical structure of the mode on a surface and thus represented by the (m, n) number. In this pair, n indicates how fast the mode structure changes with respect to the toroidal direction, φ, and m for changes along the poloidal direction, θ.

In this section, we will see how a continuous 3D perturbation of the equilibrium is characterized by the (m, n) number on a surface. The interaction between plasma, the wall and external perturbation is discussed based on this representation. Finally, the dispersion relation for the deviation is calculated and the fast root representing the fast kink instability in HBT-EP is investigated. This model is used in the feedback system to predict perturbation effect and adjust system parameters.

A. Surface representation of the instability

The full 3D plasma system needs to be represented by a few parameters for the feedback system to process as input. The surface representation theory of the deviation from equilibrium serves well for this purpose. The basis for this representation theory is illustrated in this section.

1. Reduced MHD

Reduced MHD theory[16] models the plasma under cylinder coordinates (r, θ, z). It is based on taking $r = \mathsf{Const}$ as the equilibrium magnetic surfaces and assuming a large aspect ratio: $\varepsilon = r/R \ll 1$. The toroidal direction is represented by $z = R\phi$. This model assumes that the kinetic energy of the plasma is much smaller than the magnetic energy: $p \ll B^2/2\mu_0$ and the magnetic field is mostly along the z direction. The component along the perpendicular direction to z is $B_\perp = \frac{r}{R} B_z/q$. For a typical case where the safety number is single digit, one has: $B_\perp/B_z \sim \varepsilon$.

Analysis about the order of the physics quantities can be inferred from the model's assumptions. First, the length scale of the perturbation must be different, depending on whether it is along the field line or perpendicular to it. For a perturbation that takes a pattern of $\exp[i(m\theta - n\phi)]$, with m/n around unity, one has $\nabla_\theta \sim \nabla_\phi$. Since $\nabla_\perp \sim \nabla_\theta / r$ and $\nabla_\parallel \sim \nabla_\phi / R$, the variation is has longer wavelength along the parallel (z) direction: $\nabla_\parallel \sim \varepsilon \nabla_\perp$. The order of current density $\vec{j}$. can be derived with Ampere's law:

$$\begin{aligned}
\mu_0 \vec{j} &= \vec{\nabla} \times \vec{B} \\
&= \left(\vec{\nabla}_\perp + \varepsilon \vec{e}_z \frac{\partial}{\partial z} \right) \times \left(\varepsilon \vec{B}_\perp + B_{0z} \vec{e}_z \right) \\
&= \varepsilon \vec{\nabla}_\perp \times \vec{B}_\perp + O(\varepsilon^2)
\end{aligned}$$

which implies $j_z \sim \varepsilon$ and $j_\perp \sim \varepsilon^2$.

The magnetic field is decomposed into a dominant z component and a perpendicular component. This is expressed as:

$$\vec{B} = \vec{e}_z \times \vec{\nabla}\Psi + B_{z0}\vec{e}_z$$

to immediately satisfy the divergence free condition. The Ampere's law for the current density thus becomes

$$\mu_0 j_z = \nabla^2\Psi$$

where both j_z and Ψ are scalar functions. The above equation should not be confused with the equation for magnetic potential $\mu_0\vec{J} = -\nabla^2\vec{A}$, where the function in question is a vector.

The displacement of plasma is strongly linked with the perturbation in the magnetic field. If we use ξ to denote the displacement of plasma away from its equilibrium position, then its time derivative $\dot{\xi}$ denotes the velocity of the plasma. Combining the ideal MHD equation $\vec{E} + \dot{\vec{\xi}} \times \vec{B} = 0$, where resistivity is ignored, with Maxwell's equations, one has:

$$\begin{aligned} \frac{\partial \vec{B}}{\partial t} &= -\vec{\nabla} \times \vec{E} \\ &= \vec{\nabla} \times (\dot{\vec{\xi}} \times \vec{B}) \end{aligned} \tag{2}$$

This is the connection between perturbation in magnetic field and the displacement of plasma. As is noted previously, an instability, while displaying the deviation in both observation, can be represented by the structure in magnetic field perturbation.

The perpendicular component of $\vec{B}$ consists of the equilibrium in poloidal direction and the perturbation in both radial and poloidal direction. Let $\Psi = \Psi_0 + \delta\Psi$ where $\delta\Psi$ represents the perturbation part of the magnetic field. Then from $\vec{B} = \vec{\nabla} \times (\Psi\vec{z})$ and Eq. 2, one has:

$$\delta\Psi\vec{z} + \vec{\nabla}\chi = \vec{\xi} \times \vec{B}$$

where χ is an arbitrary function to balance the curl-free difference between the $\xi \times B$ term and the $\delta\Psi$ term.

With the assumption that the displacement of plasma is non-compressional (divergence-free) and perpendicular to $\vec{z}$, it can be expressed as the curl of a function along $\vec{z}$ direction, $\zeta\vec{z}$. In another word, it is equivalent to denote ξ as $\vec{\xi} = \vec{\nabla}\zeta \times \vec{z}$. The above equation is thus expressed as:

$$\begin{aligned}\delta\Psi\vec{z} &= (\vec{\nabla}\zeta \times \vec{z}) \times \vec{B} - \vec{\nabla}\chi \\ &= (\vec{B} \cdot \vec{\nabla}\zeta)\vec{z} - B_z\vec{\nabla}\zeta - \vec{\nabla}\chi\end{aligned}$$

The leading order of the magnetic field along z direction, $B_z = B_{z0} + O(\varepsilon^2)$, is B_{z0}, a constant. We have $B_z\vec{\nabla}\zeta \sim \vec{\nabla}(B_{z0}\zeta)$. The second and third terms in the above equation can thus be merged into a gradient function $\vec{\nabla}f$. All the other terms except $\vec{\nabla}f$ are along direction $\vec{z}$, so should $\vec{\nabla}f$. This implies that f can only be a function of z. Then $\vec{\nabla}f(z) = f'(z)$ is also only dependent on z:

$$\delta\Psi = \vec{B} \cdot \vec{\nabla}\zeta + f'(z) \tag{3}$$

This equation has the same physics meaning as Eq. 2, expressed using $\delta\Psi$ and ζ. It couples the magnetic perturbation with plasma displacement.

The force driving plasma movement comes from pressure and Lorentz force. This gives another equation governing the dynamics of plasma:

$$\begin{aligned}\vec{\nabla} \times \rho\frac{d\vec{v}}{dt} &= \vec{\nabla} \times (\vec{\nabla}P - \vec{j} \times \vec{B}) \\ &= -\vec{j} \cdot \vec{\nabla}\vec{B} + \vec{B} \cdot \vec{\nabla}\vec{j} \end{aligned} \tag{4}$$

Under the reduced MHD assumption, $j_\perp/j_z \sim \varepsilon$, the first term is second order in magnitude: $\vec{j} \cdot \vec{\nabla}\vec{B} \sim j_z\frac{\partial}{\partial z}\vec{B} \sim \varepsilon^2$. The second term has some contributions in the first order:

$$\vec{B} \cdot \vec{\nabla}\vec{j} = \vec{B}_0 \cdot \vec{\nabla}\vec{j} + \vec{B}_1 \cdot \vec{\nabla}\vec{j}_0$$

Let's examine the term $\vec{B}_0 \cdot \vec{\nabla}\vec{j}$ first. The equilibrium magnetic field $\vec{B}_0 = B_{z0}\vec{z} + B_\theta\frac{\vec{e}_\theta}{r} = B_\theta(q\vec{e}_\varphi + \vec{e}_\theta)/r$ has contribution in both z and θ direction. For a perturbation structure taking the form of $f \sim \exp[i(m\theta - n\varphi)]$, a gradient operator on it has the same effect as a linear multiplication:

$$\vec{\nabla} f = (im\vec{\nabla}\theta - in\vec{\nabla}\varphi) f$$

Using the identity that $\vec{e}_i \cdot \vec{\nabla} x^j = \delta_{i,j}$, one obtains a simple expression for the first component in Lorentz force:

$$\begin{aligned}\vec{B}_0 \cdot \vec{\nabla}\vec{j} &= i\frac{B_\theta}{r}(m - nq)\vec{j}_1 \\ &= iF(r)\vec{j}_1\end{aligned}$$

where $F(r) = [m - nq(r)]B_\theta / r$.

For the second term, $\vec{B}_1 \cdot \vec{\nabla}\vec{j}_0$, a symmetric current profile for $\vec{j}_0 = j_0(r)\vec{z}$ can be assumed for simplicity. Then $\vec{\nabla}\vec{j}_0 = \vec{\nabla} r j_0'(r)\vec{z}$ and $\vec{B}_1 \cdot \vec{\nabla}\vec{j}_0 = B_r \vec{j}'(r)$, where $B_r = \vec{\nabla} r \cdot (\vec{e}_z \times \vec{\nabla}\delta\Psi) = -\frac{\vec{e}_\theta}{r} \cdot \vec{\nabla}\delta\Psi$. Under the assumption that the perturbation has the helical form, $\delta\Psi \sim \exp[i(m\theta - n\varphi)]$, one has:

$$\vec{B}_1 \cdot \vec{\nabla}\vec{j}_0 = B_r \vec{j}_0'(r) = -i\frac{m}{r}\delta\Psi j_0'(r)\vec{z}$$

The velocity part in Eq. 4 can be expressed in terms of ζ. According to the definition, the velocity is $\vec{v} = \dot{\xi} = \frac{d}{dt}(\vec{\nabla}\zeta \times \vec{z})$. Assuming the perturbation has a single growth rate, the time dependent part can be expressed as $\zeta(t) \sim \exp(\gamma t)$. By dropping the higher order $\vec{v}\cdot\vec{\nabla}$ term in the d/dt operator, one has $d\zeta/dt \sim \partial\zeta/\partial t = \gamma f$. Combining the derivations above, one obtains the second equation between the plasma displacement and the perturbed magnetic structure:

$$\rho\gamma^2\nabla^2\delta\zeta = iF(r)\nabla^2\delta\Psi - i\frac{m}{r}\delta\Psi j'(r) \tag{5}$$

With the assumptions made to obtain Eq. 5, Eq. 3 can be further simplified. The leading order from $\vec{B} \cdot \vec{\nabla}$ operator on the perturbation term ζ is the same as multiplying it with $iF(r)$. We also notice that the $f(z)$ term in $\delta\Psi$ does not affect the magnetic field through $\vec{B} = \vec{\nabla}\Psi \times \vec{z}$, because $\vec{\nabla} f'(z) \times \vec{z} \sim \vec{z} \times \vec{z} = 0$. Thus it can be safely set to zero: $f(z) \equiv 0$. With regard to these simplifications, the equation becomes:

$$\delta\Psi = iF(r)\zeta \tag{6}$$

These two equations, (5) and (6), serve as the fundamental in reduced MHD theory. Based on these equations, Ref. [17] has derived interesting results about the plasma instability with ideal wall or resistive wall. It assumes a delta function profile of the plasma current $j_0 = j_0\delta(r-a)$. The domain of the solution is then separated by the $r = a$ surface. Within each domain, $\delta\Psi$ is found to satisfy the Laplacian equation, where general analytical solution is readily available. The continuity condition at the surface $r = a$ requires

$$\begin{aligned}
&\delta\Psi(a^+) = \delta\Psi(a^-) \\
&\delta\Psi'(a^+) - \left(1 + \frac{\rho\gamma^2}{F(0)^2}\right)\delta\Psi'(a^-) = -\frac{mj_0}{aF(0)}\delta\Psi(a)
\end{aligned}$$

These constraints are used to match up the solutions from both sides of the surface.

The 3D plasma behavior are thus essentially represented by the physical quantities at the plasma boundary and the wall surfaces. One exampled of the discussion of the plasma instability through this model can be found in Ref. [17]. This reduces the plasma dynamic analysis down to interactions between surfaces and eliminates the work of calculating everything in the volume. Moreover, the representation is based on discrete mode basis functions, which is a better model for the feedback system. This idea is further expand in the following sections to arrive at the core model used by the current feedback system in HBT-EP.

2. *Surface representation and matrix equation*

A rigorous theory that works directly with surface quantities to describe plasma is developed by Boozer[37]. The final result is similar to what is shown above, but with a different approach that doesn't rely on reduced MHD assumptions about small a/R. This theory treats the plasma as a black box inside its boundary. The external field interacts with the plasma by applying a magnetic field at the plasma boundary. The plasma responds back, also through magnetic field, which can be characterized as an effective current flowing on the surface of the plasma boundary. The magnetic field outside the plasma, in the vacuum, is purely governed by the Maxwell's equation, whose solution is determined once the boundary conditions are set. Consequently, the dynamics of the system is characterized by the physics quantities on the plasma surface and the wall surface.

The closed surface of the plasma boundary, the torus, is parametrized by (θ, φ). A set of basis functions $\{f_i(\theta, \varphi)\}$ is used for the function space defined on the surface $x(\theta, \varphi)$. The basis functions are orthogonal to each other with respect to a weighting function w: $\oint f_i^* f_j w da = \delta_{i,j}$, with the constraint $\oint w da = 1$ being satisfied. A specific realization of (θ, φ) or $\{f_i(\theta, \varphi)\}$ is not restricted, as long as these conditions are met.

The flux of the magnetic field through the surface is a scalar function defined on (θ, φ). It thus can be decomposed as

$$\vec{B} \cdot \vec{n} = w \sum_i \Phi_i f_i(\theta, \varphi)$$

The effective current flowing on the surface can be represented by a surface function $\kappa(\theta, \varphi)$ through:

$$\vec{j}(\theta, \varphi) = \vec{\nabla} \times \{\kappa(\theta, \varphi)\delta(r - a)\vec{\nabla} r\}$$

We expand κ with respect to the surface basis functions:

$$\kappa(\theta, \varphi) = \sum_i J_i f_i(\theta, \varphi)$$

Note that the expansion for $\vec{B} \cdot \vec{n}$ has w in it while κ does not. This is for the convenience that when the inner product of these two functions are needed, one will obtain an expression that contains $\oint f_i^* f_j w da = \delta_{i,j}$.

κ represents an effective current distribution, which inherently creates a radial flux $\vec{B} \cdot \vec{n}$. This is viewed as the self-inductance of the surface, and is purely determined by its geometry. The relation between these two functions is characterized by an induction matrix, defined with the vectors $\vec{\Phi} = \{\Phi_i\}$ and $\vec{J} = \{J_i\}$ representing the flux and the effective current:

$$\vec{\Phi} = \overleftrightarrow{L} \cdot \vec{J}$$

This notation is consistent with the usual meaning of inductance.

The notation represents the magnetic energy in the system concisely and is consistent with the classical definition. In the classic definition, the change rate of the magnetic energy is the integration of $\vec{j} \cdot \vec{E}$ over the volume. This is expressed by the surface quantities in the following way:

$$\begin{aligned}
\frac{d\delta W}{dt} &= -\int \vec{j} \cdot \vec{E} d^3x \\
&= -\int \vec{\nabla} \times \{\kappa(\theta, \varphi)\delta(r-a)\vec{\nabla}r\} \cdot \vec{E} d^3x \\
&= \int \kappa(\theta, \varphi)\delta(r-a)\vec{\nabla}r \cdot \frac{\partial B}{\partial t} d^3x \\
&= \oiint \kappa(\theta, \varphi)\frac{\partial}{\partial t}(\vec{B} \cdot \vec{n}) da \\
&= \vec{J} \cdot \frac{d}{dt}\vec{\Phi}
\end{aligned}$$

The surface functions are represented in the vector form in the last step. While the meaning of the vector entries is not as obvious as the classical j and B, the resulted notation is similar to the formula obtained in the standard E&M theory: $d\varepsilon/dt = j \cdot E = j \cdot dB/dt$.

The total flux Φ through the surface of plasma consists of two parts:

- One part comes from the current outside the surface. This is called the external flux Φ_x.

- The other part comes from the current within the surface. This is called the plasma flux $\Phi_p = L_p \cdot J_p$, where J_p is the effective plasma surface current. Note that the effective current is only valid when viewing the plasma response from outside the plasma boundary. In this view, plasma is treated like a black box.

The relation between J_p and Φ will be discussed in Sec. III C. It characterizes the plasma response to outside perturbation.

Other surfaces in the system that interact with the plasma are also considered. They play an important role in the plasma stability analysis. These surfaces include:

- The wall surface surrounding the plasma. The wall can be resistive or ideal depending on the nature of the material and the time scale of interest.

- The sensor surface, where the magnetic sensors are located. This surface does not perturb the plasma, but signals are measured on it.

- The control surface, where external control coils are placed. The control coil currents are viewed as surface current on it.

In the case of HBT-EP, these three surfaces are modelled at the same location because the sensors and control coils are all mounted on the in-vessel stainless steel shells which also serve as the first layer of the resistive wall. The magnetic flux through the wall surface contributed by plasma has a surface representation Φ_{wp}. This defines the mutual inductance matrix $\Phi_{wp} = L_{wp} J_p$. The total flux through the wall is $\Phi_w = L_{wp} J_p + L_w I_w$, where I_w is the surface current on the wall and L_w is the self-inductance matrix of the wall.

While the empirical value of these inductance matrices are usually calculated numerically by 3D codes like VALEN[38], the evaluation is simple under the cylindrical case. In a cylindrical system, we assume again that the perturbation is mostly helical. The basis functions $\{f_i\}$ are labeled by (m, n) with $f_{m,n} = \exp[i(m\theta + n\varphi)]$. They are already orthogonal with respect to the surface integration, so the weighting function w is a constant. Consider the surface at $r = b$, the unity requirement for w implies $w = 1/\oint da = 1/4\pi^2 b R_0$.

Under the assumption with large aspect ratio: $n/R \ll m/r$, one can neglect the $\partial/\partial z$ term in the Laplacian: $\nabla^2 \sim \frac{\partial^2}{\partial r^2} + \frac{1}{r^2}\frac{\partial^2}{\partial \theta^2}$. The magnetic field between surfaces is curl free because $j = \vec{\nabla} \times \vec{B} = 0$ in the vacuum. It thus can be represented as the gradient of a scalar function: $\vec{B} = \vec{\nabla}\phi$. The divergence free condition of $\vec{B}$ becomes $\nabla^2\phi = 0$, which has a well-defined general solution. For the field ϕ that is solely generated by current flowing on the surface $r = b$, it satisfies the constraints that

- ϕ is finite at $r = 0$.
- $\lim_{r\to\infty} \phi(r) \to 0$.

These conditions separate the solution into two domains: one inside the surface $r = b$ and one out side it. The general solution of ϕ is

$$\begin{cases} \phi = \sum \phi_{m,n} \left(\frac{r}{b}\right)^m f^*_{m,n} & r < b \\ \phi = \sum \phi'_{m,n} \left(\frac{b}{r}\right)^m f^*_{m,n} & r > b \end{cases}$$

There are two boundary conditions. First is the continuity of the B_r field, which is expressed as $\phi_{m,n} + \phi'_{m,n} = 0$. The second is the Ampere's law regarding to the surface current and the poloidal field, which is expressed as $\mu_0\kappa = 2\phi_{m,n}f_{m,n}$. This gives the coefficients for the solution:

$$\phi_{m,n} = -\phi'_{m,n} = \mu_0 J_{m,n}/2$$

The self-inductance matrix of the surface $L_{i,j}$ can then be obtained. Since $\vec{B} \cdot \vec{n} = B_r = \frac{m}{b}\phi_{m,n}f^*_{m,n}$, one can calculate the vector representation of the flux:

$$\begin{aligned} \Phi_{m,n} &= \oint \vec{B} \cdot \vec{n} f_{m,n} da \\ &= 2\pi^2 m\mu_0 R_0 J_{m,n} \\ &= L_{m,n,m',n'} J_{m,n} \end{aligned}$$

where $L_{i,j} = 2\pi^2 m\mu_0 R_0 \delta_{i,j}$. As is shown by the expression, this quantity only depends on the geometry of the system.

The $(b/r)^m$ term in the solution of ϕ indicates the decay of the magnetic field strength when propagating between surfaces. For the $r > b$ region, the strength decays with r^{-m}. The higher the m number, the faster it decays. For the coupling between surface $r = a$ and $r = b$, the decay factor $(a/b)^{2m}$ is often encountered in the derivation to denote the coupling between surface a to surface b and then back to surface a again.

The surface representation theory quantifies the physics outside plasma with basis functions that incorporate well with numeric calculation. The eigen vectors of the matrix equation governing the system dynamics can be solved. If the same eigen vectors are chosen as the basis function for surface, f_i, the system is decoupled and each J_i and Φ_i will grow at the time scale determined by the eigen value. Basis functions not orthogonal to each other are sometimes used and the non-zero cross terms need to be evaluated. This is referred as mode coupling because each f_i mode now interacts with other f_j modes and no longer grows independently.

B. Plasma wall interaction

A wall surrounding the plasma provides stabilizing effect. Without the wall, a plasma mode could be naturally unstable and grow at an Alfven time scale. With the existence of the wall, eddy currents are excited by the changing magnetic field generated from the growing mode. These eddy currents will couple back to the plasma and suppress the growth rate of the instability. The ideal wall assumption models the wall as a perfect conductor, which provides the strongest stabilizing effect. A more realistic model, the resistive wall model, takes the wall resistivity into consideration. It allows the magnetic flux to penetrate through the wall, at a much slower time scale compared to the Alfven time, called the resistive wall time. Under such assumption, the fast growth rate of the unstable mode is often reduced down to the resistive wall growth rate. The scale of the wall time depends on the wall thickness, conductivity and geometry. While a full 3D calculation of the resistive wall effect requires numeric code like VALEN[38], one can analyze simple cases with a cylindrical model and gain intuition of the resistive wall effect.

The notation of surface representation is used to represent the mode. Between the plasma surface $r = a$ and wall surface $r = b$, the magnetic field is expressed as $\vec{B} = \vec{\nabla}\delta\Psi \times \vec{z}$. For mode number (m, n), the solution for $\vec{\nabla}^2\delta\Psi = 0$ would be[37]:

$$\delta\Psi = \left(\psi_p\left(\frac{a}{r}\right)^m + \psi_w\left(\frac{r}{a}\right)^m\right)\exp\{i(m\theta - n\varphi)\} \tag{7}$$

$$\text{with} \quad B_r = \frac{im}{r}\left(\psi_p\left(\frac{a}{r}\right)^m + \psi_w\left(\frac{r}{a}\right)^m\right)\exp\{i(m\theta - n\varphi)\}$$

$$B_p = \frac{m}{r}\left(-\psi_p\left(\frac{a}{r}\right)^m + \psi_w\left(\frac{r}{a}\right)^m\right)\exp\{i(m\theta - n\varphi)\}$$

The complex value ψ_p represents the contribution by plasma current from the $r \leq a$ side and ψ_w for that by the wall current from $r \geq b$ side. The following subsections works on different boundary conditions applied to the solution of the mode based on the models used for the wall.

1. *Ideal wall*

The ideal wall models the wall material as the perfect conductor. No magnetic field can penetrate through the wall, meaning $B_r(r = b) = 0$. This condition implies

$$\psi_w = -\left(\frac{a}{b}\right)^{2m}\psi_p \tag{8}$$

Notice that the eddy current represented by ψ_w is passively excited by the plasma current ψ_p. When the magnitude of these two components are measured at the plasma surface $r = a$, the ratio is $|\psi_w/\psi_p| = (a/b)^{2m}$. This ratio is denoted as the coupling coefficient, c, between the wall and the plasma. It will be encountered many times in the later derivations. In a 3D case, the expression for the coefficient c does not have this neat formula. It is usually calculated numerically.

2. Thick resistive wall

The thick wall model assumes that the wall fills the entire volume beyond $r \geq b$. Volume current flows in the space and there is no delta-function-like surface current. The dynamic is governed by the Ampere's law and Faraday's law:

$$\vec{E} = \eta \vec{j} = \frac{\eta}{\mu_0} \vec{\nabla} \times \vec{B}$$

$$\vec{\nabla} \times \vec{E} = -\frac{\partial \vec{B}}{\partial t}$$

Eliminating $\vec{E}$ from the above equations, one obtains:

$$\frac{\partial \vec{B}}{\partial t} - \frac{\eta}{\mu_0} \nabla^2 \vec{B} = 0$$

$$\text{or} \qquad \nabla^2 \Psi + \frac{\mu_0 \gamma}{\eta} \Psi = 0$$

The general solution for Ψ with the cylindrical boundary is

$$\Psi = K_m \left(\sqrt{\frac{\mu_0 \gamma}{\eta}} r \right)$$

The volume current j does not create a jump of magnetic field crossing the boundary, so $\vec{B}(b^+) = \vec{B}(b^-)$. This means that B_p/B_r is continuous across the boundary, implying:

$$\frac{m}{b} \frac{\psi_w - c\psi_P}{\psi_w + c\psi_p} = \left. \frac{\delta \Psi'}{\delta \Psi} \right|_{b^-} = \sqrt{\frac{\mu_0 \gamma}{\eta}} \frac{K'_m \left(\sqrt{\frac{\mu_0 \gamma}{\eta}} r \right)}{K_m \left(\sqrt{\frac{\mu_0 \gamma}{\eta}} r \right)} \tag{9}$$

This is a more complicated boundary condition compared with the ideal wall case. Asymptotic approximations about the Bessel function K_m is used sometimes to obtain a simpler expression.

3. Thin resistive wall

The thin resistive wall model considers the wall as a thin layer that supports the surface current. The actual thickness of the wall l and its conductivity $\sigma = 1/\eta$ is often used together, $l\sigma$, as a single parameter defining the conductivity of the thin wall. The density of the surface current is decomposed into helical patterns. For each helical structure, the total magnetic field $\delta\Psi$ on the domain $r > b$ must follow the form:

$$\delta\Psi_{out} = C\left(\frac{a}{r}\right)^m \exp\left\{i(m\theta - n\varphi)\right\}$$

B_r is continuous across $r = b$. Compare this with the solution $\delta\Psi(r < b)$ expressed in Eq. 7, we have:

$$C = \psi_p + \psi_w/c$$

where $c = (a/b)^{2m}$ is the coupling coefficient. The jump in B_p satisfies the Ampere's law:

$$\delta\Psi'(b^-) - \delta\Psi'(b^+) = \mu_0 j = \frac{l}{\eta}E = -\frac{l\gamma}{\eta}\delta\Psi(b)$$

where we have used $\vec{E} = -\partial\delta\Psi/\partial t = -\gamma\delta\Psi$. Combining the equation obtained from B_r and B_p, we have:

$$\frac{m}{b}\frac{\psi_w - c\psi_p}{\psi_w + c\psi_p} = \left.\frac{\delta\Psi'}{\delta\Psi}\right|_{b^-} = -\frac{m}{c}\left(1 + \frac{cl\gamma}{m\eta}\right) \tag{10}$$

Based on which model is chosen for the wall, Eq. 8, 9 or 10 are obtained accordingly. They all, nevertheless, provide the constraint between ψ_p and ψ_w with a similar format. The response of plasma to the external perturbation shown in Sec. III C provides another relation between ψ_p and ψ_w. The growth rate γ of the instability is solved by combining these two equations.

4. *Plasma rotation*

Plasma rotation affects its interaction with the wall. Viewed with the surface representation, rotation is observed as the transition of energy between the sine and cosine mode with the same (m, n) number, which can be incorporated into the imaginary part of the complex growth rate γ. The real and imaginary part of the representation Ψ, indicates its projection onto the sin and cosine component. The formula shown above thus absorbs the rotation term naturally. With a plasma rotation at a frequency Ω, from the view point of the plasma, the wall is rotating in the counter direction. Under the plasma frame of reference, an extra $i\Omega$ component in γ needs to be added into the equations describing the dynamics of plasma wall interaction. On the other hand, in the wall frame of reference, the plasma response is also affected by the plasma rotation. The plasma rotation modifies the dissipation term and provides stabilizing effect to the mode[6]. The plasma response model, where the plasma rotation enters the equation through the parameter α, is discussed in the next section.

C. Plasma response to external perturbation

The dispersion relation of plasma instability dynamics is completed by including the plasma response to external perturbation, which gives another relation between ψ_p and ψ_w. ψ_p is the effective current distribution on the plasma surface that reproduces the same magnetic field observed from outside plasma. The perturbation is contributed by both walls and control coils. ψ_w represents the wall contribution in perturbation. ψ_x is used to include the additional flux contributed by external control coils. The model discussed in this section is linear, which doesn't describe the full physics inside the plasma. Nevertheless, it is the linearization of the non-linear model with respect to the quasi-equilibrium state. Some empirical parameters will be introduced in the model as the coefficients for the linearization.

This section has two parts. The first part derives the 3rd order dispersion relation where both the resistive wall mode root and the fast rotating kink mode root are included. The second part focuses on the fast rotating kink mode branch that is often observed in HBT-EP. The linear model in this part is used in the feedback system to predict the plasma behavior.

1. *The dispersion relation.*

In this section, the dispersion relation is obtained from a linear model proposed by Boozer[37]. The linear relation is viewed as the first order linearization of a higher order equation. The plasma system is treated as an oscillator system based on the energy principle:[39]

$$[(\gamma + i\Omega)^2 K + (\gamma + i\Omega) D + \delta W_p + \delta W_v^\infty]\psi_a = \delta W_v^\infty \psi_x \tag{11}$$

Here $\psi_a = \psi_p + \psi_x$. Ω is the rotation frequency of plasma. The δW_p is the potential energy displacement for plasma and δW_v^∞ is the potential energy displacement for vacuum without wall. If there is no external interaction with the plasma then $\psi_x = 0$. The system is unstable if $\delta W_p + \delta W_v^\infty < 0$. The stability parameter is defined as:

$$s = -\frac{\delta W_p + \delta W_v^\infty}{\delta W_v^\infty}$$

$s > 0$ implies the plasma is unstable without wall.

With an ideal wall at b, there is coupling between ψ_x and ψ_a similar to Eq. 8. One can move this passive response part to the left of Eq. 11. This is like changing the effective δW_v when there is no other external perturbation. Sometimes δW_v^b is used to denote the effective vacuum energy with the existence of an ideal wall at $r = b$. But this is not another independent coefficient.

The resistive wall condition expressed in Eq. 10 can be re-formulated. Let ψ be the total flux through the wall. Eddy current I on the wall is driven by the induced electric field, generated by the variation of ψ in time. The short form for this relation is $d\psi/dt = -RI$. By expressing ψ and I in terms of ψ_a, ψ_x, through the notations from previous section, one has:

$$\frac{d}{dt}\left[\sqrt{c}(\psi_a - \psi_x) + \frac{\psi_x}{\sqrt{c}}\right] = -\frac{R}{L}\psi_x/\sqrt{c} = -\psi_x/\tau_w\sqrt{c}$$

c is the coupling coefficient mentioned previously, which equals to $(a/b)^{2m}$ in the cylindrical case. L is the self-inductance and $\tau_w = L/R$ is the resistive wall time scale. Substituting d/dt with the single growth rate γ, this relation is expressed as:

$$\begin{aligned}\psi_x &= -\frac{c\gamma\tau_w}{1+\gamma(1-c)\tau_w}\psi_a \\ &= -s_c\frac{\gamma\tau_w^*}{1+\gamma\tau_w^*}\psi_a\end{aligned} \tag{12}$$

where $\tau_w^* = (1-c)\tau_w$ and $s_c = c/(1-c)$.

Combining Eq. 11 and 12, one obtains the dispersion relation for γ:

$$(\gamma+i\Omega)^2\frac{K}{\delta W_v^\infty} + (\gamma+i\Omega)\frac{D}{\delta W_v^\infty} - s + s_c\frac{\gamma\tau_w^*}{1+\gamma\tau_w^*} = 0$$

This is rearranged into a third order polynomial equation:

$$\left[(\gamma+i\Omega)^2\frac{K}{s_c\delta W_v^\infty} + (\gamma+i\Omega)\frac{D}{s_c\delta W_v^\infty} + 1 - \bar{s}\right](1+\gamma\tau_w^*) = 1 \tag{13}$$

where $\bar{s} = s/s_c$. There are three roots in this equation. The branch contributed by the inertia term γ^2 is usually smaller and thus does not need to be analyzed if only the unstable modes are interested.

For fast growing mode branch with $\gamma\tau_w^* \gg 1$, the term in the bracket is equal to $1/(1+\gamma\tau_w^*) \sim 0$. This means $\gamma \sim -\frac{\delta W_v^\infty s_c}{D}(1-\bar{s}) - i\Omega \sim \frac{\gamma_{MHD}^2}{\nu_d}(1-\bar{s}) - i\Omega$. The fast MHD growth rate is defined as $\gamma_{MHD}^2 = \delta W_v^\infty s_c/K$ and $\nu_d = D/K$ is the viscosity coefficient. The coupling coefficient c, determined by the geometry of the wall and plasma, can also be represented by another coefficient $\delta W_v^b(c)$, in context with δW_p and δW_v^∞, as long as the two definitions are consistent. δW_v^b is defined to satisfy:

$$c = \frac{\delta W_v^b - \delta W_v^\infty}{\delta W_v^b}$$

With the new notation, s_c and $1 - \bar{s}$ are expressed in terms of δW_v^b:

$$s_c = \frac{c}{1-c} = \frac{\delta W_v^b - \delta W_v^\infty}{\delta W_v^\infty}$$
$$s_c - s = \frac{\delta W_v^b + \delta W_p}{\delta W_v^\infty}$$

It shows that in the ideal wall case ($\tau_w \to \infty$), the stability of the system is governed by the sign of $\delta W_v^b + \delta W_p$. If it is positive, then one has $1 - \bar{s} > 0$, which results in a stable γ that has non-positive real component. This criteria, when compared with the no wall case, where the stability is governed by the sign of $\delta W_p + \delta W_v^\infty$, shows why δW_v^b is considered as the effective vacuum energy with ideal wall at $r = b$.

In the case of the slow mode branch where $\gamma/\gamma_{MHD} \ll 1$, the first two terms in the bracket can be ignored, and we have

$$\gamma = \frac{1}{\tau_w^*}\frac{\bar{s}}{1-\bar{s}} = \frac{\gamma_w}{1-c}\frac{\bar{s}}{1-\bar{s}} \tag{14}$$

This is the resistive wall mode growth rate.

The root obtained for the RWM growth rate is consistent with the linear relation $(-s + i\alpha)\psi_a = \psi_x$ proposed by Boozer in his model[37]. To see this more clearly, one notice that in obtaining the slow mode root, the first two terms in the bracket in Eq. 13 is ignored. This is the same as ignoring the first two terms in Eq. 11, which results in $-s\psi_a = \psi_x$. Directly combining this with the wall boundary condition in Eq. 12, we have

$$s = s_c \frac{\gamma\tau_w^*}{1 + \gamma\tau_w^*}$$

This is the same solution as expressed in Eq. 14.

In case of large dissipation, one keeps the imaginary part of the $(\gamma + i\Omega)D$ term in Eq. 11. Define

$$\alpha = Im[\gamma + i\Omega]\frac{D}{\delta W_v^\infty}$$

The equation becomes $(-s + i\alpha)\psi_a = \psi_x$. Combining this with Eq. 12, one obtains the growth rate with plasma rotation:

$$s - i\alpha = s_c \frac{\gamma\tau_w^*}{1 + \gamma\tau_w^*}$$

$$\rightarrow \qquad \gamma = \frac{\gamma_w}{1-c}\frac{\bar{s} - i\bar{\alpha}}{1 - \bar{s} + i\bar{\alpha}}$$

Here $\bar{\alpha} = \alpha/s_c$. Under such definition, α is linearly dependent on the imaginary part of γ, with an offset term depending on the plasma mass rotation frequency Ω.

It is important to note that the fast rotating kink mode observed in HBT-EP does not belong to the slow mode branch. When perturbation is applied by the feedback system, however, all eigen modes can be excited. Careful use of the control coils is needed to ensure that other branches of the mode does not become unstable while the feedback system is suppressing the fast rotating kink mode.

2. *HBT-EP model for the fast rotating kink root.*

The fast rotating kink branch ($\gamma\tau_w^* \gg 1$) of the dispersion relation is further discussed in this section. This single helicity linear model for external kink mode dynamics has also been described in [19, 31, 39, 40]. It assumes a frequency-independent dissipation rate, ν_d, a natural mode rotation rate, Ω, and the stability parameter, s, which are determined by experimental observation[39, 41]. The coupling between the perturbed currents flowing on the plasma surface and the eddy currents flowing in the wall requires computation of the coefficient, $0 < c < 1$, through the VALEN code[38].

When the plasma dissipation is large enough compared to the ideal kink mode growth rate, $\nu_d \sim \gamma_{\mathsf{MHD}}^2/\Omega$, the inertia term in Eq. 13 can be dropped, the combined dynamics of the plasma and wall is modelled by a two-dimensional linear system[32, 39], even when the plasma operates near the ideal wall stability limit, $\bar{s} \equiv s/s_{\mathsf{crit}} \sim 1$.

This linear system is

$$
\frac{d}{dt}\begin{pmatrix}\psi_a\\ \psi_w\end{pmatrix}=\begin{pmatrix}(1-\bar{s}+i\bar{\alpha})\frac{\gamma_{\mathsf{MHD}}^2}{\nu_d} & -\frac{\gamma_{\mathsf{MHD}}^2}{\nu_d\sqrt{c}}\\ \frac{\gamma_w\sqrt{c}}{1-c} & -\frac{\gamma_w}{1-c}\end{pmatrix}\begin{pmatrix}\psi_a\\ \psi_w\end{pmatrix}+\begin{pmatrix}-\frac{c_f}{\nu_d}\gamma_{\mathsf{MHD}}^2\\ \gamma_w(1-\frac{cc_f}{1-c})\end{pmatrix}\psi_c \tag{15}
$$

The symbols c, c_f, and γ_w are the VALEN-computed parameters associated with the close-fitting conducting wall, and these parameters are listed in Ref. [32]. The critical stability parameter for a kink mode surrounded by an ideal wall is $s_{\mathsf{crit}} \equiv c/(1-c)$. The stability parameter, $\bar{s}$, is the ratio of the total perturbed energy of the ideal kink mode without a wall to the change in vacuum energy with and without a wall. The normalized torque parameter, $\bar{\alpha} \equiv v_d\Omega/\gamma_{\mathsf{MHD}}^2$, represents the friction-like dissipation of the helical perturbation, and $\bar{\alpha} \sim 2$ in HBT-EP[39].

The control coil current is proportional to the control flux, $\psi_c = M_c I_c$, where $M_c \approx 2.3\mu$H. When the control coil current is switched off, Eq. 15 is a second-order system with two modes. When $\bar{s} < 0$, both modes are damped oscillations. When $\bar{s} > 0$, one mode becomes unstable, with characteristics depending upon $(\bar{s}, \bar{\alpha})$. For slowly rotating modes and small $\bar{s}$, the unstable mode is called the resistive wall mode with a growth rate $\gamma \approx \gamma_w(\bar{s} - i\bar{\alpha})/(1-c)$. This is consistent with the result obtained in the previous model. When $\bar{s} \sim 1$, the fast rotating kink mode is unstable with $\gamma \approx i\Omega + (\gamma_{\mathsf{MHD}}^2/\nu_d)(\bar{s}-1)$. In the HBT-EP tokamak, the fast kink mode is naturally unstable while the resistive wall mode is usually rotationally stable. The feedback system mainly deals with the fast rotating kink mode.

In the active feedback control, ψ_c is driven by a linear amplifier in response to the measurements of the perturbed flux variables, (ψ_a, ψ_w). The implementation of current control feedback, discussed in Sec. IV D, creates a small effective time delay, proportional to $\omega_{\mathsf{eff}}^{-1}$, and this delay is modeled with a single pole response. Measurements of the perturbed poloidal magnetic field, δB_p, at the radius of the wall segments, are used as sensor inputs for the closed-loop feedback control. Using the vacuum representation of the perturbed poloidal field, $\delta B_p = i(m/r_w)(2\sqrt{c}\psi_a - (1+c)\psi_w)/(1-c)$, the implementation of a phase shifted proportional gain current-control feedback introduces the third linear equation:

$$\psi_c + \frac{1}{\omega_{\mathsf{eff}}}\frac{d\psi_c}{dt} = ge^{i\triangle\phi}\frac{im}{r}(\frac{2\sqrt{c}}{1-c}\psi_a - \frac{1+c}{1-c}\psi_w) \tag{16}$$

where g is the feedback gain (in units of meters, or flux per Tesla), and $\triangle\phi$ is the desired toroidal phase shift between the quadrature detection of δB_p and the applied helical control flux, ψ_c. Analysis of the third-order system, Eq. 15 and 16, were presented in previous simulations of active feedback control in HBT-EP[31, 32], except $\omega_{\mathsf{coil}} \ll \omega_{\mathsf{eff}}$ was used because the voltage-control feedback does not compensate for the control coil self inductance.

A root locus plot illustrating how the dominate roots, for this third-order system, move with respect to proportional gain is shown in Fig. 9. This figure, compared directly with Fig. 14 of Ref. [32], shows the closed-loop system's responses as a function of g and $\triangle\phi$, with enhanced ω_{eff}. The feedback system can accelerate, decelerate, amplify, and suppress the mode depending on the applied phase shift $\triangle\phi$, which is consistent with the experimental observations obtained previously with other control system[42, 43]. Mode suppression is achieved with a phase shift larger than the acceleration value and smaller than the deceleration value. This observation is used to search for the suppression parameter settings empirically during the experiment. While the theory predicts a sine-like variation of the growth rate depending on the phase shift, the phase margin for suppression observed experimentally is usually narrow.

Most importantly, this plot shows the current control compensation, which changes $\omega_{\mathsf{eff}}/2\pi$ from 4.3kHz to 20kHz, has eliminated the excitation of the slow mode. In contrast to Fig. 14 shown in Ref. [32], the eigenvalue with the smaller imaginary value, the slowly rotating mode, is not excited by the closed-loop feedback at the gain used for fast mode suppression in the new algorithm. This explains why the improved

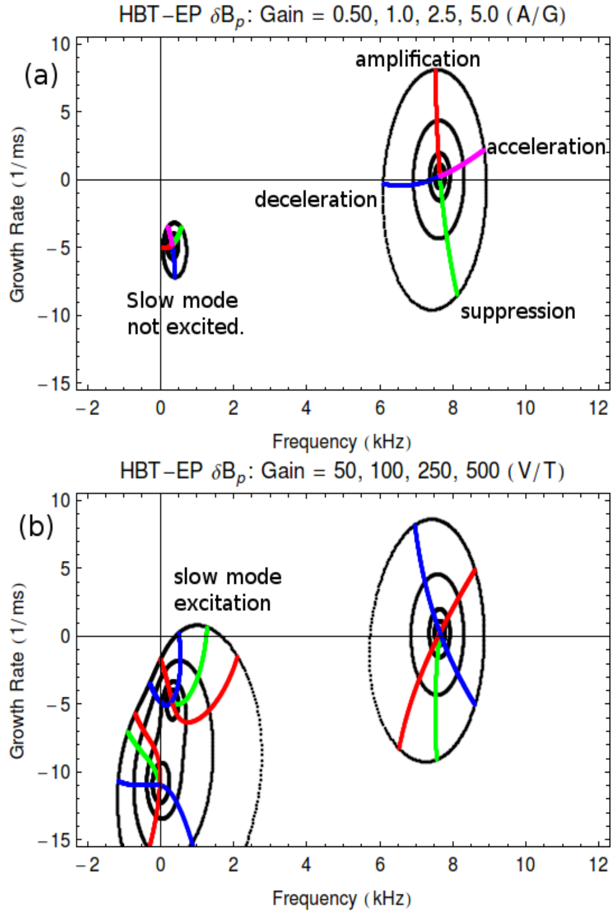

Figure 9. (a)The two eigenvalues with respect to different proportional gains and phase shifts. For each colored line, the phase shift $\triangle\phi$ is fixed while the gain, g, increases. For each black circle, g is fixed and $\triangle\phi$ is scanned. As the phase shift $\triangle\phi$ varies, the system goes through each of the four scenarios: deceleration, amplification, acceleration, and suppression. The gain assumes the control coils cover the full plasma surface. In the actual experiment, the control coils only cover the outboard area of the plasma. (b) Voltage control, adapted and reprinted with permission from Rath *et al*[32] for comparison. The positive direction of rotation is changed to be consistent with (a). The third root in (a) is very strongly damped and is outside the boundary.

feedback system can achieve mode suppression at all frequency.

The optimal phase shift for suppression (i.e. the $\triangle\phi$ at which the $Re(\gamma)$ is smallest) varies slightly depending on $\bar{\alpha}$, as is shown in Fig. 10. This observation is corroborated by the experimental results shown later in Fig. 21, where the plasma is slowed by the bias probe.

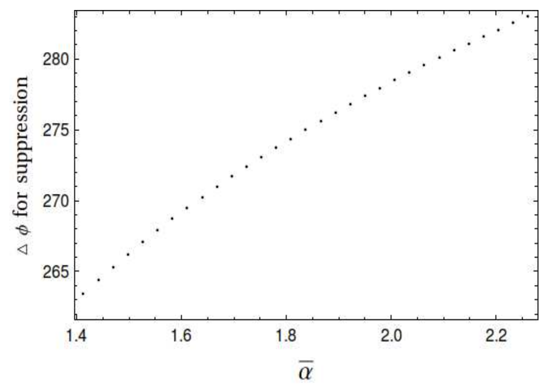

Figure 10. The optimal phase shift $\triangle\phi$ for suppression versus $\bar{\alpha}$. For each given $\bar{\alpha}$, a phase scan with gain = 1 A/Gauss is performed and the $\triangle\phi$ with the smallest $Re[\gamma]$ is plotted.

IV. FEEDBACK SIGNAL PROCESSING IN HBT-EP

Perturbation on the plasma through control coils are driven by the feedback system in HBT-EP, which is a GPU-based platform using NVIDIA GTX580 card to parallelly process the signals measured by the magnetic sensors around the plasma. This system was designed by Rath[23] and then improved by the author of this thesis. The system currently takes 40 poloidal sensors, 40 radial sensors as input signal; its output drives 40 in-vessel control coils and 1 bias probe. The signals are measured every 6μs. The total latency between the time when a signal is measured to the time of the control coil response, is 22μs.

An overview of the hardware and software logic of the system is discussed first. Later sections focus on the critical issues encountered in feedback suppression of plasma instability. Through careful design of the algorithm, the system keeps accurate phase difference $\triangle\phi$ between the measured mode and the applied perturbation, which has resulted in longer duration of the mode suppression window and elimination of previously observed slow mode excitation.

A. Hardware overview

The hardware of the system is shown in Fig. 11, which consists of three major components:

- The observer, which collects signals from plasma. The magnetic sensors measure the induced electric field, and then transfer them through CPCI boards to the analog-digital-convertor. They are the observer of the system.

- The signal processing component. It processes the signals from input and calculates what perturbation should be exerted to the plasma. The computer, called Caliban, equipped with a commercialized Nvidia GPU card for the parallel processing, is the main part of this component.

- The actuator. It receives output signal from GPU and realizes the perturbation to the plasma. The control coils, bias probe and the amplifiers driving them all belong to this component.

The observer takes measurement from 40 radial and 40 poloidal magnetic sensors. These sensors are essentially looped coils to measure the induced electric field generated by the variation of the magnetic flux through the loops. They measure the value of $\oint h(\vec{x})\vec{B}\cdot d\vec{l}$, where the loop integral is poloidally around the plasma. The 40 radial/poloidal sensors are mounted on the inner side of the shells facing the plasma. Their measurements are treated as point value estimations of the magnetic field at the location of the sensors. Because of the eddy current effect from the shells, the radial magnetic field is shielded by the wall when the mode is fast rotating. The magnitude of the signals detected by radial field sensors are usually seven times smaller than that detected by the poloidal sensors. The voltage signals from these sensors are collected by ACQ196, the analog to digital converter, and then sent to the signal processing component.

The signal processing component is a standard PC equipped with the commercial NVIDIA video card GTX580. When the feedback system is operating during a plasma

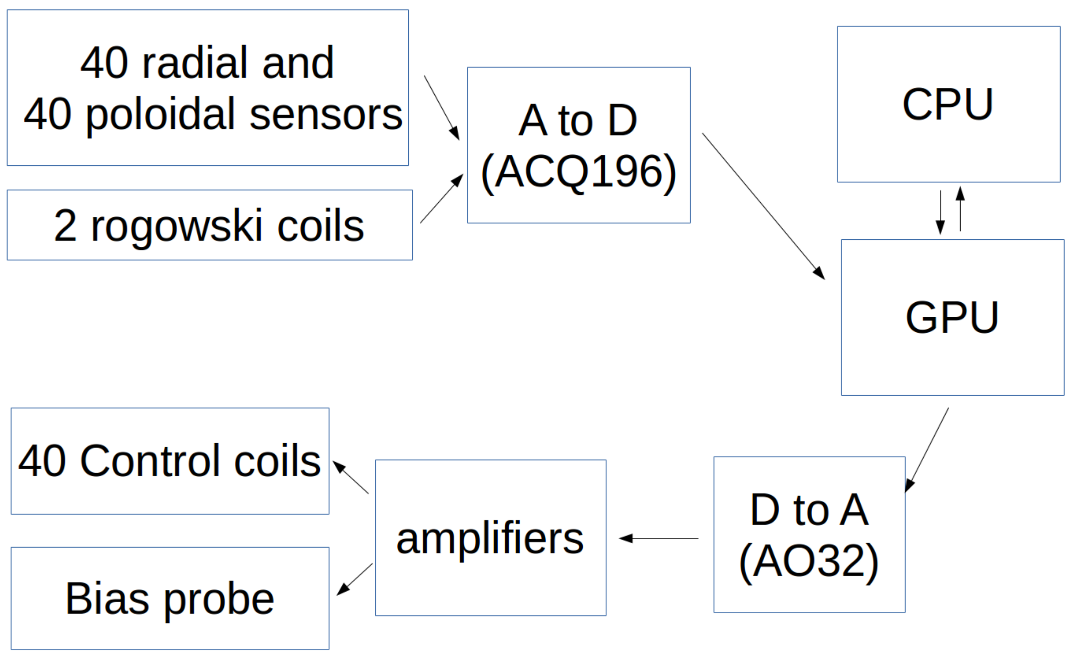

Figure 11. Illustration of the hardware in the feedback system.

discharge, the data received by ACQ196 is transferred in real-time directly to the memory of the GPU through the PCIe bus. Currently, up to 82 threads run in parallel to process the data and calculate the desired perturbation on plasma. The output data is sent to the AO32 devices, which convert signals from digital to analog.

The actuator component receives signals from the AO32 devices and drives the control coils/bias probe through amplifiers. The control coils are looped coils mounted on the shells. Driving current through these coils creates external magnetic field to perturb the plasma. The control coils, as the load to the amplifiers, have a high inductance/resistance ratio. This results in a smoothing effect on the output waveform when the signals are fast changing. Recognizing this and handling this effect in the feedback algorithm have made significant improvement to the performance. The bias probe penetrates under the plasma boundary. Actively changing the voltage potential on this probe can create an radial current and a $J \times B$ force that will drive the plasma rotation. The capability of active feedback on this voltage has been demonstrated, but the feedback algorithm discussed in this thesis does not use this feature. For most of the experimental results in this thesis, the bias probe voltage is set before the discharge. This sets different plasma rotation configuration for tests on the feedback system.

B. Software overview

The software structure of the feedback system is very flexible, which allows easy and systematic modification. Most of the system parameters are set in the python file fbsettings.py. It incorporates the human friendly parameters into many pre-calculated matrices. Any change in this file is applied properly and consistently across the system. All the pre-computed values will be written as the header file format in fbsettings.h. Other C++ or CUDA code will include this header file to use these values directly in the compiled executable. The core feedback algorithm is implemented in the gpu_fb.cu file, a CUDA file for parallel computation on GPU. The do_fb.cpp file initializes the system and connects the ACQ196 and AO32 devices with the GPU system. It can also switch the system between production mode and debug mode. The fbtools.py file implements some algorithms for mode matrix construction and post-discharge analysis. Details of these files are shown in Appendix III.

C. Signal fitting method

In experiment, the direct measurement from sensors need to be preprocessed to obtain the input signal applicable for system model. An important improvement in the feedback algorithm involves separation of fluctuation signal from equilibrium signal. Taking the magnetic sensor reading for example, it measures the total B field along poloidal/radial direction at the sensor location, which not only includes the magnetic field coming from the perturbing field, but also includes the equilibrium field coming from the vertical field coils or the plasma equilibrium current. The feedback system is only interested in the perturbing field. The equilibrium field evolves during the whole discharge, at a slower time scale compared with the perturbation signal. To separate them, the slowly changing equilibrium signal contribution to the total mixed signal needs to be estimated. Previously, this was done using a moving window average method. It keeps the entire history of the measured data and updates the windowed averaging result as new signal arrives. For each mode component, the time series has around two thousand data points for a discharge, which must be stored as an array on the shared memory of the GPU. The new algorithm uses a band pass filter instead, which only stores one scalar value for each order of the filter. The two methods produce similar results for the equilibrium fitting, but the scalar value used by the latter method can be stored as local registers for each thread, providing faster read/write speed, resulting in reduced computation time. Interpretation of the band pass filter under the equilibrium fitting context is shown in this section.

The concept of equilibrium estimation in the feedback system must be understood in the context of real time calculation. Unlike post-discharge analysis, to estimate the equilibrium at any given time, one cannot use the data 'in the future'. For example, if we need to estimate the equilibrium component of signal $f(t)$ at time $t = t_0$, then only the data for $t \leq t_0$ will be available. In the windowed averaging method, the target estimation time is set at the right end point of the window to satisfy this requirement. This requirement is satisfied by the band pass filter method.

1. Low/High pass filter

Lets first investigate the theory about a first order low/high pass filter. The input/output of the filter is described by a simple equation. For a first order low pass filter, assuming f is the input signal, the output signal g will satisfy:

$$g + \frac{1}{\alpha}\frac{dg}{dt} = f \tag{17}$$

where α is the single coefficient governing the filter. The analytical solution for g

can be expressed as an integral on f:

$$g(t) = \alpha \int_0^\infty f(t-s)e^{-\alpha s} ds$$
$$= \alpha \int_{-\infty}^t f(s)e^{-\alpha(t-s)} ds \tag{18}$$

We can denote this formula as $g = L_\alpha[f]$. The function $g(t)$ is a weighted average of $f(s)$ for $s < t$. For the high pass filter with the same coefficient α, the output will be $(1 - L_\alpha)[f]$. If we take $g(t)$ as the equilibrium estimation on signal $f(t)$, then the remaining component $f - g = (1 - L_\alpha)[f]$ is the fluctuation signal. This shows that we can apply a first order high pass filter on the total magnetic signal to obtain a rough estimation of the fluctuation part contributed by the rotating mode.

A simple numerical implementation can be constructed for the low pass filter in the discrete signal case. If the function of $f(t)$ is discretely sampled at every $N\triangle t$, then one can construct $\tilde{g}$ at the every time point incrementally, using:

$$\tilde{g}[(N+1)\triangle t] = \tilde{g}(N\triangle t)e^{-\alpha\triangle t} + \frac{1 - e^{-\alpha\triangle t}}{\alpha} f[(N+1)\triangle t] \tag{19}$$

This discrete implementation converges to Eq. 18 as $\triangle t \to 0$. For the high pass filter, one can use the same formula, but output $f - g$ instead of g.

When running in real time, the filter does not need to store all the past data of g or f. It stores the current $g(N\triangle t)$ value in a variable and updates it every time the new $f(t)$ arrives. The coefficient $e^{-\alpha\triangle t}$ and $(1 - e^{-\alpha\triangle t})/\alpha$ can be computed beforehand once α is determined.

2. Linear fitting with exponential weight

Simple first order low/high pass filter method points out a good direction in equilibrium signal estimation. The results are not very satisfactory. This section interprets the formula under a generalized estimation context. A better estimation method is then derived, which is currently used in the feedback system.

The equilibrium estimation problem can be formulated under an optimization context. Given a function f, at any time point t, one can pick a constant a as the equilibrium estimation for f on $t < s$. The estimation is optimized by minimizing the function:

$$I(t,a) = \int_0^{\infty} (f(t-s) - a)^2 e^{-\alpha s} ds$$

As is shown in Fig. 12, the equilibrium is a constant function at the level of a. The difference between $f(t)$ and a is weighted with $e^{-\alpha s}$, where s is the time distance to current time t, and α is the decay factor. This optimization is evaluated at every time point t, so we can obtain a trace of a depending on t as the new information of f comes in.

Minimizing the penalty function with $\partial I/\partial a = 0$ leads to:

$$\begin{aligned} & \int_0^{\infty} f(t-s)e^{-\alpha s} ds = a \int_0^{\infty} e^{-\alpha s} ds = a/\alpha \\ \rightarrow \quad & a = \alpha \int_0^{\infty} f(t-s)e^{-\alpha s} ds \end{aligned}$$

The solution is the same as the expression given by low pass filter in Eq. 18. This shows that the output of a first order low pass filter $g(t)$ is effectively the same as, at each time point t, fitting the past signal $f(t)$ to one constant value equilibrium with exponentially decaying weight.

The equilibrium signal is slowly evolving, and using a constant function as the target is probably not a good idea. Substituting it with a linear function is one natural improvement. At each time point t, we can estimate the equilibrium part of the past signal $f(t-s)$ with the linear function $a + bs$. This function is valued at a at time t and the slope is $-b$, with respect to t, as is shown in Fig. 12. The penalty function for this optimization is:

$$I(t,a,b) = \int_0^{\infty} (f(t-s) - a - bs)^2 e^{-\alpha s} ds$$

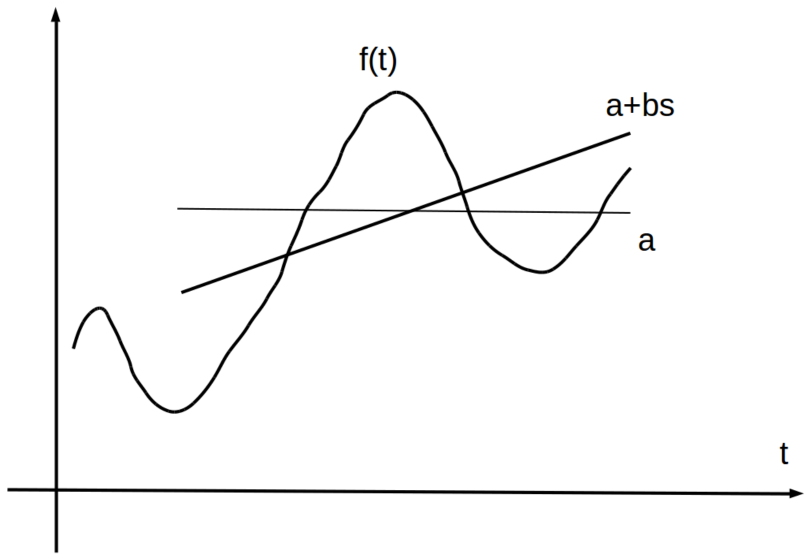

Figure 12. An illustration of the fitting method with exponentially decaying weight. Both fitting with constant function a and with linear function $a+bs$ is shown.

The minimization condition requires $\partial I/\partial a = 0$ and $\partial I/\partial b = 0$, which imply:

$$
\begin{aligned}
a\int_0^\infty e^{-\alpha s}ds + b\int_0^\infty se^{-\alpha s}ds &= \int_0^\infty f(t-s)e^{-\alpha s}ds \\
a\int_0^\infty se^{-\alpha s}ds + b\int_0^\infty s^2e^{-\alpha s}ds &= \int_0^\infty f(t-s)se^{-\alpha s}ds
\end{aligned}
$$

The integration part not involving $f(t)$ can be computed with the following identities:

$$
\begin{aligned}
\int_0^\infty e^{-\alpha s}ds &= 1/\alpha \\
\int_0^\infty se^{-\alpha s}ds &= -\frac{\partial}{\partial\alpha}(\int_0^\infty e^{-\alpha s}ds) = 1/\alpha^2 \\
\int_0^\infty s^n e^{-\alpha s}ds &= \Gamma(n+1)/\alpha^{n+1} = n!/\alpha^{n+1}
\end{aligned}
\tag{20}
$$

This gives:

$$
\begin{aligned}
a + \frac{b}{\alpha} &= \alpha \int_0^\infty f(t-s) e^{-\alpha s} ds = K_1 \\
a + 2\frac{b}{\alpha} &= \alpha^2 \int_0^\infty f(t-s) s e^{-\alpha s} ds = K_2
\end{aligned}
\tag{21}
$$

The solution for the equilibrium function is: $a = 2K_1 - K_2$ and $b = \alpha(K_2 - K_1)$. In the above formula, $K_1 = L_\alpha[f]$ is the result of a first order low pass filtering on f. Interestingly, the expression for K_2 satisfies the following:

$$
\begin{aligned}
& K_2 = \alpha^2 \int_{-\infty}^t f(s)(t-s) e^{-\alpha(t-s)} ds \\
\rightarrow \qquad & \frac{dK_2}{dt} = \alpha K_1 - \alpha K_2 \\
\rightarrow \qquad & K_2 + \frac{1}{\alpha}\frac{dK_2}{dt} = K_1
\end{aligned}
\tag{22}
$$

This implies $K_2 = L_\alpha[K_1]$, meaning that K_2 is also the result of low pass filtering on K_1.

At each time t, one can estimate the equilibrium function using past signal $f(s)$, for $s \leq t$. The value of the linear equilibrium function at time t is just $a = 2K_1 - K_2$. Evaluate a at each time point, one obtains the trace $a(t)$ as the estimated equilibrium signal.

In most situations, the feedback system is mostly interested in the fluctuation part of the signal: $f - a = f - 2K_1 + K_2$. One can verify that

$$
\begin{aligned}
& (1 - L_\alpha)^2[f] \\
&= (1 - L_\alpha)(f - K_1) \\
&= f - K_1 - (K_1 - K_2) \\
&= f - 2K_1 + K_2
\end{aligned}
$$

Since $1 - L_\alpha$ is the high pass filter operator, the above formula implies that the fluctuation signal can be obtained by directing high pass filtering the signal f twice consecutively. This method is used in the feedback system to extract the perturbation signal of the rotating mode from the total magnetic field signal. Each high pass filter is implemented with formula described in Eq. 19.

The above optimization method also provides an estimation for the slope of the equilibrium signal. The parameter s goes in the opposite direction of t, so the slope of the equilibrium implied by function $a + bs$ is actually $-b = \alpha(K_1 - K_2)$. With Eq. 22, we can express $-b$ as:

$$-b = \alpha(K_1 - K_2) = \partial_t K_2 = \partial_t L_\alpha^2 f = L_\alpha^2[\partial_t f]$$

The commutability between ∂_t and L_α is clear by taking derivative of t on both sides of Eq. 17. This expression is used for implementation in the feedback algorithm. Estimation of the frequency of the mode rotation is obtained from the mode's phase trace with respect to time.

3. *Formula for discrete signals*

Most of the expression discussed above uses continuous time, which implies the input data is defined at every time point. Practically, the signal is measured discretely in time. The current feedback system in HBT-EP has a sampling period $\triangle t = 6\mu$s. The rigorous formula can be obtained by re-designing the penalty function to adapt the discrete time nature of the input data. Let the input function to only have data at discrete time points $t_k = k\triangle t$. Assume the estimated equilibrium has the form $\sum_{j=0}^{n} c_j(k\triangle t)^j$, where we have used a more general order n polynomial format. The penalty function can be constructed as:

$$I(t_j) = \sum_{k=0}^{\infty} \left(f(t_{j-k}) - \sum_{j=0}^{n} c_j (k\triangle t)^j \right)^2 \triangle t e^{-\alpha k \triangle t}$$

This converges to the continuous time version as $\alpha \triangle t \to 0$.

In the case of using linear function as estimation for equilibrium, $c_k = 0$ for $k \geq 2$. The minimization of penalty function requires:

$$I_0 c_0 + I_1 c_1 = K_1/\alpha$$
$$I_1 c_0 + I_2 c_2 = K_2/\alpha^2$$

where the coefficients I_i are defined as following:

$$\begin{aligned}
p &= e^{-\alpha \triangle t} \\
I_0 &= \sum_{k=0}^{\infty} \triangle t e^{-\alpha k \triangle t} = 1/(1-p) = \frac{\triangle t}{1 - e^{-\alpha \triangle t}} \\
I_1 &= \sum_{k=0}^{\infty} k \triangle t^2 e^{-\alpha k \triangle t} = \frac{p \triangle t}{1-p} I_0 = \frac{\triangle t}{e^{\alpha \triangle t} - 1} I_0 \\
I_2 &= \sum_{k=0}^{\infty} (k \triangle t)^2 \triangle t e^{-\alpha k \triangle t} = \frac{2p\triangle t}{1-p} I_1 + \frac{p(\triangle t)^2}{1-p} I_0 \\
&= \frac{2(\triangle t)^2}{(e^{\alpha \triangle t} - 1)^2} I_0 + \frac{(\triangle t)^2}{e^{\alpha \triangle t} - 1} I_0
\end{aligned}$$

These expressions are independent of the input signal f. The functions K_1 and K_2 are defined as:

$$K_1 = \alpha \sum_{k=0}^{\infty} f(t_{j-k}) e^{-\alpha k \triangle t} \triangle t$$
$$K_2 = \alpha^2 \sum_{k=0}^{\infty} f(t_{j-k}) (k \triangle t) e^{-\alpha k \triangle t} \triangle t$$

Just as discussed in Sec. IV C 1, the implementation does not need to keep tract of all the past data. The value of of K_1 and K_2 up to time are stored as two variables and updated every time the new information about f arrives. The incremental update formulas for these values are:

$$K_1(t_{j+1}) = e^{-\alpha\triangle t}K_1(t_j) + \alpha\triangle t f(t_{j+1})$$
$$K_2(t_{j+1}) = e^{-\alpha\triangle t}K_2(t_j) + \alpha\triangle t e^{-\alpha\triangle t}K(t_j)$$

These converge to their continuous time version as $\alpha\triangle t \to 0$.

When solving for c_0, c_1, note that $I_1 \sim I_0/\alpha$ and $I_2 \sim 2I_0/\alpha$. To make the entries in the matrix of same order, one can solve

$$\begin{pmatrix} \alpha I_0 & \alpha^2 I_1 \\ \alpha^2 I_1 & \alpha^3 I_2 \end{pmatrix} \begin{pmatrix} c_0 \\ c_1/\alpha \end{pmatrix} = \begin{pmatrix} K_1 \\ K_2 \end{pmatrix}$$

to get the coefficient for c_0 and c_1/α. The inversion of the square matrix is computed only once, before processing the input signal. K_1 and K_2 will be updated in real time.

In the feedback system, we use $(1 - L_\alpha)^2[f]$ to estimate the equilibrium signal in f and $L_\alpha^2[\partial_t f]$ for the slope of it. Where the bandpass filter operator L_α is implemented by Eq. 19 on the discrete signal. The formula is supposed to be consistent with $f - 2K_1 + K_2$ and $\alpha(K_1 - K_2)$. However, if one simply uses the definition given by Eq. 21, and approximate the integration with discrete input, the traces would not match well because f should actually be considered as step function. The formula for K_1 and K_2 obtained here, considering the input f as discrete, gives the result that matches better with the traces obtained by bandpass filter operator.

D. Actuator design

Applying the perturbation with correct phase and magnitude to the plasma is important for successful feedback control. As is shown in Sec. IV A, the control coils in the feedback system are driven by amplifiers, which receive requests from the signal processing component. The waveform of the actual current on the coil, however, does not follow exactly with the waveform of the requested signal. This is because the control coils, as the load in the output circuit of the amplifiers, have a high inductance/resistance ratio. The inductive part resists quick variations in the coil current, hence smooths the signal. This has caused trouble in the previous version of the feedback system. As the gain is increased, the feedback system excited a slowly rotating mode. It becomes dominant quickly that the system loses track of the original mode. Because the settings used to suppress the fast rotating mode do not suppress this slow mode, the performance of feedback suppression is not satisfactory. This is the result of control coils failing to accurately apply the requested perturbation.

To overcome this issue, the improvement in the actuator design has been focusing on this scenario. The smoothing effect is now compensated on the output signal from the GPU. For example, if the desired current is $I_0(t)$, then the output signal would be $V(t)$ such that, after the smoothing effect, the actual realized current I on the coil will follow $I_0(t)$. This method is referred to as "current control". The comparison of a control coil's current between this method and the previous method, voltage control, is shown in Fig. 13. The successful implementation of this current control feedback method on a GPU platform is a major result of this thesis.

The compensation in current control is done by modeling the smoothing effect as a RL circuit. Assume the output circuit for the amplifier has resistance R and inductance L, then the relation between the output voltage V and the coil current I is:

$$I + \frac{L}{R}\frac{dI}{dt} = V/R$$

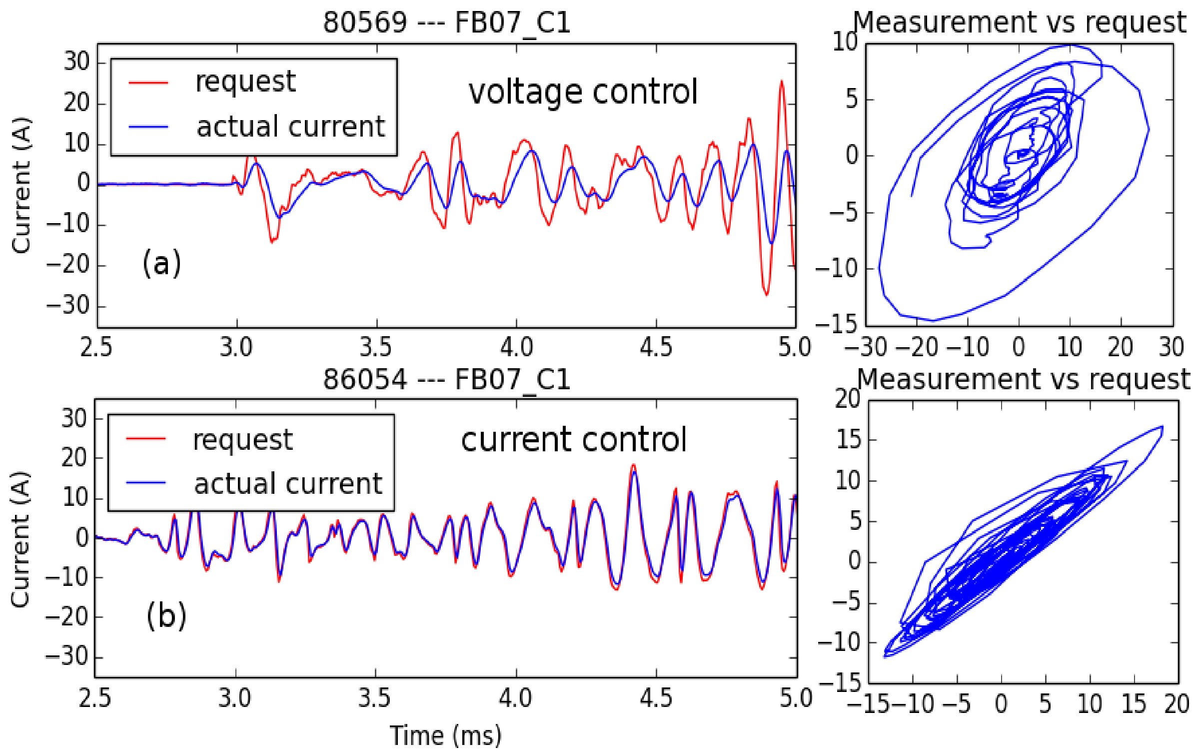

Figure 13. Comparison between current control and voltage control. The realized current is smoothed from the voltage signal sent to amplifier, as is shown in part (a). If the smoothing effect is compensated, the realized current will follow the desired waveform.

This is the same as a low pass filter relation: $I = L_{R/L}[V/R]$. For simplicity, rescale $R = 1$ and let $\omega_0 = R/L$ in the model. A circuit with the same amplifier and control coil is tested on the bench to record its performance with input request at a similar time scale as that in experiment. The data is then used to fit the parameter ω_0 for the transfer function model. It is found that $\omega_0/2\pi = 4.3$kHz characterizes the relationship well. In the experiment, the perturbation signal contributed by the rotating mode has a typical frequency around 7kHz, well above $\omega_0/2\pi$. This explains the noticeable smoothing effect introduced by amplifiers in the feedback system.

The smoothing effect must then be compensated such that experimental signals with the typical frequency around 7kHz can maintain its waveform through the amplifier. If the desired signal for the coil current is I_0, then the driving voltage of the amplifier V_1 must be compensated such that the actual current, $I_1 = L_\omega[V_1]$ will follow

I_0. Directly setting $V_1 = I_0 + \frac{1}{\omega_0}\frac{dI_0}{dt}$ will yield $I_1 = I_0$. But this is not practical because the formula will amplify the noise in I_0. A more approachable way is to compensate through a lead-lag mechanism where high frequency noise is not amplified. If we can ensure $I_1 = L_{\omega_1}[I_0]$ where $\omega_1/2\pi$ is set to 20kHz, well beyond the frequency range of typical experimental data, then the wave form of the requested signal is maintained through the transformation. This implies two equations:

$$I_1 + \frac{1}{\omega_0}\frac{dI_1}{dt} = V_1$$
$$I_1 + \frac{1}{\omega_1}\frac{dI_1}{dt} = V_0$$

eliminating I_1 in the equation array gives:

$$V_1 = \omega_1 \int_0^t (V_0 - V_1)ds + \frac{\omega_1}{\omega_0}V_0 \tag{23}$$

This is the formula used to compute V_1, the compensated voltage input for transformers driving control coils. In previous design by Rath[32], the compensation is done based on the estimated frequency of the rotation, which does not work well when the rotation frequency is not steady. With this method, the realized coil current I_1 follows the requested waveform closely. This is shown in Fig. 13.

E. The feedback algorithm

This section summarizes the feedback algorithm that is implemented in the feedback system. The algorithm is improved upon the previous version shown in [32]. The underlying physics model is not changed in the new algorithm. The improvement is focused on measuring the signal and applying the perturbations more accurately and efficiently. A simple block diagram for the algorithm is shown in Fig. 14.

The feedback system uses the physics model described in Sec. III C 2. The naturally

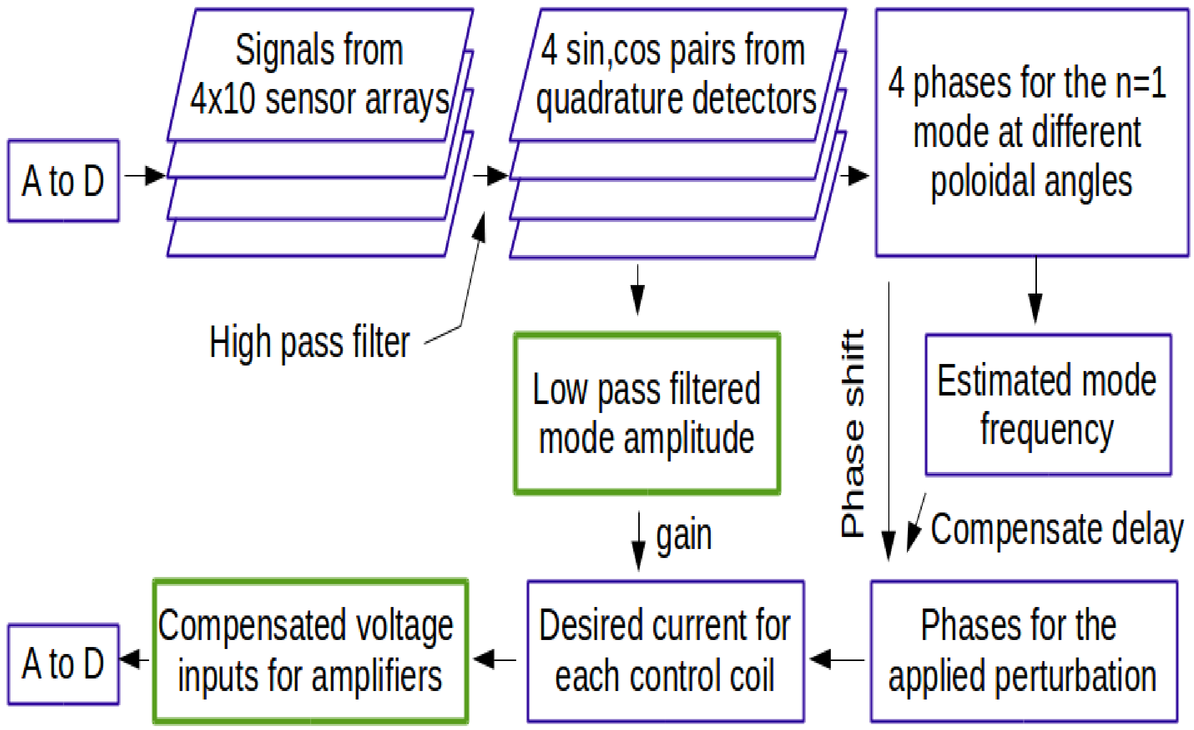

Figure 14. An illustration of the feedback algorithm. Major changes to the previous algorithm is highlighted in green.

arising instability is usually an $n = 1$ mode and the m number depends on the edge q of the plasma. If one uses a uniformly constructed θ as described in Sec. I B 2, the structure of the mode will be $A(\theta)\exp[i(f(\theta) + \varphi + \triangle\varphi)]$, with the periodicity constraint: $f(2\pi) - f(0) = 2m\pi$. But $f(\theta)$ will not be necessarily linear on θ. The $A(\theta)$ dependency addresses the observation that the mode amplitude is not uniform, usually stronger on the outboard side than on the inboard side. The global structure used to estimate the mode must be consistent with this observation. The expectation of the plasma response to a proportional gain on the measurement, predicted in Sec. III C 2, is used.

The GPU-based feedback system takes in multi-channel measurement signals through the Analog-to-Digital converter. Newly arrived signals update various physics parameters describing the plasma model in real time. The algorithm runs in parallel by the threads on the GPU to process the signals from multiple channels at the same time. The threads then calculate the output signals and send them to the actuator through the Digital-to-Analog converter.

Input signals from magnetic sensors are handled in four groups to produce the estimation of the mode amplitude and phase. The input signals come from the magnetic sensors measuring the change of magnetic flux through induced electric voltage. The signals are immediately integrated to reconstruct the total magnetic field measured along poloidal/radial direction. The location of these sensors, as is shown in Sec. II A, makes it natural to split them into four toroidal arrays. Each of the array can measure the mode along the toroidal direction individually. For each array, the $n = 1$ mode amplitude and phase is described by the mode component on the sine/cosine basis.

Take one array of feeback sensors in the middle plane for example, the ith sensor in the array is located at φ_i with measurement S_i. If the mode structure is estimated as $A_s sin\varphi + A_c cos\varphi$, then the error in estimation for each sensor will be $S_i - A_s sin\varphi_i - A_c cos\varphi_i$. The best estimation looks for A_s and A_c to minimizing the penalty function:

$$\sum_i \left(S_i - (A_s sin\varphi_i + A_c cos\varphi_i)\right)^2$$

The solution for the minimization is a simple matrix multiplication:

$$(A_s, A_c) = (S_1, \cdots, S_n) \cdot \begin{pmatrix} sin\varphi_1 & \cdots & sin\varphi_n \\ cos\varphi_1 & \cdots & cos\varphi_n \end{pmatrix}^{\dagger} \tag{24}$$

where $M^{\dagger}$ is the pseudo inverse of M. The pseudo inverse matrix does not depend on the measurement and is computed before the experiment begins. When the sensors are evenly distributed on the machine, this is the same as direct projecting the measurement on the basis function. In the case of malfunctioning sensors, they are excluded from measurement and the vectors in inverse matrix differ from the basis function. This method is better for the unevenly distributed sensors, than the direction projection method.

The mode amplitude and phase are obtained from these estimations. Ideally, once

A_s and A_c are obtained, we can express the estimated mode as

$$A_s sin\varphi_i + A_c cos\varphi_i = A sin(\varphi_i + \triangle\varphi) \tag{25}$$

where $A = \sqrt{A_s^2 + A_c^2}$ is the mode amplitude and $\triangle\varphi = \arctan(A_c/A_s)$ is the mode phase. In practice, due to sensors mis-alignment and asymmetric equilibrium evolution, the A_c and A_s directly obtained from the projection contain a slowly changing equilibrium signal that offsets the fluctuation signal. This is where the equilibrium estimation method discussed in Sec. IV C comes in to extract out the fluctuation part of A_c and A_s. An example of this is shown in Fig. 15. After obtaining the fluctuating component contributed by the rotating mode, the mode amplitude and phase are calculated with Eq. 25. Currently, only the mode measured by poloidal field sensors are used. The signals measured by radial sensors are not used, due to the low fluctuation amplitude measured in radial field.

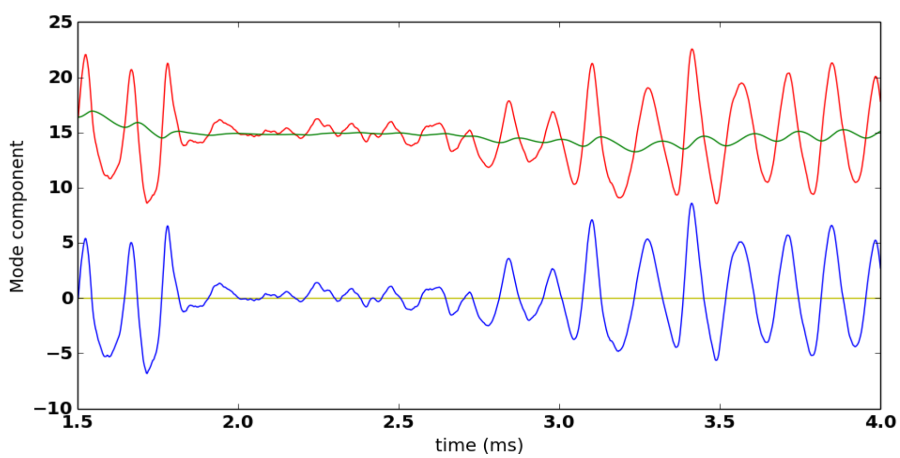

Figure 15. An example of extracting the fluctuation signal from the mixed mode component. The red line is the directly computed A_c, which is clearly offset from zero. Green line is the estimated equilibrium. Blue line is the estimated fluctuation signal and the yellow line is the constant zero level for comparison.

The four groups of mode amplitude and phase provide critical information about how the perturbation should be applied. The amplitude distribution among the four groups indicates the $A(\theta)$ function of the mode structure with respect to poloidal angle. And the phase shifts $\triangle\varphi$ between the four groups sketch the $f(\theta)$ function, the helical structure of the mode. Under proportional gain, the applied perturbation will take the same structure of the detected mode. The changing rate of the mode phase against time provides an estimation for the rotation frequency. The frequency estimation is implemented with the method described in Sec. IV C.

There is a delay of 22μs between the measured signal and the applied signal. At each time, when a perturbation with regard to the measurement is actually applied, the mode will have already rotated to a different angle with regard to the measurement. At a typical frequency around 7kHz, the shift will be around 50 degrees. It is compensated in the system by adding an extra phase shift to the applied perturbation, depending on the estimation of the rotation frequency. The current in the coil will be calculated with respect to the desired perturbation. The perturbation is applied by driving the control coil array with the compensated signal.

The phase shift between the measured mode and the applied perturbation is crucial for the feedback suppression. The algorithm tries to maintain the desired phase shift at its best capability. The smoothing effect discussed in Sec. IV D can cause the excitation of a slow mode when the gain is high. This phenomena is observed in [32] and hinders the feedback performance as a high gain is sometimes necessary. This smoothing effect is mitigated by adapting the compensation method discussed in Sec. IV D. From the actual experimental data, we notice that the sudden changes on the coil current request not only come from quick changes in the mode phase, but can also come from abrupt variations in the mode amplitude. Quick response to the mode amplitude variation may not be necessary. Compensation on this only adds more burden to the amplifiers. This observation is addressed by smoothing the mode amplitude signal before using it for feedback perturbation calculation. In this way, the capacity of the amplifiers will be distributed more on adapting the fast changes in the phase of the mode detected.

In summary, the signal processing steps illustrated in Fig. 14 is performed as following:

- Raw signals from sensors are characterized by $n = 1$ mode components with Eq. 24. The mode components are filtered by the highpass filter, the $(1 - L_{\alpha_1})^2$ operator, to extract the instability signal.

- The sine/cosine mode components give the measured mode amplitude and phase for the instability. The frequency of the mode rotation is estimated by applying $L_{\alpha_2}^2 \partial_t$ on the mode's phase signal.

- Proportional gain is applied on the measured mode to calculated the desired perturbation. Time delay of the system is compensated in mode phase. The mode amplitude is smoothed by lowpass filter, the L_{α_3} operator.

- The final output is transformed through Eq. 23, to compensate the delay caused by the amplifiers' rising time for signal.

Compared with previous design, the new algorithm uses a new cost-efficient method to extract fluctuation signals from magnetic sensors, adapts the current control method that provides quicker control coil response and achieves better phase accuracy in feedback control. These improvements resulted in stronger feedback results and feedback suppressions are successfully demonstrated under different wall conditions, and artificially slowed plasma. Details about the experiment are discussed in next section.

V. EXPERIMENTAL RESULTS OF THE FEEDBACK SYSTEM

This chapter describes the experimental results of this thesis. First, we present the result where feedback suppression is achieved on the ordinary wall condition, which is a direct improvement compared with results shown in [31, 32]. Second, the feedback result on different wall conditions are presented, where plasma is more unstable with reduced wall coupling. Finally, the feedback result on plasma slowed by bias probe is discussed.

A. Feedback suppression

The feedback system performance on HBT-EP has improved with the newly developed algorithm. The suppression effect is observed over a long duration and the issue with excitation of the slow mode is reduced. The three discharges shown in Fig. 16 have different feedback settings: one is a reference discharge, one is with feedback starting at 2.5ms and switched off at 6ms, the last one has feedback turned on at 2.5ms but switched off at 4.2ms. The mode's amplitude is reduced when the feedback suppression is active and rises after feedback is switched off.

The slow or acceleration effect of the feedback system is also evident in the experiment. With proper phase shift applied, the mode rotation frequency can be affected. This is consistent with previous observation. Shown in Fig. 17 are two examples where the mode is accelerated or slowed by the feedback perturbation. Different phase shift is applied in each case. This confirms that maintaining the correct phase shift between perturbation and measurement is crucial for the mode suppression. Inaccurate phase shift applied in a feedback suppression setting will result in modified mode rotation, and even excitation other slow modes, as is observed in the previous feedback system[32].

Fourier transformation on the mode signal gives another view of the mode suppression effect. For the mode signal, the time series of the sine/cosine pair is combined into a complex trace: $A_c + iA_s$, which is the input of the Fourier transformation.

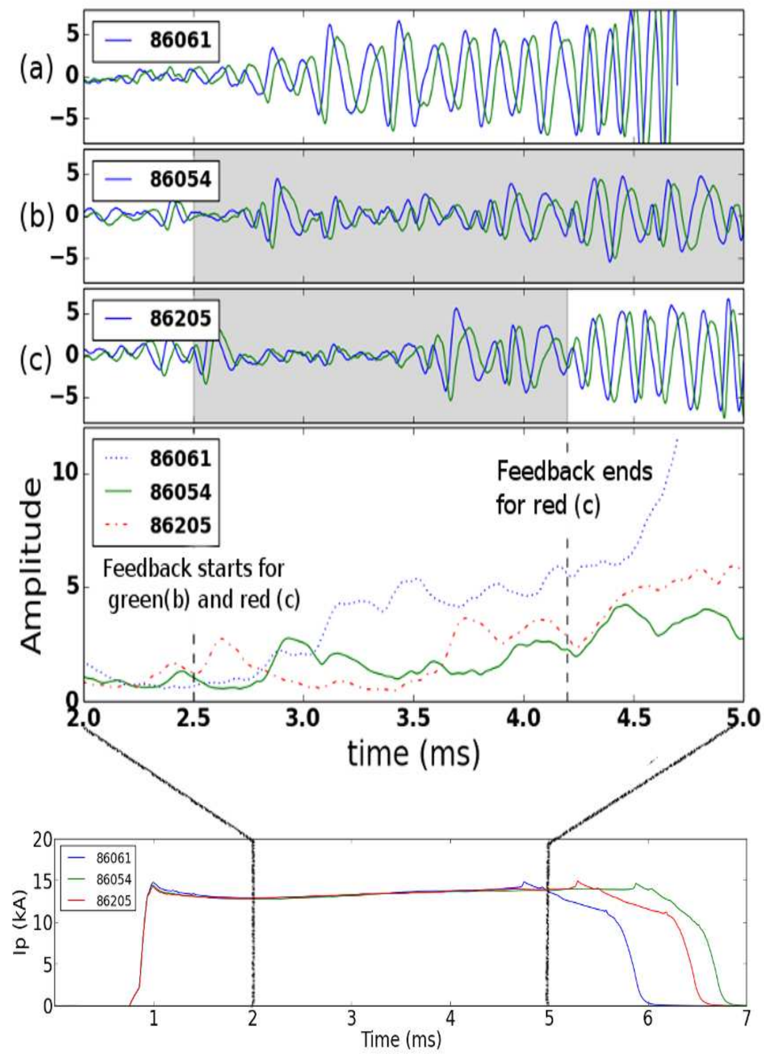

Figure 16. Three discharges:(a) without feedback, (b) with feedback active from 2.5ms to 6.0ms, and (c) with feedback active from 2.5ms to 4.2ms. The top 3 plots show the sine/cosine mode components for each discharge. The grayed area indicates when feedback is on. The 4th plot shows the smoothed mode amplitudes: 86061(blue)(a) is a reference discharge which disrupts at ∼4.8ms. 86205(red)(c) has the mode amplitude going back up after the feedback is turned off. The bottom plot shows the plasma current of the three discharges.

This views the mode rotation as a combination of signals at different frequencies. It illustrates how much energy is distributed at each frequency interval. The spectral analysis, shown in Fig. 18a, compared with Fig. 6 in Ref. [31], reproduced in Fig. 18b,

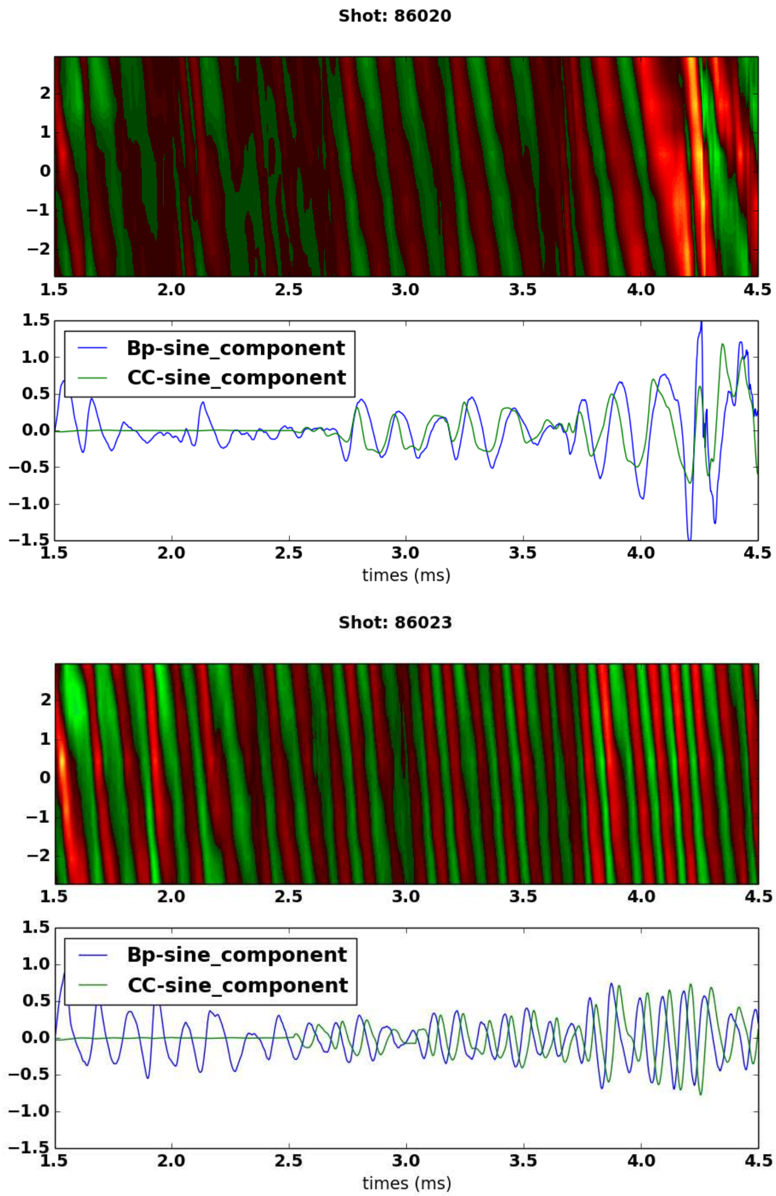

Figure 17. Example of the feedback system slowing down the mode rotation or accelerate the rotation. The first row is the contour plot of the mode measured on magnetic sensors. The second row shows the detected mode signal against the applied perturbation mode (CC stands for control coil). Different phase shift between the detected mode and perturbation is applied in the two cases. In both plots, the plasma rotation changes significantly after the control coil is turned on.

indicates a much stronger suppression effect at all frequencies, with no slowly rotating mode excited.

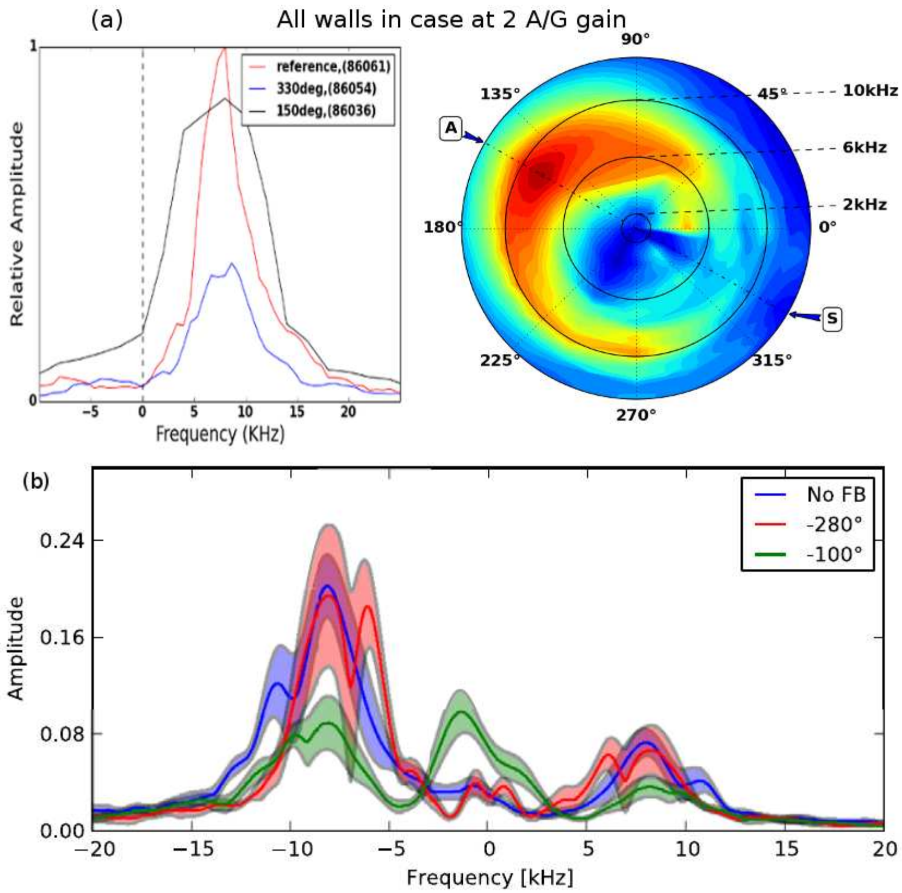

Figure 18. Phase scan plot for "all walls in" configurations. On the first row, the left plot compares the feedback suppressed/amplified discharges to the reference discharge. The right plot shows how the spectrum of the mode is affected with different phase shifts. The S and A symbols indicate the phase for suppression and amplification. The dependency on $\triangle\phi$ is consistent with the simulation shown in Fig. 9. The second row is a reproduce of Fig. 6 in Ref. [31]. The positive direction of frequency was opposite to the actual rotation direction. For other results shown in this paper, the positive direction of frequency is aligned with mode rotation.

To better understand the role of phase shift in the feedback system, a phase scan of the parameter is performed, with other parameters fixed. For each phase shift chosen, the plasma with feedback on is tested. The spectrum analysis on the mode rotation is carried out. All the data is aggregated into one single contour polar plot, with the color indicating the strength of the spectrum. The result is shown in the contour plot in Fig. 18a. When the phase shift is roughly 90 degrees ahead of suppression case, the mode is slowed, and the spectrum density is pushed toward the low frequency region. When the phase shift is roughly 90 degrees behind the suppression case, the mode is accelerated. When the phase shift is opposite to the suppression case, the mode is amplified.

B. Feedback with different wall configuration

The feedback system is also tested with different wall configurations. As is shown in Sec. II A, HBT-EP has a 2x10 set of in-vessel wall segments whose radial positions can be adjusted individually. The following wall configurations are considered in the experiment:

1. All of the shells are close to the plasma surface: the "all walls in" configuration.

2. The stainless walls are close and the ferritic walls far away from the plasma: the "stainless walls in" configuration.

3. The ferritic walls are close and the stainless walls far away from the plasma: the "ferritic walls in" configuration.

4. All of the walls are far away from the plasma, the "all walls out" configuration.

The positions of the shells, on which the ferritic materials are mounted, are used as the reference point for wall configuration. In the "all walls in" or "all walls out" configuration, all the shells are maintained at the same radial position. This means that the layer of the ferritic material, being 5.6mm thick, will stay closer to the plasma surface than the surface of the stainless steal segment. The choice is made in this way so that the eddy current on the wall, and the control coils, will be at the same level of radial position. When in the "stainless walls in" or "ferritic walls in" configuration, the radial positions of the sensors and coils will be staggered. This creates a $n = 5$ ripple effect on the detected signal and applied perturbation. Fortunately, with $q \sim 3$, the $n = 5$ mode resonates with plasma would have $m = 15$ which, with spatial decay rate of $(a/b)^{2m}$, would not have a strong response from plasma. So the analysis on this mode number is not examined. The detection in feedback system thus only works on the $n = 1$ signal component, and does not implement any algorithm to compensate this $n = 5$ ripple effect.

Wall configuration	Wall coupling c	Feedback gain(A/G)	Control current for suppression(A)
All walls in	0.1	2.0	12.2
Stainless walls in	0.07	4.0	13.3
Ferritic walls in	0.07*	5.0	23.3
All walls out	0.05	5.5	33.1

Table II. Experimental parameters for different wall configuration cases. The coupling coefficient, c, is calculated with VALEN[38] without including the ferritic material effect. (*)The c in the ferritic wall case should be smaller than that in the stainless wall case because of shielding from ferritic tiles. The control coil current for suppression is the averaged current amplitude driven on coils in the feedback suppression case.

The effective plasma wall coupling coefficient c is modified when adjusting the shell positions because of its dependence on the ratio of plasma radius, a, and conductive wall radius, b. For a uniform, cylindrical wall, $c \sim (a/b)^{2m}$. The c factor drops by $\sim 50\%$ when changing from the all walls in case to the all walls out case. Numeric evaluations using VALEN for the four wall cases on a $(3, 1)$ kink mode are shown in Tab. II. Plasma is more unstable at reduced wall coupling[6]. Increased feedback gain and stronger magnetic perturbation are required to achieve feedback suppression.

The new control algorithm achieves feedback suppression in all 4 cases. In each case, the performance of feedback is examined with a scan of the phase shift parameter $\triangle\phi$ while maintaining other conditions fixed. As predicted by simulation, mode acceleration, suppression, deceleration, and amplification are observed depending on $\triangle\phi$. For the all walls in case, the feedback suppression is achieved with a gain at 2A/Gauss, which drives the control coils with a current signal peaking around 12A. This coil current is consistent with the results shown in [32], without excitation of

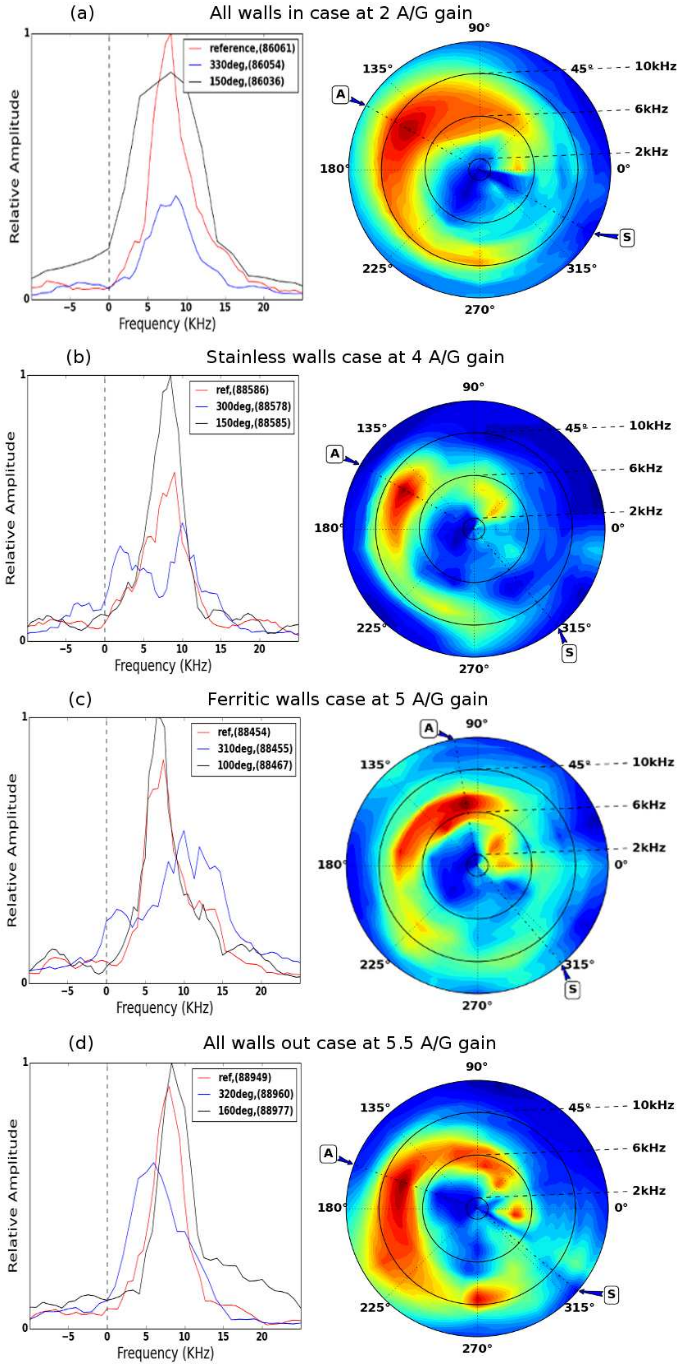

Figure 19. Phase scan plots for different wall configurations. As the wall coupling is weakened or ferritic material is introduced, the suppression becomes less effective and the gain needs to be increased.

the slowly rotating mode. Since the plasma becomes less coupled to the wall when the shells are retracted, the gain must be increased to achieve suppression with lower c. In each case, the gain is adjusted to the point where clear mode suppression is observed. Installation of the ferritic material in HBT-EP has made plasma more unstable, as is reported in [44]. Although the model in [34] predicts the growth rate to increase proportional to the relative permeability, μ_r (≈ 8 in our case), the observed growth rate increment ratio is around 1.5 to 2.0 [35]. This is in part due to the partial coverage of the ferritic material around the plasma, $\sim 15\%$ in our case. Mode suppression for the "ferritic walls in" case is achieved, with increased feedback gain. The performance on the spectrum analysis is not as clear as that for the "all walls in" case. The results are shown in Fig. 19.

C. Feedback with different plasma rotation

The feedback system is tested with slowed plasma under the "All walls in" configuration. In HBT-EP, the plasma rotation can be modified by an internal biased electrode (called "bias probe"), which drives a radial current across the plasma and induces angular momentum through $J \times B$ force[45]. A plasma with slowed rotation gives a smaller torque parameter $\bar{\alpha}$ [19]. The natural rotation frequency of a mode in HBT-EP is $7 \sim 8$kHz. This technique slows the mode rotation to 4kHz with the bias probe voltage set at 40V with respect to the chamber's ground, driving a radial current ~ 30A. An example of this discharge is shown in Fig. 20.

The bias probe is also managed by the feedback system. The GPU uses one thread to control the voltage on the bias probe in the same way as it drives other control coils. The output signal is updated in real time and has the capability of adjusting the bias probe's voltage with respect to the measured mode signal. Currently, the output voltage is preprogrammed for the discharge, without active feedback on the information from the measurement. This modifies the overall plasma rotation frequency to a predefined range.

As the rotation being slowed, the growth rate of the mode increases, and a feedback gain at 3 A/Gauss achieves an equivalent suppression. As predicted in Fig. 10, the

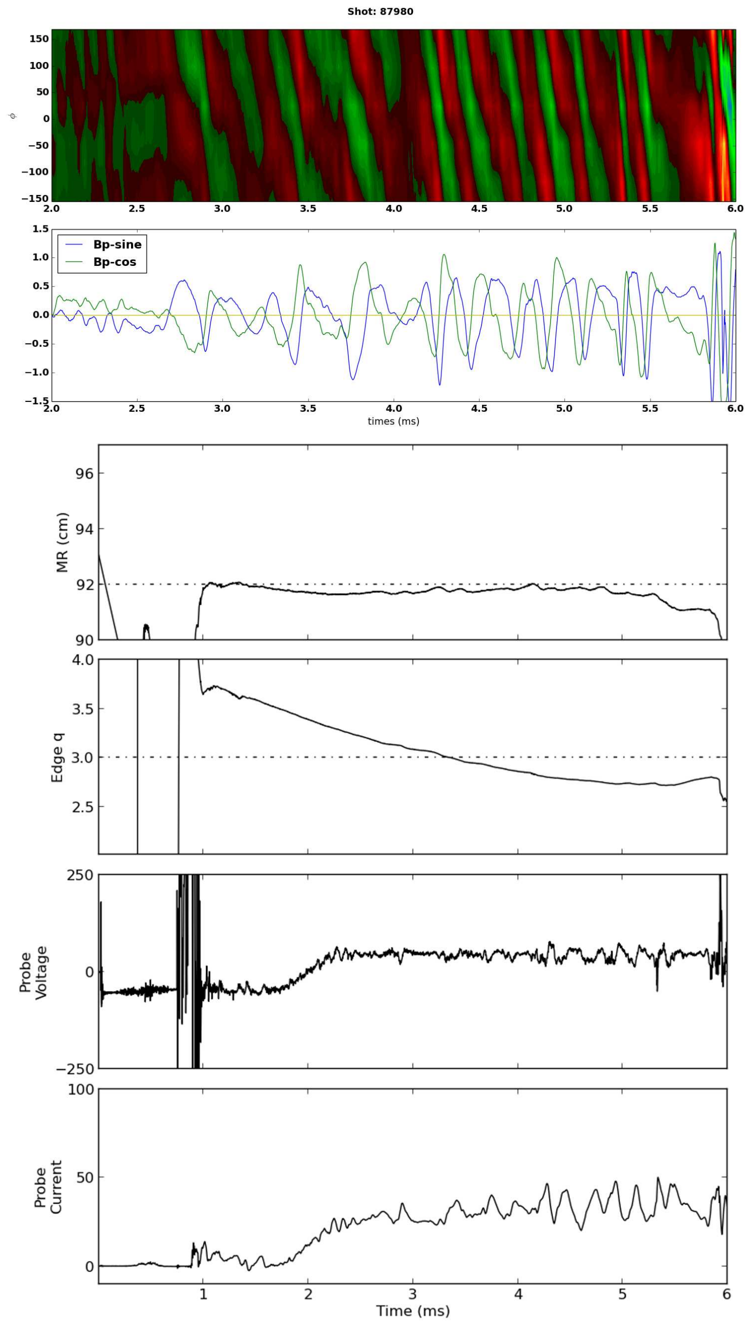

Figure 20. A typical shot where plasma is slowed by the bias probe. Bias probe is gradually turned on starting at 1.8ms and the voltage is maintained at 40V. Plasma rotation is visibly slowed, as is shown in the contour plot on the top.

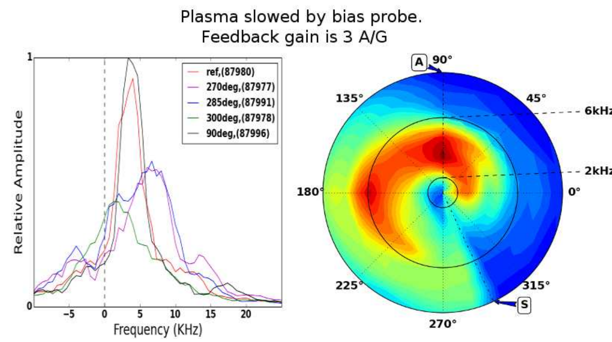

Figure 21. Feedback phase scan on plasma discharges slowed with the bias probe. The spectrum density is shifted toward lower frequency because the plasma is slowed by the bias probe. $\triangle\phi$ for suppression is around 290°.

drop in rotation reduces the $\bar{\alpha}$ parameter which also decreases the optimal phase shift for suppression. As is shown in Fig. 21, the optimal phase shift for suppression is around 290 degrees in slowed plasma while it is 330 degrees in the non-slowed case shown in Fig. 19.

In summary, suppression on fast kink mode is achieved without excitation of slow mode in the improved feedback system. Even with unfavourable wall configurations where the plasma is more unstable, feedback suppression is still achieved, at higher feedback gain. The system also works when the plasma rotation is slowed by the bias probe.

VI. SUMMARY AND CONCLUSIONS

Tokamak is the magnificent art of modern science which seeks energy through one of the most violent processes in nature, while sustainably keeping the whole device in order and under control. Control of instability is the main contribution of this thesis to the study of plasma, which is summarized in Sec. A. Suggestions of further research is discussed in Sec. B.

A. Summary of the results

The plasma investigated in HBT-EP has a dominant instability, that is a fast rotating kink mode, whose (m, n) number is closely related to the edge q, which, in most cases presented in this thesis, is exemplified by a strong $(m, n) = (3, 1)$ mode. As is shown in Sec. II, the mode's fast rotation ($\sim$ 7kHz), further complicated by the fast variation in amplitude and frequency, suggests the need of a time critical and accurate phase response from the feedback control system. A control from outside is only effective, when it acts at the speed of the instability from inside.

The improved feedback system presented in this thesis has demonstrated sustained and clear feedback suppression effect on the fast rotating unstable mode. In contrast to the previous method reported in Ref[46], the new system suppresses the mode at all frequency, without slow mode excitation as the side effect of high proportional gain.

The system is further examined under conditions where increased instability of plasma is induced by modified wall configurations. These additional configurations include 'ferritic walls in', 'stainless walls in' and 'all walls out' scenarios. Furthermore, plasma with slowed rotation is another scenario created to add in more instability. Notwithstanding all of these unfavorable conditions, mode suppression is achieved at all cases. This demonstrates the flexibility of the feedback system. Details of these results are shown in Sec. V, Fig. 19.

Observations in experiment confirm the theoretical model, which predicts mode suppression, acceleration, amplification and deceleration with specified phase shift. Moreover, decrease of coupling coefficient c, induced by the retraction of wall, requires higher proportional gain to achieve comparable suppression effect. Comparison of the 'ferritic walls in' and 'stainless walls in' is consistent with the prediction of increased gain. In the case of plasma slowed with bias probe, modification to the optimal phase shift for suppression is observed, as is seen in the theoretical model discussed in Sec. III.

The improved feedback system results from its better phase accuracy between the detected instability and the applied perturbation. Such perturbation, requested to be in resonance with the fast evolving instability, is difficult to deliver, when the system drives the control coils through amplifiers. The amplifier, as a transmitter and transformer, intrinsically delays and smooths the signal. To compensate for this lag, current control method is implemented to enhance the applied current. This method is modified from its original classical form, to adapt the situation that measurement on the coil current is not readily available in the system for closed loop calculation, to reduce the latency. Furthermore, to improve the accuracy in phase rather than amplitude, the detected mode amplitude is smoothed to mitigate its exacting impact on the system's capacity. Full explanation of this algorithm is shown in Sec. IV.

The windowed averaging method in previous design is substituted with the exponential weighted linear fitting method, implemented through digital band pass filters. This method maintains the quality of the regression on system states, while increasing the efficiency in memory storage and transfer. Such efficiency allows the program to finish calculations in the short time cycle critical for the feedback suppression.

Simultaneous operation on control coils and bias probe, in the slowed plasma scenario, opened another possibility for the the GPU-based feedback system. This experiment proves in principle that, through careful design, the feedback system can exert the power of magnetic coils and bias probe both, from inside and outside the plasma, for the purpose of instability suppression.

In all, this thesis shows the recent progress of HBT-EP made on the GPU-based feedback control system. The system takes 80 magnetic field sensors as input, 40 in-vessel coils and 1 bias probe as output, to apply perturbation on the plasma. This parallel computation system samples data every $6\mu s$, exhibiting a total latency around $22\mu s$ between the measured signal and the delivered output. The flexibility in the design environment has allowed us to test numerous implementations and will continue to assist us in the future research.

The feedback suppression on plasma instability is important for the ITER experiment and pragmatic fusion. Knowledge presented by this thesis contributes to the feedback system design on these devices, where fast and accurate response to plasma instability is critical.

B. Direction of future research

Success of the feedback control in HBT-EP with the current GPU-based system has opened promising areas for future research, including: integration of more hardware into the system, design and test of other algorithms and further investigation of the theoretical model for the plasma.

The physics model for plasma described in Sec. III C 2 is consistent with the experimental observations. The agreement is, however, qualitative. This is expected because the current linear single helicity model is yet to consider multi-mode effect, or the change of equilibrium, and thus dominant instability, against time. More comprehensive simulations, together with considerations about the 3D structure in HBT-EP in the future, is needed to provide better predictions about what gain will be used for feedback suppression. The system can then adaptively change the feedback scheme based on the equilibrium information collected at run time. This will improve the robustness of the system.

The feedback performance on instability suppression is the main topic of this thesis. Its capability, however, should not be limited to this. HBT-EP is susceptible to disruption when operating with $q \sim 2$. Preliminary tests have shown that the feedback system can delay the disruption to some extent by reducing the $(m, n) = (2, 1)$ mode activity[44]. This capability could be further explored to see the system's potential in mitigating disruption in general.

Having integrated the bias probe into its output, the system will then actively control the bias probe voltage to maintain a target plasma rotation. Specially carefulness is required in the estimation of plasma rotation frequency for the closed-loop calculation. Delays in the closed loop feedback could induce unwanted excitations, as has been seen in the previous design. Experimental observations so far suggest that the plasma rotation has more variation with the inserted bias probe. Applying a voltage on the probe will shift the average rotation frequency of plasma, and widen the frequency distribution at the same time. This must be taken into consideration when designing the feedback rotation control with the bias probe.

The feedback system could also be used for major radius control in the future. The system can take signals from rogowski coils, which provide estimations of the plasma major radius. The control coils can be programmed to create vertical fields at the edge of the plasma and apply a horizontal force on the plasma toroidal current, resulting in the movement of the major radius. At present, the major radius of a discharge in HBT-EP drifts over time. Maintaining a more steady major radius is desirable for post analysis, where the addition impact from plasma radius can be ruled out. Investigation on whether the feedback system can achieve certain level of major radius control is aligned with the interest of other studies in the group.

Current experimental observations suggest that the fast changes of mode amplitude and frequency, described in Sec. II, is associated with strong signals measured by the soft X-ray detector, which implies internal plasma activity. If the connection between plasma instability and its internal activity can be clearly established, such knowledge would enhance the feedback performance by guiding the system with real-time internal measurement.

[1] Wikipedia. Ivy Mike.

[2] Robert A. Gross. *Fusion energy.* Wiley Interscience publication, 1984.

[3] S. Atzeni and J. Meyer-ter Vehn. *The Physics of Inertial Fusion.* University of Oxford Press., 2004.

[4] LLNL Nuckolls, J. H. Early steps toward inertial fusion energy (IFE) (1952 to 1962). Technical report, 1998.

[5] J. Wesson. *Tokamaks.* Clarendon Press - Oxford, 1997.

[6] A. Bondeson and D. J. Ward. Stabilization of external modes in tokamaks by resistive walls and plasma rotation. *Physical Review Letters*, 72(17):2709–2712, 1994.

[7] E. J. Strait. Stability of high beta tokamak plasmas. *Physics of Plasmas*, 1(5):1415, 1994.

[8] T.C Hender, J.C Wesley, J Bialek, a Bondeson, a.H Boozer, R.J Buttery, a Garofalo, T.P Goodman, R.S Granetz, Y Gribov, O Gruber, M Gryaznevich, G Giruzzi, S Günter, N Hayashi, P Helander, C.C Hegna, D.F Howell, D.a Humphreys, G.T.a Huysmans, a.W Hyatt, a Isayama, S.C Jardin, Y Kawano, a Kellman, C Kessel, H.R Koslowski, R.J. La Haye, E Lazzaro, Y.Q Liu, V Lukash, J Manickam, S Medvedev, V Mertens, S.V Mirnov, Y Nakamura, G Navratil, M Okabayashi, T Ozeki, R Paccagnella, G Pautasso, F Porcelli, V.D Pustovitov, V Riccardo, M Sato, O Sauter, M.J Schaffer, M Shimada, P Sonato, E.J Strait, M Sugihara, M Takechi, a.D Turnbull, E Westerhof, D.G Whyte, R Yoshino, H Zohm, Disruption Group, the Itpa Mhd, and Magnet. Chapter 3: MHD stability, operational limits and disruptions. *Nuclear Fusion*, 47(6):S128–S202, June 2007.

[9] E. J. Strait. Magnetic control of magnetohydrodynamic instabilities in tokamaks. *Physics of Plasmas*, 22(2):021803, 2015.

[10] A. A. Vlasov. On Vibration Properties of Electron Gas. *J. Exp. Theor. Phys. (in Russian)*, 8(3):291, 1938.

[11] I. G. Abel, G. G. Plunk, E. Wang, M. Barnes, S. C. Cowley, W. Dorland, and A. A. Schekochihin. Multiscale Gyrokinetics for Rotating Tokamak Plasmas: Fluctuations, Transport and Energy Flows.

[12] K. C. Shaing and J.D. Callen. Neoclassical flows and transport in nonaxisymmetric toroidal plasmas. *Phys. Fluids*, 26(11):3315–3326, 1983.

[13] Y. Sun, Y. Liang, K.C. Shaing, H.R. Koslowski, C. Wiegmann, and T. Zhang. Modelling of the neoclassical toroidal plasma viscosity torque in tokamaks. *Nuclear Fusion*, 053015, 2011.

[14] H Alfven. Existence of electromagnetic-hydrodynamic waves. *Nature*, 150:405–406, 1942.

[15] Eric Priest and Terry Forbes. *Magnetic Reconnection: MHD Theory and Applications*. Cambridge University Press, 2000.

[16] G. P. ZANK and W. H. MATTHAEUS. The equations of reduced magnetohydrodynamics. *J. Plasma Physics*, 48:85–100, 1992.

[17] John M Finn. Resistive wall stabilization of kink and tearing modes. *Physics of Plasmas*, 2(January), 1995.

[18] M. S. Chu, J. M. Greene, T. H. Jensen, R. L. Miller, A. Bondeson, R. W. Johnson, and M. E. Mauel. Effect of toroidal plasma flow and flow shear on global magnetohydrodynamic MHD modes. *Physics of Plasmas*, 2(6):2236, 1995.

[19] Allen H. Boozer. Feedback equations for the wall modes of a rotating plasma. *Physics of Plasmas*, 6(8):3180, 1999.

[20] Yueqiang Liu, A Bondeson, M.S Chu, J.-Y Favez, Y Gribov, M Gryaznevich, T.C Hender, D.F Howell, R.J. La Haye, J.B Lister, P. De Vries, and EFDA Jet Contributors. Feedback and rotational stabilization of resistive wall modes in ITER. *Nuclear Fusion*, 45(9):1131–1139, 2005.

[21] A.M. Garofalo, M.S. Chu, E.D. Fredrickson, M. Gryaznevich, T.H. Jensen, L.C. Johnson, R.J. Lahaye, G.A. Navratil, M. Okabayashi, J.T. Scoville, E.J. Strait, A.D. Turnbull, and DIII-D Team. Resistive wall mode dynamics and active feedback control in

DIII-D. *Nuclear Fusion*, 41(9), 2001.

[22] P. Piovesan, J. M. Hanson, P. Martin, G. A. Navratil, F. Turco, J. Bialek, N. M. Ferraro, R. J. La Haye, M. J. Lanctot, M. Okabayashi, C. Paz-Soldan, E. J. Strait, A. D. Turnbull, P. Zanca, M. Baruzzo, T. Bolzonella, A. W. Hyatt, G. L. Jackson, L. Marrelli, L. Piron, and D. Shiraki. Tokamak Operation with Safety Factor q95<2 via Control of MHD stabilities. *Physical Review Letters*, 113(4):045003, July 2014.

[23] N. Rath, J. Bialek, P.J. Byrne, B. DeBono, J.P. Levesque, B. Li, M.E. Mauel, D.A. Maurer, G.A. Navratil, and D. Shiraki. High-speed, multi-input, multi-output control using GPU processing in the HBT-EP tokamak. *Fusion Engineering and Design*, 87(12):1895–1899, December 2012.

[24] J I Paley, F Felici, S Coda, T P Goodman, and the TCV Team. From profile to sawtooth control: developing feedback control using ECRH/ECCD systems on the TCV tokamak. *Plasma Physics and Controlled Fusion*, 51(12):124041, 2009.

[25] M Bessenrodt-Weberpals, H J de Blank, M Maraschek, P J McCarthy, M Sokoll, K Asmussen, and the ASDEX Upgrade Team. MHD activity as seen in soft x-ray radiation. *Plasma Physics and Controlled Fusion*, 38(9):1543, 1996.

[26] Y. In, J. S. Kim, D. H. Edgell, E. J. Strait, D. a. Humphreys, M. L. Walker, G. L. Jackson, M. S. Chu, R. Johnson, R. J. La Haye, M. Okabayashi, a. M. Garofalo, and H. Reimerdes. Model-based dynamic resistive wall mode identification and feedback control in the DIII-D tokamak. *Physics of Plasmas*, 13(6):062512, 2006.

[27] D.a Gates, J.R Ferron, M Bell, T Gibney, R Johnson, R.J Marsala, D Mastrovito, J.E Menard, D Mueller, B Penaflor, S.a Sabbagh, and T Stevenson. Plasma shape control on the National Spherical Torus Experiment (NSTX) using real-time equilibrium reconstruction. *Nuclear Fusion*, 46(1):17–23, 2006.

[28] S.a. Sabbagh, J.W. Berkery, R.E. Bell, J.M. Bialek, S.P. Gerhardt, J.E. Menard, R. Betti, D.a. Gates, B. Hu, O.N. Katsuro-Hopkins, B.P. LeBlanc, F.M. Levinton, J. Manickam, K. Tritz, and H. Yuh. Advances in global MHD mode stabilization research on NSTX. *Nuclear Fusion*, 50(2):025020, 2010.

[29] P. Piovesan, D. Bonfiglio, L. Marrelli, a. Soppelsa, M. Spolaore, and D. Terranova. Self-organized 3D equilibrium formation and its feedback control in RFX-mod. *Nuclear Fusion*, 54(6):064006, 2014.

[30] David A. Maurer, Daisuke Shiraki, Jeffrey P. Levesque, James Bialek, Sarah Angelini, Patrick Byrne, Bryan DeBono, Paul Hughes, Michael E. Mauel, Gerald A. Navratil, Qian Peng, Dov Rhodes, Nickolaus Rath, and Christopher Stoafer. High resolution detection and excitation of resonant magnetic perturbations in a wall-stabilized tokamak. *Physics of Plasmas*, 19(5):056123, 2012.

[31] N Rath, S Angelini, J Bialek, P J Byrne, B DeBono, P Hughes, J P Levesque, M E Mauel, G A Navratil, Q Peng, D Rhodes, and C Stoafer. Adaptive control of rotating magnetic perturbations in HBT-EP using GPU processing. *Plasma Physics and Controlled Fusion*, 55(8):084003, August 2013.

[32] N. Rath, P.J. Byrne, J.P. Levesque, S. Angelini, J. Bialek, B. DeBono, P. Hughes, M.E. Mauel, G.A. Navratil, Q. Peng, D. Rhodes, and C. Stoafer. Adaptive feedback control of rotating external kink modes in HBT-EP. *Nuclear Fusion*, 53(7):073052, July 2013.

[33] C. Cates, Mikhail Shilov, Michael E. Mauel, Gerald A. Navratil, D. Maurer, S. Mukherjee, D. Nadle, J.M. Bialek, and A.H. Boozer. Suppression of resistive wall instabilities with distributed, independently controlled, active feedback coils. *Physics of Plasmas*, 7(8):3133, 2000.

[34] V. D. Pustovitov and V. V. Yanovskiy. Ferromagnetic effects in the theory of slow and fast resistive wall modes in tokamaks. *Physics of Plasmas*, 21(2):022516, 2014.

[35] P. E. Hughes, J. P. Levesque, N. Rivera, M. E. Mauel, and G. a. Navratil. Design and installation of a ferromagnetic wall in tokamak geometry. *Review of Scientific Instruments*, 86(10):103504, 2015.

[36] J P Levesque, N Rath, D Shiraki, S Angelini, J Bialek, P J Byrne, B A DeBono, P E Hughes, M E Mauel, G A Navratil, Q Peng, D J Rhodes, and C C Stoafer. Multimode observations and 3D magnetic control of the boundary of a tokamak plasma. *Nuclear Fusion*, 53(7):073037, 2013.

[37] Allen H. Boozer. Simplified multimode calculations of resistive wall modes. *Physics of Plasmas*, 17, 2010.

[38] James Bialek, Allen H. Boozer, M. E. Mauel, and G. A. Navratil. Modeling of active control of external magnetohydrodynamic instabilities. *Physics of Plasmas*, 8(5):2170, 2001.

[39] M.E Mauel, J Bialek, A.H Boozer, C Cates, R James, O Katsuro-Hopkins, A Klein, Y Liu, D. A Maurer, D Maslovsky, G. A Navratil, T.S Pedersen, M Shilov, and N Stillits. Dynamics and control of resistive wall modes with magnetic feedback control coils: experiment and theory. *Nuclear Fusion*, 45(4):285–293, April 2005.

[40] Richard Fitzpatrick. A simple model of the resistive wall mode in tokamaks. *Physics of Plasmas*, 9(8):3459, 2002.

[41] Daisuke Shiraki, Sarah M. Angelini, Patrick J. Byrne, Bryan A. Debono, Paul E. Hughes, Jeffrey P. Levesque, Michael E. Mauel, David A. Maurer, Gerald A. Navratil, Qian Peng, Nikolaus Rath, Dov J. Rhodes, and Christopher C. Stoafer. Measurement of 3D plasma response to external magnetic perturbations in the presence of a rotating external kink. *Physics of Plasmas*, 20(2007), 2013.

[42] Alexander J. Klein, David A. Maurer, Thomas Sunn Pedersen, Michael E. Mauel, Gerald A. Navratil, Cory Cates, Mikhail Shilov, Yuhong Liu, Nikolai Stillits, and Jim Bialek. Suppression of rotating external kink instabilities using optimized mode control feedback. *Physics of Plasmas*, 12(4):1–4, 2005.

[43] Jeremy M. Hanson, Bryan De Bono, Jeffrey P. Levesque, Michael E. Mauel, David A. Maurer, Gerald A. Navratil, Thomas Sunn Pedersen, Daisuke Shiraki, and Royce W. James. A Kalman filter for feedback control of rotating external kink instabilities in the presence of noise. *Physics of Plasmas*, 16(5), 2009.

[44] J. P. Levesque, P. E. Hughes, J. Bialek, P. J. Byrne, M. E. Mauel, G. A. Navratil, Q. Peng, D. J. Rhodes, and C. C. Stoafer. Active and passive kink mode studies in a tokamak with a movable ferromagnetic wall. *Physics of Plasmas*, 22(5):056102, 2015.

[45] Christopher Stoafer. *Study of kink modes and error fields through rotation control with*

a biased electrode. PhD thesis, Columbia University, 2015.

[46] Nikolaus Rath. GPU-based, Microsecond Latency, Hecto-Channel MIMO Feedback Control of Magnetically Confined Plasmas. *Doctoral Thesis*, 2012.

I. APPENDIX: COORDINATE SYSTEMS FOR TORUS

Coordinate systems are needed to describe things quantitatively in space. Most people are familiar with the Cartesian coordinate (x, y, z) where the distance between two points is $ds = \sqrt{dx^2 + dy^2 + dz^2}$. The basis vectors $\vec{x}$, $\vec{y}$ and $\vec{z}$ are orthogonal and never changes their direction in the space. Differential operators under this coordinate system have straight forward expressions which are easy to carry out. It is used in many places. However, there are some occasions where it might be more convenient to use other coordinate systems. This is specially true when the objects of interest already have some basic shapes inherited in them. For example, using radial coordinate to describe orbital trajectories of earth around the sun might be preferred. Spherical coordinate coordinates could be a better choice when studying the flight paths around the earth. Differential operators become more complicated to carry out in certain situations, but more intuition of the problem is gained by describing it under the natural coordinate system.

For the study of tokamak, special coordinate systems are adapted to describe the torus, the shape in which the plasma is confined. If one picks a magnetic field line in plasma and follows it, the field line usually goes around the machine over and over, eventually sketching out a surface. In some cases, the field line will simply bite its own tail after finite loops. Sometimes it will actually fill up a volume rather than a surface inside the plasma. The surface sketched by the magnetic field lines is called the magnetic surface. It has the shape of a torus for the plasma in tokamak. Since plasma can, on the first order, move freely alone magnetic field lines, physics quantities like temperature, pressure, electric potential e.t.c. are usually approximated as identical, on the leading order, within a magnetic surface. This can be expressed as $\vec{B} \cdot \vec{\nabla} f = 0$ for f being these quantities of interest. These quantities are also called magnetic labels because they can be used to identify the magnetic surface. Quite naturally, the magnetic surface label is a good parameter to describe the spacial point in plasma. Each surface will then be parametrized by two additional scalars. Most coordinate systems used by plasma physicists are constructed in this way.

The numeric result of the differential operations should not depend on the coordinate system used. However, with respect to each component along the basis direction, the analytical expression becomes more complicated under certain natural coordinates. This is a trade off to gain more intuition about the physics in the problem. This section of the thesis focuses on showing tangible ways of obtaining expressions for frequently used differential operations such as gradient, divergence, curl and other similar ones. The analytic expressions, while complicated, can surely be carried out once everything is clearly defined. This facilitates using computer code to do numeric evaluation on the physics quantities of interest. One only needs to make sure that such expressions are derived correctly.

A. General coordinate systems

This section discusses the coordinate system with the least assumption. Only the metric, which describes distance between points, is needed as the starting point. Expressions for differential operators will be derived under the most generalized concept. They are thus suitable for more specific cases. This section covers the mostly used differential operators in analysis and gives detailed steps in obtaining them. For the ones that are not covered, they can be obtained following similar ways. Assuming only the existence of the metric and deriving the whole theory based on it, the theory is self-consistent. With the knowledge of this theory, one will be able to identify situations where assumptions under some flawed coordinate system are controversial to each other. This can happen when one tries to address the curvature, especially for the toroidal direction in plasma, with a quick work around. Sometimes those workarounds work fine locally, but become inconsistent once viewed under the global structure.

Three parameters are needed to uniquely identify a point in a 3D system. This can be expressed as $\vec{x} = \{x^1, x^2, x^3\}$ where $\vec{x}$ denotes the position of the point. x^i are the three parameters. In the Cartesian system, one has $\vec{x} = \{x, y, z\}$. The position of the point should not be dependent on how it is parametrized, and should be consistent across different coordinate systems. There must be a unique mapping between $(x, y, z) \rightleftarrows \{x^1, x^2, x^3\}$. This implies the existence of the relation $x = x(x^1, x^2, x^3)$, $y = y(x^1, x^2, x^3)$, $z = z(x^1, x^2, x^3)$. The mapping of $\{x^1, x^2, x^2\} \to \{x, y, z\}$ does not necessarily need to be linear, as long as it is one-to-one. Certain boundaries might exist to ensure the one-to-one property. For example, in a radial coordinate system, one often has $\theta \in [-\pi, \pi)$ to avoid multiple points mapping into the same position. Most importantly, the distance between two points should be consistent cross different coordinate systems:

$$
\begin{aligned}
ds^2 &= dx^2 + dy^2 + dz^2 \\
&= dx^2(x^1, x^2, x^3) + dy^2(x^1, x^2, x^3) + dz^2(x^1, x^2, x^3)
\end{aligned}
$$

As we will see in the later derivation, this is the fundamental assumption that generates the analytical expressions for other concepts.

Basis directions are defined in general coordinates. They serve as the similar functions as $\vec{e}_x$, $\vec{e}_y$ and $\vec{e}_z$ in Cartesian. The basis directions are defined by $\vec{e}_i = \partial\vec{x}/\partial x^i$, which shows how will the position change if only one of the parameters is increased. This definition is consistent with that in Cartesian. As is shown in Fig. 22, the vector basis shows the direction of how $\vec{x}$ will move, with infinitesimal change of x^i. The vectors are straight, at each point evaluated, while $\vec{x}$ can follow a curved path as x^i increases. If one considers the surface constructed by holding $x^1 = \mathsf{Const}$, while varying x^2 and x^3 freely, then at every point on this surface, $\vec{e}_2$ and $\vec{e}_3$ will be tangential to the surface. This is why they are also called tangential basis vectors. Different from that in Cartesian, the tangential basis vectors do not need to be of unit length. In fact, the length reflects the ratio of how quickly the point moves over the change of the parameter.

Inner production in general coordinate system is defined consistently with that in Cartesian. Let's first define the inner product between basis vectors. Consider

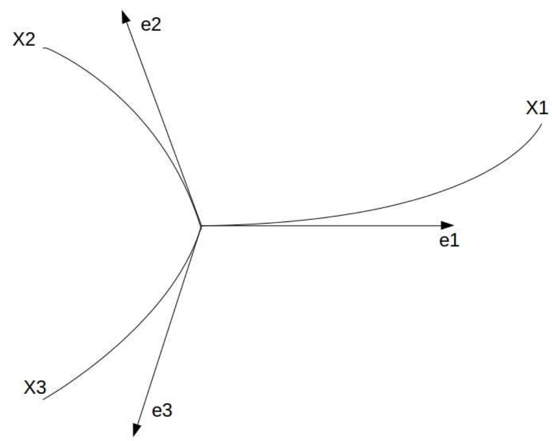

Figure 22. An illustration of the tangential basis vector.

$\vec{x}_0 = \{x_0^1, x_0^2, x_0^3\}$ then $\vec{e}_1 \triangle x^1 = \{x_0^1 + \triangle x^1, x_0^2, x_0^3\} - \vec{x}_0$. The inner product between basis vectors are defined as if they are measured under the Cartesian:

$$\vec{e}_1 \cdot \vec{e}_2 = \lim_{\triangle x^1, \triangle x^2 \to 0} \frac{(\{x_0^1 + \triangle x^1, x^2, x^3\} - \vec{x}_0) \cdot (\{x_0^1, x^2 + \triangle x^2, x^3\} - \vec{x}_0)}{\triangle x^1 \triangle x^2}$$

The expression is similar for any $\vec{e}_i \cdot \vec{e}_j$. The matrix $g_{ij} = \vec{e}_i \cdot \vec{e}_j$ is called the Jaccobian matrix and $J = \sqrt{Det(g_{ij})} = \sqrt{g}$ is called Jaccobi. Inner product between arbitrary vectors is a linear combination of g_{ij}. This will be shown below in this section.

There is another set of basis vectors that are equally important in the theory of general coordinate systems, called contravariant basis vectors. They are along the directions that are normal to the surfaces constructed with $x^i = \mathsf{Const}$. They are noted as $\vec{\nabla} x^i$, and the length of each one shows how fast does x^i changes when moving along this direction. It is also called the gradient of function $x^i(\vec{x})$. Moving along $\vec{e}_1$ by $\delta x^1 \vec{e}_1$ will change the value of x^1 by exactly δx^1, which implies $\vec{e}_1 \cdot \vec{\nabla} x^1 = 1$. Since moving along the direction $\vec{e}_2$ won't change x^1, one has $\vec{e}_2 \cdot \vec{\nabla} x^1 = 0$. More generally, $\vec{\nabla} x^i \cdot \vec{e}_j = \delta_{i,j}$. In the Cartesian, $\vec{\nabla} x^i = \vec{e}_i$, but in the general case, they can be pointing along different directions and the lengths can also be different.

The directions and lengths of these basis vectors usually depend on position. This is evident in the definition of $\vec{e}_i = \partial\vec{x}/\partial x^i$ and $\vec{\nabla}x^i$. It means that the basis vectors are always defined in the local context. Any vector analysis derived using the general coordinate system should be interpreted with this in mind. If one wants to express some non-local quantities, integrations over a line, a surface or a volume will often be involved. Inner product alone is not enough to describe the non-local distance, except for certain cases like Cartesian. For example, the distances between (r_1, θ_1) and (r_2, θ_2) usually cannot be simply expressed as a function of $\triangle r = r_1 - r_2$ and $\triangle\theta = \theta_2 - \theta_1$, unless the assumption $\triangle r, \triangle\theta \to 0$ is implied.

Any vector $\vec{A}$ can be decomposed by these basis vectors. If the tangential basis vectors are used, then it can be expressed as:

$$\vec{A} = A^1\vec{e}_1 + A^2\vec{e}_2 + A^3\vec{e}_3 = A^i\vec{e}_i$$

The decomposition is unique, because the coefficients are given by $A^i = \vec{A} \cdot \vec{\nabla}x^i$. Similarly, one can uniquely decompose the vector with contravariant basis vectors:

$$\vec{A} = A_1\vec{\nabla}x^1 + A_2\vec{\nabla}x^2 + A_3\vec{\nabla}x^3 = A_i\vec{\nabla}x^i \tag{26}$$

and the coefficients are obtained with $A_i = \vec{A} \cdot \vec{e}_i$. These coefficients give us a convenient way of expressing the inner product of two vectors:

$$\vec{A} \cdot \vec{B} = A_iB^i = A^iB_i = A^iB^jg_{i,j}$$

In the last formula, $g_{i,j}$ enters the expression when $\vec{A}$ and $\vec{B}$ are decomposed using the same vector basis $\vec{e}_i$. It addresses the issue that $\vec{e}_i$ is not orthogonal to each other, nor are they necessarily of unit length. From the above equation, one can also see that the components can be expressed in terms of each other:

$$A_i = A^jg_{i,j} \tag{27}$$

Volume is another important concept in general coordinate system. For three linearly independent infinitesimal directions $d\vec{A}$, $d\vec{B}$, $d\vec{C}$, they construct a infinitesimal volume element $dV = (d\vec{A} \times d\vec{B}) \cdot d\vec{C}$. By definition, the value of dV should be coordinate system independent. In Cartesian, the volume constructed by basis vectors $dx\vec{e}_x$, $dy\vec{e}_y$ and $dz\vec{e}_z$ are just $dxdydz$, because $(\vec{e}_x \times \vec{e}_y) \cdot \vec{e}_z = 1$. Any other vector can always be decomposed as a combination of the basis vectors and the volume constructed with such vectors can be expressed in a similar manner. This means, for a general coordinate system, one only needs to know the value of $V = (\vec{e}_1 \times \vec{e}_2) \cdot \vec{e}_3$. If the basis vector $\vec{e}_i$ can be expressed under Cartesian as $\{e_{ix}, e_{iy}, e_{iz}\}$, then V can be expressed as the determinant of the matrix

$$V = \begin{vmatrix} e_{1x} & e_{1y} & e_{1z} \\ e_{2x} & e_{2y} & e_{2z} \\ e_{3x} & e_{3y} & e_{3z} \end{vmatrix} = |M|$$

where M is used to denote the 3x3 matrix. V can be calculated with the following linear algebra trick. One has

$$\begin{aligned} V^2 = |M|^2 &= \left|M \cdot M^T\right| \\ &= \begin{vmatrix} \vec{e}_1 \cdot \vec{e}_1 & \vec{e}_1 \cdot \vec{e}_2 & \vec{e}_1 \cdot \vec{e}_3 \\ \vec{e}_2 \cdot \vec{e}_1 & \vec{e}_2 \cdot \vec{e}_2 & \vec{e}_2 \cdot \vec{e}_3 \\ \vec{e}_3 \cdot \vec{e}_1 & \vec{e}_3 \cdot \vec{e}_2 & \vec{e}_3 \cdot \vec{e}_3 \end{vmatrix} = g \end{aligned}$$

Thus the Jaccobi,

$$V = J = \sqrt{g} = (\vec{e}_1 \times \vec{e}_2) \cdot \vec{e}_3 \tag{28}$$

is the basic volume constructed by the basis vectors. Notice that the value of g is space dependent. It is an important variable that will be used many times in the later derivations.

The above expression also provides another important formula for the cross product between two basis vectors. $\vec{e}_1 \times \vec{e}_2$ should be perpendicular to both $\vec{e}_1$ and $\vec{e}_2$, so it must be along the direction of $\vec{\nabla}x^3$: $\vec{e}_1 \times \vec{e}_2 = c\vec{\nabla}x^3$. Since $\vec{\nabla}x^3 \cdot \vec{e}_3 = 1$, combined with Eq. 28, one see that $\vec{e}_1 \times \vec{e}_2 = J\vec{\nabla}x^3$. More generally, we have

$$\vec{e}_i \times \vec{e}_j = J\epsilon_{i,j,k}\vec{\nabla}x^k$$

where $\epsilon_{1,2,3} = 1$ and $\epsilon_{i,j,k} = \epsilon_{j,k,i} = -\epsilon_{j,i,k}$. So its value can only be 1, -1, or 0.

The linear Independence of the basis vectors ensures that $g \neq 0$. This means the matrix g_{ij} is non-singular and thus can be inverted. The inverted matrix is called $g^{ij} = (g_{ij})^{-1}$. From Eq. 27, one obtains that $A^i = A_j g^{ij}$. Because $A^i = \vec{A} \cdot \vec{\nabla}x^i = (A_j\vec{\nabla}x^j) \cdot \vec{\nabla}x^i = A_j\vec{\nabla}x^j \cdot \vec{\nabla}x^i$, this implies that each entry of the matrix satisfies:

$$g^{ij} = \vec{\nabla}x^i \cdot \vec{\nabla}x^j$$

Using similar derivations above, one can check that

$$(\vec{\nabla}x^1 \times \vec{\nabla}x^2) \cdot \vec{\nabla}x^3 = \sqrt{g^{i,j}} = 1/J$$
$$\vec{\nabla}x^i \times \vec{\nabla}x^j = \epsilon_{i,j,k}\vec{e}_k/J$$

The gradient operator on a scalar function can be expressed under the framework of the general coordinate system. Consider the gradient function $\vec{\nabla}f$, which defines how much will the scalar function change in space. Specifically, if the point moves infinitesimally by $\delta x^1\vec{e}_1$, the value of f should change by $\delta x^1\vec{e}_1 \cdot \vec{\nabla}f$. On the other hand, since the point moves from $\{x^1, x^2, x^3\}$ to $\{x^1 + \delta x^1, x^2, x^3\}$, the function $f(x^1, x^2, x^3)$ should change by $\frac{\partial f}{\partial x^1}\delta x^1$. Comparing these two, one has

$$\frac{\partial f}{\partial x^i} = \vec{e}_i \cdot \vec{\nabla}f$$

Comparing this with Eq. 26, and noticing that the decomposition is unique, we obtain the decomposition of $\vec{\nabla}f$ under the contravariant basis vectors:

$$\vec{\nabla} f = \frac{\partial f}{\partial x^i} \vec{\nabla} x^i$$

The divergence of a vector $\vec{A}$ reflects the net flux generated in a volume. The same method that being used to derive divergence formula under Cartesian can also be applied under the general coordinate system. At point $\vec{x} = \{x^1, x^2, x^3\}$, consider a box constructed by $dx^1\vec{e}_1$, $dx^2\vec{e}_2$ and $dx^3\vec{e}_3$. The volume of the box is $Jdx^1dx^2dx^3$. Consider two surfaces, one constructed by $dx^1\vec{e}_1$ and $dx^2\vec{e}_2$ at $\vec{x}$ and the other at $\vec{x} + dx^3\vec{e}_3$. The flux of $\vec{A}$ through the surface $d\vec{S}$ is $\vec{A} \cdot d\vec{S}$, where the surface element is defined by the two edges constructing the surface: $d\vec{S} = dx^1\vec{e}_1 \times dx^2\vec{e}_2$. The net contribution of the flux through these two surfaces will be

$$dx^3 \frac{\partial [\vec{A} \cdot (dx^1 dx^2 \vec{e}_1 \times \vec{e}_2)}{\partial x^3} = dx^1 dx^2 dx^3 \frac{\partial (JA^3)}{\partial x^3}$$

Adding all the net flux through the six surfaces of the box, the total would be $dx^1dx^2dx^3\partial(JA^i)/\partial x^i$. This is generated within a volume of $Jdx^1dx^2dx^3$, implying that the divergence of the vector field $\vec{A}$ at this point must be:

$$\vec{\nabla} \cdot \vec{A} = \frac{\partial J A^i}{J \partial x^i}$$

The curl of a vector field $\vec{A}$ can be easily expressed by using $\vec{A} = A_i \vec{\nabla} x^i$ and by decomposing the gradient function $\vec{\nabla} A_i$ with contravariant basis function:

$$\begin{aligned}
\vec{\nabla} \times \vec{A} &= \vec{\nabla} \times (A_i \vec{\nabla} x^i) \\
&= \vec{\nabla} A_i \times \vec{\nabla} x^i \\
&= \frac{\partial A_i}{\partial x^j} \vec{\nabla} x^j \times \vec{\nabla} x^i \\
&= \epsilon^{ijk} \frac{\partial A_i}{J \partial x^j} \vec{e}_k
\end{aligned}$$

where we have used $\vec{\nabla} x^i \times \vec{\nabla} x^j = \epsilon^{ijk} \vec{e}_k / J$ in the last step. This formula expresses $\vec{\nabla} \times \vec{A}$ with the tangential basis vectors.

Laplacian is another important differential operator often encountered in physics. Laplacian of a scalar function is the divergence of the gradient of this function. Since we already know the formula for both of this operators, it is easy to combine them and obtain:

$$
\begin{aligned}
\nabla^2 f &= \vec{\nabla}\cdot(\vec{\nabla} f) \\
&= \frac{\partial J(\frac{\partial f}{\partial x^i}\vec{\nabla} x^i)^j}{J\partial x^j} \\
&= \frac{\partial}{J\partial x^j}(J\frac{\partial f}{\partial x^i}\vec{\nabla} x^i \cdot \vec{\nabla} x^j) \\
&= \frac{\partial}{J\partial x^j}(J g^{ij}\frac{\partial f}{\partial x^i})
\end{aligned}
$$

where we have used $A^i = \vec{A}\cdot\vec{\nabla} x^i$ and $g^{ij} = \vec{\nabla} x^i \cdot \vec{\nabla} x^j$ in the derivation.

For evaluation purpose, values like g_{ij}, J will be computed once the coordinate system is constructed. The computation can be done analytically if the coordinate system has some nicely defined shape like circle or sphere. It can also be done just numerically if analytic expression is not practical. The point is, a theorist can use the differential operators freely in the derivation without worrying about the evaluation of them. The notation of $\vec{\nabla}$ operator should be kept as long as possible before the final evaluation process. In the final evaluation, if the coordinate system is wisely chosen, the system will often be symmetric with respect to certain parameters and one may find that $\partial f/\partial x^1 \equiv 0$ holds everywhere. Such features will usually simplify the evaluation process and compensate for the complicity involved in the matrix: $g_{i,j}$.

The basis vectors can be space dependent, varying their directions and lengths as they move in space. This subtlety can produce extra terms in the expression when differential operators are applied on the basis vectors. Christoffel symbol Γ^k_{ij} is used to address such variations of the basis vectors with space. For a basis vector $\vec{e}_j$, its variation rate along parameter x^i is also an vector and thus can be expressed as a linear combination of the tangential basis vectors. The coefficients of the decomposition are noted as the Christoffel symbol:

$$\frac{\partial}{\partial x^i}\vec{e}_j = \lim_{\delta x^i \to 0} \frac{\vec{e}_j(\vec{x} + \delta x^i \vec{e}_i) - \vec{e}_j(\vec{x})}{\delta x^i} = \Gamma^k_{ij}\vec{e}_k$$

It has 27 entries as i, j and k runs over 1,2,3. The Christoffel symbol can be evaluated based on g_{ij} and g^{ij}:

$$\Gamma^k_{ij} = \frac{1}{2} g^{kl} \left[\frac{\partial g_{il}}{\partial x^j} + \frac{\partial g_{jl}}{\partial x^k} - \frac{\partial g_{ij}}{\partial x^l} \right] \tag{29}$$

Detailed derivation for this formula is omitted here. There are some interesting identities that are useful regarding to the Christoffel symbol:

$$\begin{aligned} \frac{\partial g_{ij}}{\partial x^k} &= g_{jl}\Gamma^l_{ik} + g_{il}\Gamma^l_{jk} \\ \frac{\partial \sqrt{g}}{\partial x^i} &= \Gamma^j_{ij}\sqrt{g} \end{aligned}$$

It becomes compelling to use Christoffel symbol when tensors are mixed with differential operators. Here we show some examples of its application. One should be encouraged to use them if the analytical derivations can be made more clear and precise.

The first example is about the tensor $\vec{\nabla}\vec{A}$, where the differential operator is applied on vector $\vec{A}$ not in the sense of divergence nor curl. Since it is a tensor, we want to know how can each entries be expressed in terms of A_i or A^j if the tensor is cast into a matrix form. The meaning of the tensor$\vec{\nabla}\vec{A}$ becomes more clear by dot-producting it with vector $\vec{u}$ on the left. This gives the change rate of $\vec{A}$ along the direction of $\vec{u}$:

$$\begin{aligned} \vec{u} \cdot \vec{\nabla}\vec{A} &= u^i \vec{e}_i \cdot \vec{\nabla}\vec{A} \\ &= u^i \frac{\partial_i (A^j \vec{e}_j)}{\partial x^i} \\ &= u^i \left(\frac{\partial A^j}{\partial x^i} + A^k \Gamma^j_{ik}\right)\vec{e}_j \end{aligned}$$

where the Christoffel symbol is used in the last step for differentiation on $\vec{e}_j$. For a tensor $\overleftrightarrow{T} = T^{ij}\vec{e}_i\vec{e}_j = T_i^{\,j}\vec{\nabla}x^i\vec{e}_j$, we have $\vec{u}\cdot\overleftrightarrow{T} = u^k T_i^{\,j}\vec{e}_k\cdot\vec{\nabla}x^i\vec{e}_j = u^i T_i^{\,j}$. Comparing the expressions, one has the decomposition of $\vec{\nabla}\vec{A}$ under basis vectors:

$$\vec{\nabla}\vec{A} = (\frac{\partial A^j}{\partial x^i} + A^k\Gamma^j_{ik})\vec{\nabla}x^i\vec{e}_j = (\frac{\partial A^j}{\partial x^s} + \Gamma^j_{sk}A^k)g^{si}\vec{e}_i\vec{e}_j$$

The second example is about the divergence of a tensor: $\vec{\nabla}\cdot\overleftrightarrow{T}$. Here the flux considered is not a scalar but a vector: $d\vec{S}\cdot\overleftrightarrow{T}$. By the same method used to derive divergence of a vector field, we can construct a box Ω with $(\delta x^1\vec{e}_1\times\delta x^2\vec{e}_2)\cdot\delta x^3\vec{e}_3$ and have

$$\iiint_\Omega \vec{\nabla}\cdot\overleftrightarrow{T}dV = \oiint_{\partial\Omega} d\vec{S}\cdot\overleftrightarrow{T}$$

The net flux at x^1 and $x^1+\delta x^1$ will be

$$\delta x^1\frac{\partial}{\partial x^1}[(\delta x^2\vec{e}_2\times\delta x^3\vec{e}_3)\cdot\overleftrightarrow{T}] = \frac{\partial}{\partial x^1}(\sqrt{g}T^{1i}\vec{e}_i)\delta x^1\delta x^2\delta x^3$$

Sum the flux from all surfaces, one has $\vec{\nabla}\cdot\overleftrightarrow{T}$ expressed in terms of the basis vectors:

$$\begin{aligned}\vec{\nabla}\cdot\overleftrightarrow{T}\sqrt{g}\delta x^1\delta x^2\delta x^3 &= \iiint_S \vec{\nabla}\cdot\overleftrightarrow{T}dV = \frac{\partial}{\partial x^j}(\sqrt{g}T^{ji}\vec{e}_i)\delta x^1\delta x^2\delta x^3\\ \rightarrow \qquad \vec{\nabla}\cdot\overleftrightarrow{T} &= \frac{1}{\sqrt{g}}\partial_i(\sqrt{g}T^{ij}\vec{e}_j)\\ &= (\frac{1}{\sqrt{g}}\frac{\partial\sqrt{g}T^{ij}}{\partial x^i} + T^{il}\Gamma^j_{il})\vec{e}_j\end{aligned}$$

The expression for the Laplacian on a vector field is just a combination of the above two:

$$
\begin{aligned}
\nabla^2 \vec{A} &= \vec{\nabla} \cdot (\vec{\nabla} \vec{A}) \\
&= \vec{\nabla} \cdot ((\frac{\partial A^j}{\partial x^s} + \Gamma^j_{sk} A^k) g^{si} \vec{e}_i \vec{e}_j) \\
&= \frac{1}{\sqrt{g}} \frac{\partial}{\partial x^i} [\sqrt{g} (\partial_s A^j + \Gamma^j_{sk} A^k) g^{is}] \vec{e}_j \\
&\quad + (\partial_s A^m + \Gamma^m_{sk} A^k) g^{si} \Gamma^j_{im} \vec{e}_j
\end{aligned}
$$

which is a rather complicated form.

B. Coordinate systems used for plasma

Many types of coordinate systems are used in plasma physics, either to facilitate analytic derivation or to serve as the foundation of numerical computation. For most cases, the coordinate system is natural to plasma by assuming that one of the parameters represents the equilibrium magnetic surface label. Here are a few examples.

1. Cylindrical coordinate system

The cylindrical coordinate system is probably the most widely used one, especially for quick estimation. The plasma is modelled by bending the torus straight again. In this way, the torus becomes a cylinder and the magnetic surfaces are described by $r = \mathsf{Const}$ surfaces. Curvature in the toroidicity is neglected. The consistency in the toroidal direction is enforced by assuming a periodicity of $L = 2\pi R$ along the z direction, where R is the major radius of the torus. The helical structure of the plasma is captured in this model. Many theories, such as the reduced MHD shown in Sec. III A 1, are based on this model. The analytical derivation is simpler than its full 3D counterpart but the results obtained still provide plenty intuition about the nature of the problem.

The cylindrical coordinate system uses three parameters (r, θ, z) to identify a point in space. It's mapping with Cartesian is:

$$\begin{cases} x = r\cos\theta \\ y = r\sin\theta \\ z = z \end{cases}$$

The magnetic field lines are confined on the $r = \mathsf{Const}$ surfaces and thus the magnetic field can be expressed as $\vec{B} \propto q\vec{e}_z + \vec{e}_\theta$. q is called the safety factor, which indicates the helicity of the magnetic field. It is often assumed to be constant on each magnetic surfaces: $q = q(r)$. To make the periodicity constrain more clear, the z parameter is often substituted with $z = R_0\phi$ where ϕ is called the toroidicity angle. This reminds people that any function defined on the domain must satisfy $f(\phi) = f(\phi + 2\pi)$.

This is an orthogonal coordinate system with $g_{rr} = 1$, $g_{zz} = 1$ and $g_{\theta\theta} = r^2$. Using the formulas described in above section, one check the expressions of divergence, curl and Laplacian. The results are skipped here.

2. Simple coordinate system representing torus

To include the curvature from toroidicity, a coordinate system fitting the shape of a torus needs to be constructed. One can use (r, θ, ϕ) and parametrize the space as the following:

$$\begin{cases} x = (R_0 + r\cos\theta)\cos\phi \\ y = (R_0 + r\cos\theta)\sin\phi \\ z = r\sin\theta \end{cases}$$

where the fixed constant R_0 is called the major radius. The r is called minor radius and the family of $r = \text{Const}$ surfaces takes the shape of a torus. They represent the layers of magnetic surfaces inside the plasma.

This is an orthogonal coordinate system with

$$
\begin{aligned}
e_r &= \{cos\theta cos\phi, cos\theta sin\phi, sin\theta\}^T \\
e_\theta &= \{-rsin\theta cos\phi, -rsin\theta sin\phi, rcos\theta\}^T \\
e_\phi &= \{-(R_0 + rcos\theta)sin\phi, (R_0 + rcos\theta)cos\phi, 0\}^T \\
g_{ij} &= \mathsf{Diag}\{1, r^2, (R_0 + rcos\theta)^2\} \\
\sqrt{g} &= r(R_0 + rcos\theta)
\end{aligned}
$$

From this, one can obtain the expression for the divergence operator:

$$
\begin{aligned}
\vec{\nabla} \cdot \vec{A} &= \frac{\partial}{\sqrt{g}\partial r}(\sqrt{g}A^r) + \frac{\partial}{\sqrt{g}\partial\theta}(\sqrt{g}A^\theta) + \frac{\partial}{\sqrt{g}\partial\phi}(\sqrt{g}A^\phi) \\
&= \frac{\partial A^r}{\partial r} + \frac{R_0 + 2rcos\theta}{r(R_0 + rcos\theta)}A^r + \frac{\partial A^\theta}{\partial\theta} \\
&- \frac{r^2 sin\theta}{r(R_0 + rcos\theta)}A^\theta + \frac{\partial A^\phi}{\partial\phi}
\end{aligned}
$$

Note that $A^\theta = \vec{A} \cdot \vec{\nabla}\theta$ and $\vec{\nabla}\theta$ is of length r. This is different from some expression where the θ component for $\vec{A}$ is calculated by inner production of $\vec{A}$ with a unit vector along the θ direction. The same is true for the notation of A^ϕ. The Laplacian of scalar f is expressed as:

$$
\begin{aligned}
\nabla^2 f &= \frac{\partial}{\sqrt{g}\partial r}\left(\sqrt{g}\frac{\partial f}{\partial r}\right) + \frac{\partial}{\sqrt{g}\partial\theta}\left(r^2\sqrt{g}\frac{\partial f}{\partial\theta}\right) + \frac{\partial}{\sqrt{g}\partial\phi}\left((R_0 + rcos\theta)^2\sqrt{g}\frac{\partial f}{\partial\phi}\right) \\
&= \frac{\partial^2 f}{\partial r^2} + \frac{R_0 + 2rcos\theta}{r(R_0 + rcos\theta)}\frac{\partial f}{\partial r} + r^2\frac{\partial^2 f}{\partial\theta^2} \\
&- \frac{r^3 sin\theta}{R_0 + rcos\theta}\frac{\partial f}{\partial\theta} + (R_0 + rcos\theta)^2\frac{\partial^2 f}{\partial\phi^2}
\end{aligned}
$$

The expressions have become considerably more complicated than that in the cylindrical case. This is needed to include the curvature effect related with the toroidicity. Some theory first approaches the problem using cylindrical model, then expands the problem into this system to include possible toroidicity effect. Nevertheless, the above expression can easily be programmed for numerical computation.

The flux coordinate system tries to fully describe the shape of the magnetic surface and usually does not have nice analytical expressions shown above. The above examples first construct the coordinate system and then assume the magnetic surfaces in the plasma will fit with the $r = \mathsf{Const}$ surfaces. In reality, the equilibrium magnetic field often have some asymmetric 3D structures that do not easily fit with a pre-defined nice coordinate system. Another approach would be, starting from the existing magnetic field and then build a general coordinate system on top of it. This approach assumes the existence of magnetic surfaces across the plasma region of interest.

The flux coordinate system uses (ψ, θ, φ) to parametrize the space. The parameter ψ is used to label the plasma surfaces. Points with the same ψ resides on the same magnetic surface and vice versa. On each surface, $(\theta, \varphi) \in [0, 2\pi) \times [0, 2\pi)$ are used to parametrize the surface. Usually θ is used to denote the poloidal angle. Fixing other parameters, increase θ by 2π and the point will finish a whole circle around the torus poloidally. φ is used for the toroidal angle with similar meaning. There are plenty freedom here for the choices of the two parameters.

The helicity of the magnetic field is defined by the safety factor q. The magnetic surfaces can be considered as layers of tubes in the plasma. Let $\psi = 0$ denote the center axis of these layers and ψ increases as the point moves to outer layers. The magnetic field lines do not flow across the tube. Consider one tube at $\psi = a$, the total magnetic flux though the tube along the toroidal direction is called the Ψ_T.

$$\Psi_T(\psi = a) = \iint_{\psi \leq a} \vec{B} \cdot d\vec{S}$$

Between the two layers, the flux also flows poloidally and the field lines do not cross the boundary on either side. This makes another conserved quantity between the two layers. One can define the poloidal flux $\Psi_P(\psi)$, which does not depend on θ, as:

$$\Psi_P(\psi = a) = \iint_{\psi\in[0,a],\varphi\in[0,2\pi)} \vec{B} \cdot d\vec{S}$$

Both Ψ_T and Ψ_P only depend on the magnetic surface label ψ. The safety factor is defined, independent of (θ, φ), as

$$q(\psi) = \frac{d\Psi_T}{d\Psi_P}$$

If one considers a thin layer between two magnetic surfaces ψ and $\psi + \delta\psi$. Let $\delta\Psi_T$ be the toroidal flux in this layer and $\delta\Psi_P$ be the poloidal flux in this layer. According to the definition, q will be the ratio of this two. Picking one magnetic field line going along the surface, one can see that, after a large number of circles, q will be the ratio of the number of turns in the toroidal direction over that in the poloidal direction.

The concept of q helps in the choice of (θ, φ). If one first set φ as the natural toroidal angle like ϕ in the previous example, then θ can be specified to satisfy the equation:

$$\vec{B} = C[\vec{e}_\theta + q(\psi)\vec{e}_\varphi]$$

This condition makes $\vec{B}$ always straight under the (θ, φ) coordinates, with a slope of $1/q$. One can check that this condition is consistent with the notation that q represents the ratio of toroidal turns over the poloidal turns from any sufficiently long field line.

Coordinates satisfying this condition are called straight field line coordinate system. The choice is not unique. In fact, for any function $K(\psi, \theta, \varphi)$ defined on any straight field line coordinate system (ψ, θ, φ), the following transformation:

$$\begin{cases} \theta' = \theta + K(\psi, \theta, \varphi)/q \\ \varphi' = \varphi + K(\psi, \theta, \varphi) \end{cases}$$

will maintain the straight field line criteria. Therefore another parametrization $(\psi, \theta', \varphi')$ is obtained. The Hamada coordinate system chooses a special K such that $J \equiv 1$ is maintained every where. This certainly simplifies some of the analytical derivations.

For the flux coordinate system discussed here, the parameters are chosen based on the actual structure of the magnetic field. The basis tangential vectors are rarely orthogonal to each other. g_{ij} must be evaluated for the cross terms between different directions. The advantage is that ψ is always the magnetic surface label. On the first order, we will have many quantities that only depend on ψ, such as the temperature $T_e(\psi)$, the density $n(\psi)$ and the static electric potential $V(\psi)$. There will also be some symmetries related to the path along $\psi - q\theta = \mathsf{Const}$, which is the direction of the magnetic field line.

II. APPENDIX: HIGHER ORDER EXPONENTIAL WEIGHTED FIT

This section gives a natural generalization of the equilibrium estimation described in Sec. IV C. Higher order polynomials are used as the target function for the estimation. This method does not necessarily increase the performance of the estimation. The derivation is carried under pure mathematical curiosity.

The equilibrium target function is const at $0\mathsf{th}$ order and linear, $a + bs$, at the first order. For the $n\mathsf{th}$ order polynomial, the target equilibrium should be $\sum_{i=0}^{n} c_i s^i$. The penalty function for the estimation is:

$$I(t, \{c_i\}) = \int_0^\infty \left(f(t-s) - \sum_{i=0}^{n} c_i s^i \right)^2 e^{-\alpha s} ds \tag{30}$$

Minimizing the penalty function with respect to all c_i leads to a linear algebra equation. Similar to the methods shown in Sec. IV C, we have:

$$\begin{pmatrix} 0! & 1! & 2! & \cdots & n! \\ 1! & 2! & 3! & \cdots & (n+1)! \\ 2! & 3! & 4! & \cdots & (n+2)! \\ \vdots & & & \ddots & \vdots \\ n! & (n+1)! & & \cdots & (2n)! \end{pmatrix} \begin{pmatrix} c_0/\alpha^0 \\ c_1/\alpha^1 \\ c_2/\alpha^2 \\ \vdots \\ c_n/\alpha^n \end{pmatrix} = \begin{pmatrix} K_1 \\ K_2 \\ K_3 \\ \vdots \\ K_{n+1} \end{pmatrix} \tag{31}$$

where we have used Eq. 20, and $\{K_i\}$ are defined as:

$$\begin{aligned} K_n(t) &= \alpha^n \int_0^\infty f(t-s) s^{n-1} e^{-\alpha s} ds \\ \frac{dK_n}{dt} &= \alpha[(n-1)K_{n-1} - K_n] \qquad for\ n = 2, 3, 4, \ldots \\ \frac{dK_1}{dt} &= \alpha(f - K_1) \end{aligned}$$

Adapting the L_α notation for the low pass filter, the expression for K_i can be written in a more compact form:

$$\begin{aligned} K_1 &= L_\alpha[f] \\ K_{n+1} &= nL_\alpha[K_n] \qquad for\ n = 1, 2, 3, \ldots \end{aligned}$$

Solving Eq. 31 gives all the coefficients $\{c_i\}$ needed for the estimated equilibrium function. c_0 will give the estimated value at current time. More interestingly, the slope of the equilibrium, and even estimations for higher order variation rates will be obtained from $\{c_i\}$. Numerically, the inverse of the coefficient matrix is a constant and can be calculated before hand. $\{K_i(t)\}$ can be updated by keeping a series of low pass filter. This provides a method of estimating the equilibrium parameter in the feedback system.

One interesting observation in Sec. IV C 1 is the relation between equilibrium estimation and the high pass filter. If the original signal is $f(t)$, the equilibrium estimation with linear equilibrium target function is $a(t)$ then the fluctuation signal $f-a$, can be obtained by simply passing f through the high pass filter twice. The similar statement is trivial for the zero order example. In fact, it can be proved generally for the nth order case. For example, in the above solution obtained from Eq. 31, the equilibrium estimated at the most recent time point would be c_0. It can be shown that the resulted fluctuation signal, $f-c_0$, is the same as passing f through the high pass filter n times:

$$f - c_0 = (1 - L_\alpha)^n[f]$$

To prove this formally, let's define:

$$A_n = \begin{pmatrix} 0! & 1! & 2! & \cdots & n! \\ 1! & 2! & 3! & \cdots & (n+1)! \\ 2! & 3! & 4! & \cdots & (n+2)! \\ \vdots & & & \ddots & \vdots \\ n! & (n+1)! & & \cdots & (2n)! \end{pmatrix}$$

Also, the coefficient c needs an extra index to show from which order of polynomial as equilibrium it is obtained:

$$A_n \begin{pmatrix} c_{n,0}/\alpha^0 \\ \vdots \\ c_{n,n}/\alpha^n \end{pmatrix} = \begin{pmatrix} K_1 \\ \vdots \\ K_{n+1} \end{pmatrix}$$

In this equation, the first index in c is always n, meaning that this set of solutions is obtained by using the nth order polynomial as the target equilibrium function. We will prove the result by induction. The solution for the estimation with the $n+1$th polynomial function is:

$$A_{n+1}\begin{pmatrix} c_{n+1,0}/\alpha^0 \\ \vdots \\ c_{n+1,n+1}/\alpha^n \end{pmatrix} = \begin{pmatrix} K_1 \\ \vdots \\ K_{n+2} \end{pmatrix}$$

The solution $c_{n,i}$ can be obtained by multiplying $\{K_n\}$ with A_n^{-1}. In fact, since we are only interested in the coefficient $c_{n,0}$, only the first row of A_n^{-1} matters. Let the first row be $v_n = \{v_{n,i}\}$. We have

$$c_{n,0} = \sum_{i=1,\ldots,(n+1)} v_{n,i}K_i \tag{32}$$

Note that A_n is a $(n+1)$-by-$(n+1)$ matrix, and v_n has n+1 entries. The fluctuation signal will be $f-c_{n,0}$. If the claim is true for nth order case, that $f-c_{n,0} = (1-L_\alpha)^n[f]$, then to prove the claim is true for the $n+1$th order, we only need to show that:

$$\begin{aligned} f - c_{n+1,0} &= (1-L_\alpha)^{n+1}[f] \\ &= (1-L_\alpha)(f - c_{n,0}) \\ &= (1-L_\alpha)(f - \sum_{i=1,\ldots,(n+1)} v_{n,i}K_i) \\ &= f - (v_{n,1}+1)K_1 - \frac{v_{n,n+1}}{n+1}K_{n+2} \\ &\quad - \sum_{i=2,\ldots,(n+1)} (v_{n,i} + \frac{1}{i-1}v_{n,i-1})K_i \end{aligned}$$

One can check Eq. 32 under the $n+1$th order and compare the coefficient with above formula. To prove the claim, one needs to show that the first row of A_{n+1}^{-1}, v_{n+1} can be expressed as:

$$\begin{aligned} & v_{n+1} = \begin{pmatrix} v_{n,1} & v_{n,2} & \cdots & v_{n,n+1} & 0 \end{pmatrix} + u_{n+1} \\ \text{with}\quad & u_{n+1} = (u_{n+1,1},\ldots,u_{n+1,n+2}) = \begin{pmatrix} 1 & -v_{n,1} & -\frac{1}{2}v_{n,2} & \cdots & -\frac{1}{n+1}v_{n,n+1} \end{pmatrix} \end{aligned} \tag{33}$$

A_n^{-1} is the unique solution for $A_n \cdot A_n^{-1} = I$. Since $A_n = A_n^T$ is a symmetric matrix,

v_n is the unique vector that has inner product of 1 with the first row of A_n, and is orthogonal with the rest rows in A_n. To prove the claim, we need to show that the expression given by Eq. 33 satisfies the same constraints for matrix A_{n+1}.

We first write down the constraints that v_n satisfies:

$$\sum_{i=1}^{n+1}(i-1)!v_{n,i} = 1$$
$$\sum_{i=1}^{n+1}(i+k)!v_{n,i} = 0 \quad \text{for k=0,...,n-1}$$

These are just the statements of the inner product constraints. Now lets check if the constraints for v_{n+1} are satisfied. The inner product of first row of A_{n+1} with v_{n+1} has:

$$\begin{aligned}
&\sum_{i=1}^{n+2}(i-1)!v_{n+1,i} \\
&= \sum_{i=1}^{n+1}(i-1)!v_{n,i} + 1 - \sum_{i=1}^{n+1} i!\frac{1}{i}v_{n,i} \\
&= 1 + 1 - \sum_{i=1}^{n+1}(i-1)!v_{n,i} \\
&= 1
\end{aligned}$$

The above derivation also shows an important property for u_{n+1}:

$$\sum_{i=1}^{n+2}(i-1)!u_{n+1,i} = 0 \tag{34}$$

Now let's check the rest of the constraints. For the 1 to nth row of A_{n+1}, we need to prove the following term is 0, for k in 0 to $n-1$:

$$
\begin{aligned}
&\sum_{i=1}^{n+2}(i+k)!v_{n+1,i} \\
&= \sum_{i=1}^{n+1}(i+k)!v_{n,i} + \sum_{i=1}^{n+2}(i+k)!u_{n+1,i}
\end{aligned}
$$

The first term is zero from the constraint on $v_{n,i}$. The second term can be shown to be zero by induction:

$$
\begin{aligned}
I_{n+1,k} &= \sum_{i=1}^{n+2}(i+k)!u_{n+1,i} \\
&= \sum_{i=1}^{n+2}(i+k-1)!(i+k)u_{n+1,i} \\
&= (k+1)\sum_{i=1}^{n+2}(i+k-1)!u_{n+1,i} \\
&\quad + \sum_{i=1}^{n+2}(i+k-1)!(i-1)u_{n+1,i} \\
&= (k+1)I_{n+1,k-1} \\
&\quad - \sum_{i=2}^{n+2}(i+k-1)!(i-1)\frac{1}{i-1}v_{n,i-1}
\end{aligned}
$$

The second term in above result is zero:

$$
\sum_{i=1}^{n+1}(i+k)!v_{n,i} = 0 \qquad \text{for k=0,...,n-1}
$$

Since $I_{n+1,-1} = 0$ is shown in Eq. 34. We have shown $I_{n+1,k} = (k+1)I_{n+1,k-1} = 0$ for k=0,...,n-1. Thus, the constraints are satisfied that

$$
\sum_{i=1}^{n+2}(i+k)!v_{n+1,i} = 0 \qquad \text{for k=0,...,n-1}
$$

The only thing left is to show that the above equation is also true for $k = n$. Similarly, one has:

$$\begin{aligned}
&\sum_{i=1}^{n+2}(i+n)!v_{n+1,i} \\
&= \sum_{i=1}^{n+1}(i+n)!v_{n,i} + \sum_{i=1}^{n+2}(i+n)!u_{n+1,i}
\end{aligned} \tag{35}$$

The second term

$$\begin{aligned}
I_{n+1,n} &= \sum_{i=1}^{n+2}(i+n)!u_{n+1,i} \\
&= \sum_{i=1}^{n+2}(i+n-1)!(i+n)u_{n+1,i} \\
&= (n+1)I_{n+1,n-1} \\
&\quad + \sum_{i=1}^{n+2}(i+n-1)!(i-1)u_{n+1,i} \\
&= -\sum_{i=1}^{n+1}(i+n)!v_{n+1,i}
\end{aligned}$$

where we have used $I_{n+1,n-1} = 0$. This shows that the two terms in Eq. 35 are equal and opposite to each other and the sum is zero. Thus the last constraint has been satisfied.

We thus have shown that the expression of v_{n+1} given by Eq. 33 is indeed the first row of A_{n+1}^{-1}. Thus we have proved the claimed equivalence that

$$f - c_{0,n} = (1 - L_\alpha)^n[f]$$

is held by all $n \geq 1$. This provides a convenient way of obtaining the fluctuation signal consistent with estimating the equilibrium signal as a nth order polynomial function.

III. APPENDIX: FEEDBACK SYSTEM MANUAL

The feedback system contains many files, some of them controls the CPU, GPU and other parts on in the system directly, while others configure the settings for the system. Here, the important files are shown with some explanations about the functions in it.

A. fbsetting.py

This is a python file in which most of the feedback parameters are specified. Some settings are no longer used but the code is still remained for reference of what methods have been tried.

- CYCLE_TIME is the time between two adjacent data points. It specifies the sampling rate.
- WAITx_TIME specifies different time points in the feedback system, where a certain phase is entered or left. This value is often adjusted with respect to the style of the discharges one is working on.
- IN_MODE_MATRIX is the projection matrix that transfers the sensor signals to the mode signals in sine and cosine basis.
- OUT_MODE_MATRIX is the matrix that cast the perturbation in mode domain to specific values for each control coil.
- P_BASE_GAIN specifies the proportional gain for the modes measured from the poloidal field sensors, where P stands for poloidal.
- P_BASE_PHASE specifies the phase shift between perturbation and measured poloidal field modes.

In this file, the capitalized variables will be used by other file. Non-capitalized variables are parameters for human interpretation, based on which some of the capitalized variables are generated.

B. gen_fb_hdrs.py

This is the file that loads variables from fbsettings.py and further prepares them for the usage by execution code.

- c_lit_matrix function prints out matrices in a format that can be directly used to initialize C arrays.
- map1 maps the magnetic sensor names to input channel numbers on the breakout board. map2 maps the input channels to output channels on the breakout board, reflecting the actual physical connections of the wires. These two maps tell the code which index the signal from a given sensor with be assigned.
- The cc_channel_map() performs similar function for the control coils.
- The input and output projection matrices loaded from the fbsettings.py will then be reordered to have it matching the orders of the indices.

The final step in the file writes all the relevant parameters into fbsetting.h with the header file format that can be included by other .cpp codes.

C. gpu_common.cu

- The wait_for_sample function causes the thread to pause until new data sample arrives. TLATCH_OFFSET is the index on the input sample where the time stamp of the data is stored. The method is implemented as a spin lock.

D. rtm-t.cpp

This file implements the methods to initialize the ACQ196 and AO32 devices. For a memory on the GPU, it can be referred in three ways, the physical address, the host address and the device address. The initialization methods find those addresses and connect them consistently so the ACQ196, AO32 and GPU write to the same memory space and hence transfer data correctly.

The ioctl function is implemented in rtm-t-hostdrv.c under /usr/local/src/RTM-T.

E. do_fb.cpp

This code initializes the feedback system, sets up the GPU program, and after the plasma discharge, stores the log for later review.

- In the main_real function, the input can be set to come from live experiment, or from the previously stored experimental data. Reading the previous stored data is a way to debug/validate the system without actually running the experiment. The choice can be made by toggling "#define FAKE_INPUT".

- The code allocates several blocks of memory on the GPU device as buffers for data storage. This is performed by calling cuMemAlloc and cuMemsetD8.

- Precalculated matrices are also loaded into the GPU memory by calling cuMemAlloc and cuMemcpyHtoD.

- The start_kernel function invokes the GPU code and the CPU code will pause until the GPU code finishes after the experiment.

- The cuMemcpyDtoH transfers the log data from GPU memory to the disk and stores them.

F. gpu_fb.cu

This is the CUDA file where the feedback algorithm is implemented. Many threads on the GPU will be running the same code in parallel. The only difference is that they will be assigned with different threadIdx.x value, which is stored locally as an integer: tid. The thread will behave differently depending on this value. Each thread will have its own version of the local variables defined in the function, they share the access to some arrays on the shared memory.

- The first part of the function is to find the my_ao and my_ai for each thread, according to the index. Each thread is responsible of reading the signal from its input and setting the value for its output channel.

- For the thread that will be handling the modes. They need to handle sine and cosine mode with the same expression. Thus some shift parameter is needed to set beforehand. The basic idea is that $sin(\theta) = cos(\theta - \pi)$. The pairs always have cosine mode one the first index and sine mode on the second, so the cosine mode's counterpart's index will be one after its own and vice versa for the sine mode.

- The main body of the function is a big for loop in which every batch of the experimental data is treated in a similar manner. The sample_no tells the timestamp for the data and the feedback system enters different stages according to this value.

- The first stage, with sample_no $<$ OFFSET_SAMPLES, is before the plasma break down. Measured signal in this stage is used to determine the offset level on the sensors, because some signal channels give non-zero output even with nothing going on in the experiment.

- After the first stage, the magnetic signal is integrated to give the B value from the $\partial B/\partial t$ measurement. This integration uses the same formula as that in the hbtep2 tree, so the magnetic sensor readings are consistent with those stored in the tree.

- The modes' sine and cosine component are calculated with the projection matrix preloaded in in_mtx. The signals are high pass filtered before used for amplitude and phase calculation. The signal of each traces is logged in mamp_store matrix.

- The code ignores big jumps in the phase (larger than $\pi/2$), and fills the ignored data with best guesses from previous data.

- The output mode is then calculated with proportional gain on the detected mode.

- For the output voltage signal. The code first compensates the desired control coil current for the target B_r field (the effect is small), then compensates the current signal to obtain the request voltage output for each amplifier.

- When the loop finishes, the code resets the output voltage on coils to be zero and then returns.

G. Makefile.common

This the the file that is called when one types "$make fb_shot".

- As is shown in the bottom of the file. The code will check if do_fb and gpu_fb.cubin is up to date. It will recompile them if needed.

- The code will sleep for 40 seconds before calling the executable ./do_fb. This is because the GPU code will wait in the for loop until the first signal arrives, which happens 1ms before the plasma breakdown. The waiting function is implemented in gpu_common.cu and it has a maximum waiting period which is, shorter than the time needed for the capacitor banks to charge. The code sleeps for roughly 40 seconds so that the ./do_fb executable is called shortly before the plasma discharge.

- After the execution of the feedback program, this code copies the log data into /opt/hbt/data/control with shotnumber as the name tag.

H. fbtools.py

This file implements various functions that are used by other feedback configuration files. Most importantly, the sensor signals to modes projection matrix and the perturbation mode to control coil current projection matrix are calculated in this file. The code should be self-explanatory.